Investigation of surface exchange and bulk diffusion of oxygen in ceria-based redox materials with isotope exchange experiments utilizing $^{18}O_2$ and $C^{18}O_2$

Dissertation

Zur Erlangung des Doktorgrades

der Naturwissenschaften

vorgelegt von

Daniel Uxa

aus Eisenhüttenstadt

genehmigt von der

Fakultät für Natur - und Materialwissenschaften

der Technischen Universität Clausthal

Tag der mündlichen Prüfung:

08. Februar 2022

Dekan

Prof. Dr.-Ing. Joachim Deubener

Vorsitzende der Promotionskommission

Prof. Dr. rer. nat. Ursula Fittschen

Betreuer

apl. Prof. (a.D.) Dr.-Ing. Günter Borchardt

Gutachter

Prof. Dr. rer. nat. Martin Schmücker

Der Text steht, soweit nicht anders gekennzeichnet, unter der Creative-Commons-Lizenz CC-BY.

Preface

This work was accomplished at the Institute of Metallurgy at the Clausthal University of Technology in the context of the Virtual Institute SolarSynGas, a project funded by the Initiative and Networking Fund of the Helmholtz Association of German Research Centers. Additional financial support was provided by the Schöne family foundation and the German Research Foundation. I would like to take this opportunity to express my sincere thanks.

I am using this opportunity to express my gratitude to Prof. Dr. Günter Borchardt for supervising my work, for all the help and support, and for the fruitful dialogue and constructive discussions regarding my results, as well as Prof. Dr. Martin Schmücker for acting as the second examiner.

I would like to especially thank Dr. Lars Dörrer. He guided my research and shared all the feedback that was necessary to accomplish this thesis. I would also like to thank Prof. Dr. Harald Schmidt for his backing, support and trust during my doctorate.

I would like to thank all of my colleagues and partners at the Virtual Institute SolarSynGas for their support and good cooperation, in particular Prof. Dr. Martin Schmücker, Prof. Dr. Christopher Muhich, Dr. Nicole Knoblauch, Dr. Martin Roeb, Dr. Stefan Brendelberger and Dr. Brendan Bulfin.

I would also like to thank my current and former colleagues at the institute and especially in the Thermochemistry and Microkinetics Group, Dr. Erwin Hüger, Dr. Peter Fielitz, Dr. Florian Strauß, Dr. Claudia Kofahl, Johanna Uhlendorf and Jochen Junge, as well as the technical employees of the Metallography, the Electrical Workshop and the Mechanical Workshop, who supported my work.

Further I would like to thank Dr. Michal Schulz, Dr. Stefan Beschnitt, Prof. Dr. Christos Argirusis and Francois Jomard for the help and for carrying out SIMS measurements.

Finally, I would like to thank all of my colleagues for their help, who are not explicitly mentioned at this point, but who have nevertheless contributed to the success of this work.

I dedicate this work to my long-time student friend, companion and colleague Kevin Meyer.

Abstract

The focus of this thesis is the experimental investigation of ceria-based redox materials, which are associated to two-step solar thermochemical splitting of carbon dioxide. Important detailed questions regarding the reaction kinetics, the exact influence of doping elements and the macroscopic and microscopic structure of the redox material as well as the cyclic stability have to be answered in order to achieve a scaling of the redox process to the technical scale. Surface exchange reactions and bulk transport of oxygen in ceria are of high relevance. Therefore, this work focusses on the surface reaction with carbon dioxide reduction and oxygen exchange, oxygen diffusion in bulk ceria samples, the phenomenological description (K_O, D_O), the interpretation of the calculated rate constants, the influence of the doping elements and the influence of the oxygen partial pressure of the gas atmosphere.

The most direct method of measuring oxygen diffusivities and surface exchange coefficients in oxides is oxygen isotope exchange followed by Secondary Ion Mass Spectrometry (SIMS). By utilizing oxygen isotope enriched $^{18}O_2$ and $C^{18}O_2$ gas atmospheres as well as $CeO_{2-\delta}$ and $Ce_{0.9}M_{0.1}O_{2-\delta}$ (with M = Y, Sm, Zr) samples under various experimental conditions this well-established approach represents the core of the experimental work of this thesis.

The experimental results are promising in terms of CO_2 splitting with trivalent-doped ceria, especially Sm-doped ceria, at lower temperatures than the proposed conditions for this reaction step. The majorities of isotope exchange experiments show enhanced values of D_O and K_O for Sm-doped cerium dioxide, in comparison to Y-doped and Zr-doped ceria, as well as nominally undoped ceria. For the determinable apparent activation energies, the values for Sm-doped ceria are lowest. Sm-doped and Y-doped ceria samples tend to reach the surface exchange controlled kinetic regime at $T \geq 700\,°\mathrm{C}$. This is attributed to the fact that the trivalent dopant increases the concentration of oxygen vacancies, and hence the diffusivity of oxygen in comparison to the Zr-doped ceria and nominally undoped ceria samples. Considering the investigations, a temperature of $T = 500\,°\mathrm{C}$ is feasible for solar thermochemical cycling due to the weak temperature dependency of the parameters $\tilde{K}_\mathrm{O}$ and $\tilde{D}_\mathrm{O}$. Higher reduction extents δ are therefore necessary, given constant reaction conditions. An investigation of the optimal oxygen vacancy concentration of the redox material with systematic variation of the oxygen non-stoichiometry in the reduction step is suggested.

Kurzzusammenfassung

Der thematische Schwerpunkt dieser Arbeit liegt auf experimentellen Untersuchungen von Cerdioxid-basierten Redoxmaterialien, die zur zweistufigen solarthermochemischen Spaltung von Kohlendioxid eingesetzt werden. Wesentliche Detailfragen, vor allem zur Reaktionskinetik, zum genauen Einfluss von Dotierungselementen und zur makroskopischen und mikroskopischen Struktur des Redoxmaterials, sowie zur Zyklierstabilität müssen noch beantwortet werden, um eine Skalierung des Redoxprozesses in den großtechnischen Maßstab zu ermöglichen. Oberflächenaustauschreaktionen und die Diffusion von Sauerstoff in Cerdioxid sind hierbei von hoher Relevanz. Daher konzentriert sich diese Arbeit auf die Oberflächenreaktion mit Kohlendioxidreduktion und Sauerstoffaustausch, Sauerstoffdiffusion in Ceroxid-Proben, die phänomenologische Beschreibung (K_O, D_O), die Interpretation der berechneten Geschwindigkeitskonstanten, den Einfluss der Dotierelemente und den Einfluss des Sauerstoffpartialdrucks der Gasatmosphäre.

Der direkteste Ansatz zur Bestimmung von Sauerstoff-Diffusionskoeffizienten sowie von Oberflächenaustauschkoeffizienten in Oxiden ist der Sauerstoffisotopenaustausch in Kombination mit Sekundärionen-Massenspektrometrie (SIMS). Mit der Verwendung von mit Sauerstoffisotopen angereicherten $^{18}O_2$ - und $C^{18}O_2$ -Gasatmosphären sowie $CeO_{2-\delta}$ und $Ce_{0.9}M_{0.1}O_{2-\delta}$ (mit $M = Y, Sm, Zr$) Probenmaterial unter verschiedenen experimentellen Bedingungen stellt dieser Ansatz den Schwerpunkt dieser Arbeit dar.

Die experimentellen Ergebnisse sind vielversprechend hinsichtlich der Kohlendioxidpaltung mit dreiwertig dotiertem Cerdioxid, insbesondere Sm-dotiertem Cerdioxid, bei niedrigeren Temperaturen, als bisher für diesen Reaktionsschritt vorgeschlagen wurden. Die Mehrzahl der Isotopenaustauschexperimente zeigte erhöhte Werte für D_O und K_O bei Sm-dotiertem Cerdioxid, im Vergleich zu Y-dotiertem und Zr-dotiertem Ceroxid, sowie nominell undotiertem Cerdioxid. Die berechneten Aktivierungsenergien sind für Sm-dotiertes Cerdioxid am niedrigsten. Sm-dotierte und Y-dotierte Cerdioxidproben tendieren dazu, das durch den Oberflächenaustausch kontrollierte kinetische Regime bei $T \geq 700$ °C zu erreichen. Dies ist auf die Tatsache zurückzuführen, dass dreiwertige Dotierelemente die Konzentration an Sauerstoffleerstellen und damit die Diffusivität des Sauerstoffs im Vergleich zu den Zr-dotierten und nominell undotierten Cerdioxidproben erhöhen. In Anbetracht der Untersuchungen ist aufgrund der schwachen Temperaturabhängigkeit der Parameter $\tilde{K}_\mathrm{O}$ und $\tilde{D}_\mathrm{O}$ eine Temperatur von $T = 500$ °C für solarthermochemische Kreisprozesse realisierbar.

Bei konstanten Reaktionsbedingungen sind hierfür höhere Reduktionsgrade δ erforderlich. Eine Untersuchung der optimalen Sauerstoffleerstellenkonzentration des Redoxmaterials mit systematischer Variation der Sauerstoff-Substöchiometrie im Reduktionsschritt wird vorgeschlagen.

Contents

Nomenclature

Symbols

σ	diffusion length
τ	characteristic time constant
ΔH	enthalpy
a	activity
c	concentration
D	diffusion coefficient
F	force
G	free enthalpy
h	sample thickness
I	intensity
k_B	BOLTZMANN constant
k	reaction rate
K	surface exchange coefficient
$K_\mathrm{red/ox}$	equilibrium constant
L	dimensionless parameter defining the kinetic regime
p	pressure
q	charge
T	temperature
t	time
x	depth or length
α	ionization probability
δ	suboxide parameter defining the non-stoichiometry of a metal oxide
κ	conductivity

Y	sputter yield
γ	detection efficiency of a SIMS machine
f	correlation factor
j	flux
μ	chemical potential
Γ	jump rate
v	jump frequency
R	universal gas constant
$\Re^0$	equilibrium exchange rate
V	volume
w	thermodynamic factor

Abbreviations and acronyms

DFT	density functional theory
f.c.c.	face-centered cubic
FWHM	full width at half maximum
HREELS	High resolution electron energy loss spectroscopy
ICP-OES	Inductively coupled plasma optical emission spectrometry
IEDP	isotope exchange depth profile
IELS	isotope exchange line scan
LEIS	Low-energy ion scattering
MIEC	mixed ionic electronic conductor
MO	metal oxide
rds	rate determining step
RE	rare-earth element
RT	room temperature
SIMS	secondary ion mass spectrometry
SOFC	solid oxide full cell
STCC	solar thermochemical cycling
ToF	Time-of-Flight
UPS	Ultraviolet photoelectron spectroscopy
XPS	X-ray photoelectron spectroscopy
XRD	X-ray diffractometry
YSZ	yttria-stabilized zirconia

1 Introduction

The future energy supply is certainly one of the major challenges humankind is confronted with, along with the associated global warming, challenging social, economic and political stability and national security [Smit10, Murr12, Hook13]. The majority of the fuels consumed worldwide are based on petroleum or natural gas [Harr06], and as the utilization of fossil fuels is directly linked to the release of carbon dioxide, the portion of molecules per million in the atmosphere climbs about two every year [Soco05]. Beside the well-established scientific concepts regarding the global greenhouse effect, undoubtedly no one knows the exact consequences of neither this upsurge nor the effects that lie ahead as the atmosphere´s carbon dioxide concentration rises. Taking into account both the increasing global energy demand and the urgent need to at least stabilize the atmosphere´s carbon dioxide concentration, if not reducing it, various scenarios describe different paths towards an carbon-neutral technology-based energy supply system in the near future .

With solar energy being the most abundant renewable energy source available, the chemical storage of solar energy in form of chemical bounds is a promising candidate for the extensive use on a global scale. In particular the solar-driven selectively production of basic chemicals (H_2, CO) for synthetic fuels, applying thermochemical cycles with concentrated solar energy as heat source, represents a straightforward solution with the highest thermodynamical efficiencies [Aban06, Sieg13]. Solar fuels open up the possibility to store solar energy and act as future energy carrier for the transport sector and the chemical industry.

A redox material which allows water or carbon dioxide splitting at feasible conditions is essential for such thermochemical processes. As early as 1977 metal oxide based redox materials were suggested for thermochemical solar fuel production [Naka77]. Due to its redox thermodynamics and fast redox kinetics, not displaying complex behavior of oxygen non-stoichiometry as a function of temperature and oxygen activity, cerium dioxide is a very attractive redox reactive material and was first applied in 2006 for the production of hydrogen, carbon monoxide and the mixture of both, being referred to as syngas [Aban06].

The basic proof of function considering the splitting of water and carbon dioxide by means of the thermochemical cycle utilizing ceria could be obtained since then in several laboratory studies [Chue09, Chue10, Furl12]. It is now one of the most widely studied fluorite-based oxides. Besides thermodynamic and kinetic reasons, the ceria redox system is attractive from a technical point of view for two reasons.

First, in contrast to other oxides with fluorite structure AO_2 (A = Hf, Pu, Th, U, Zr), CeO_2 is in cubic structure from room temperature to its melting point under normal ambient pressure without the need to stabilize it with a lower-valent cationic dopant. Second, since reduced ceria is structurally closely related to cerium dioxide, the redox reaction is a gradual oxygen exsolution/incorporation process rather than true phase transformation. Additionally, doping ceria with tri - and tetravalent dopants is the most promising method to improve its properties [Moge00, Trov02]. However, important detailed questions, in particular regarding the reaction kinetics, the exact influence of doping elements, the macroscopic structural parameters (powders, granules, foams, honeycomb structures etc.), the microstructure and porosity of the redox material as well as the cyclic stability still have to be answered in order to achieve a scaling of the redox process in the technical scale.

In general, redox kinetics of oxides is either controlled by surface exchange reactions or by bulk transport of oxygen. The most important prerequisite for the targeted further development of the redox material is the exact knowledge of fundamental parameters such as surface exchange coefficients, K_O, and diffusion coefficients, D_O, of oxygen [Knob15, Knob17].

In the case of carbon dioxide splitting the available data is still very fragmented. In addition to computer simulations on the reaction between CO_2 and CeO_2 on the basis of density functional theory (DFT) (see i.e. [Hahn13] and [Chen13]) there are only a few recent experimental studies on this question. Recent work on the system $CeO_{2-\delta}$ and $Ce_{1-x}M_xO_{2-\delta}$ (M = tri - and tetravalent dopants), which were carried out in the context of thermochemical cycle processes, aim primarily at the thermodynamic characterization of the redox system [Taka15, Bulf16, Dave16], on the design of the solar-heated reactor [Furl12, Acke14b], and the influence of dopants [LeGa13, Kuhn13, Call15], and pursue a primarily technically oriented objective.

The present thesis focuses on experimental investigations of ceria in order to minimize the existing data gap (K_O, D_O), with carbon dioxide reduction in focus, being one of the two essential steps towards the solar thermochemical production of syngas, and in many cases advantageous compared to water splitting regarding the efficiency [Lang15]. The most direct method of measuring oxygen diffusivities and surface exchange coefficients in oxides is oxygen isotope exchange followed by Secondary Ion Mass Spectrometry (SIMS) depth profiling (IEDP) or cross section line scan (IELS).

By utilizing oxygen isotope enriched $^{18}O_2$ and $C^{18}O_2$ gas atmospheres and various experimental conditions, this well established approach represents the core of the experimental work of this thesis. From the current state of research, critical problem complexes such as surface reaction with carbon dioxide reduction in comparison to the oxygen exchange reaction, phenomenological description (K_O, D_O) and interpretation of the rate constants, diffusion in chemical non-equilibrium, influence of the doping elements, influence of the respective kinetic regime and influence of oxygen vacancy concentration and possible defect complex formation can be identified and targeted.

2 Motivation and background

2.1 Solar thermochemical redox reaction

In order to overcome the global challenge induced by fossil fuel depletion and the fact that our mobility relies on unsustainable raw materials, great research effort is put into the production of hydrogen and synthetic hydrocarbons [Chue10, Sche12, Call13, Acke14a, Call15, Acke15, Marx15, Lang16, Taka17, Bhos19]. The solar thermochemical splitting of carbon dioxide and water via two-step redox reactions (solar thermochemical cycling, STCC), utilizing concentrated solar energy and a metal oxide (MO) as redox material, is generally referred to as a favorable path for producing syngas [Lang15]. It operates at high temperatures and utilizes the entire solar spectrum via concentration of direct solar radiation with optical point focusing systems [Rome07, Marx15].

In principle the two-step redox cycle consists of two thermochemical reactions, as illustrated in Figure 1, a high-temperature endothermic reduction step,

$$\mathrm{MO_x} \rightarrow \mathrm{MO_{x-\delta}} + \frac{\delta}{2}\mathrm{O_2(g)}\,, \tag{1}$$

and a low-temperature exothermic re-oxidation step going along with the splitting of water and/or carbon dioxide,

$$\mathrm{MO_{x-\delta}} + \delta\mathrm{H_2O(g)} \rightarrow \mathrm{MO_x} + \delta\mathrm{H_2(g)}\,, \tag{2a}$$

$$\mathrm{MO_{x-\delta}} + \delta\mathrm{CO_2(g)} \rightarrow \mathrm{MO_x} + \delta\mathrm{CO(g)}\,, \tag{2b}$$

where the non-stoichiometry δ denotes the reduction extent [Chue10, Call13, Call15, Lang15].

Reduction of the metal oxide occurs at elevated temperatures and low oxygen partial pressure by the formation of oxygen vacancies V_O in the crystal lattice. The characteristic parameter δ defining the non-stoichiometry is determined by the applied T- p_{O_2} conditions in Equation (1) and is material specific. Subsequent re-oxidation of the reduced metal oxide in the presence of water vapour or carbon dioxide according to Equations (2a) and (2b) causes the splitting reaction. Commonly, the temperature and gas atmosphere are cycled between the high-temperature reduction step (1) (T_{red} is about 1200 - 1600 °C) and the low-temperature splitting/re-oxidation step (2a-b) (T_{ox} is about 800 - 1000 °C) [Marx15, Lang15].

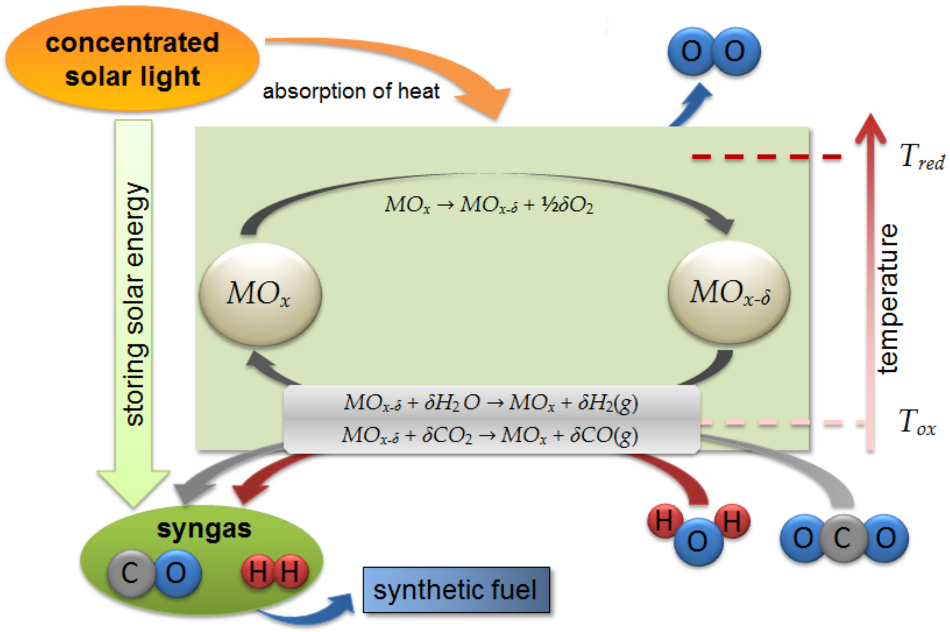

Figure 1. Schematic diagram of the solar-driven two-step thermochemical splitting of either carbon dioxide or water. MO denotes a metal oxide utilized as redox material that is either reduced ($MO_{x-\delta}$) or re-oxidized (MO_x). Adapted from [Call13, Call15].

According to the respective literature [Chue10, Sche12, Acke14a, Lang15, Marx15, Acke15, Taka17], the material specific T- p_{O_2} conditions, determining the parameter $\delta = f(T, p_{O_2})$ in Equation (1), are the most important quantities considering the fundamental relations of solar-driven thermochemical fuel production.

A decrease of the temperature for both the reduction and the re-oxidation step results i.e. in the decrease of radiation losses of the optical solar concentration system as well as in a reduction of the thermal load of the redox material, which is critical with regard to the materials stability during long-term cycling [Lang15]. An increase of the ceria non-stoichiometry enhances significantly the CO_2/H_2O splitting performance and therefore the overall process efficiency for given constant reaction conditions [Chue10, Acke15].

It is consensus that an efficient redox material and that optimizing the materials properties are essential to feasible solar fuel production and overall process efficiency enhancement [Sche12, Call13, Acke14a, Call15, Lang15, Marx15, Acke15, Taka17]. As it is not the aim of this work to focus on the thermodynamic characterization of the redox system, or on other technically oriented objectives, the reader is referred to the respective literature cited for a more thorough discussion.

2.2 Cerium dioxide as a redox material

Cerium dioxide (and solid solutions based on it) causes interest for several decades and it is one of the most widely studied fluorite-based oxides [Blum71, Tull77, Wang80, Hohn81, Fabe89, Eguc92, Moge00, Tian02]. In contrast to other oxides with the fluorite structure AO_2 (A = Hf, Pu, Th, U, Zr), pure stoichiometric CeO_2 maintains its cubic structure (f.c.c.) from room temperature to its melting point of 2750 K under normal ambient pressure without the need to stabilize it with a lower-valent cationic dopant [Sriv74, Scot75], and it does not show a complex behavior of oxygen non-stoichiometry as a function of temperature and oxygen activity [Bell69, Matz69, Ando83, Matz83, Bayo84, Matz87]. As depicted in Figure 2 the structure of CeO_2 consists of a cubic closed packed array of cerium atoms and a cubic primitive arrangement of oxygen atoms [Trov02].

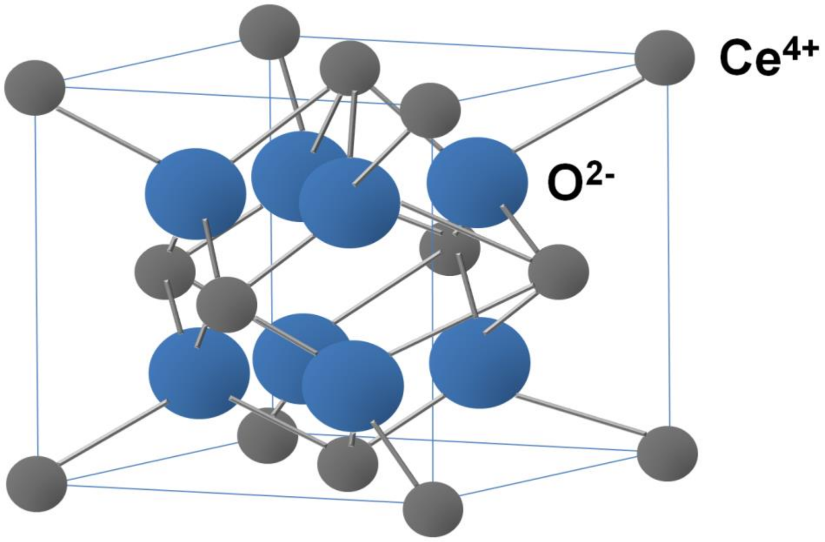

Figure 2. Unit cell of CeO_2 with cubic fluorite structure. It contains four formula units CeO_2. Ce^{4+} cations (gray) span a cubic face-centered lattice. The tetrahedral gaps are occupied by the O^{2-} anions (blue), which thus form a cubic primitive sublattice. Adapted from [Trov02].

Its general ability to conduct oxygen anions through oxygen vacancies in the crystal lattice and the ability to generate ceria-based solid solutions are the best among ionic conductors [Trov02]. At high temperatures ceria is prone to sintering (most probably due to the relative immobile cations) and is therefore mainly used as a catalyst or catalyst support. Catalysts based on cerium dioxide are well established (i.e. in automotive catalytic converters and as fluid-cracking catalysts in refineries). Ceria is essential to many applications in electrochemistry, in particular as an electrolyte in solid oxide fuel cells (SOFC).

The remarkable enhancement of catalytic activity by ceria is attributed to its ability to display large oxygen non-stoichiometry without relevant changes in its crystal structure. This so-called "oxygen storage capacity" is the ability to donate oxygen to or accept oxygen from its surrounding atmosphere. In general this can be understood by considering cerium dioxide as a redox system where oxygen is released by reduction of Ce^{4+} to Ce^{3+} and reabsorbed by reoxidation of Ce^{3+} to Ce^{4+}. During the reduction oxygen vacancies $V_O^{\bullet\bullet}$ are formed in order to obtain charge balance of the ionic crystal, which is of central importance [Trov02]. Using the KRÖGER-VINK notation [Kroe56], the following equation shows how the changing concentrations of Ce^{4+} ions ($[Ce_{Ce}^{x}]$) and Ce^{3+} ions ($[Ce_{Ce}']$) (concentrations denoted by square brackets) are related to the oxygen vacancy concentration $\left[V_O^{\bullet\bullet}\right]$:

$$2Ce_{Ce}^{\times} + O_O^{\times} \leftrightarrow 2Ce_{Ce}' + V_O^{\bullet\bullet} + \frac{1}{2}O_2(g)\,. \tag{3}$$

Several metal oxides have been suggested for the redox cycle (Equations (1) and (2a-b)), including ZnO [Stei02, Koep16], mixed metal ferrites MFe_2O_4 (M = Fe, Co, Ni)[Naka77, Alle08, Lich12], perovskites (ABO_3)[McDa13] and ceria (CeO_2). Due to its redox thermodynamics, fast redox kinetics and long-term stability cerium dioxide is a very attractive redox reactive material and was first applied in 2006 for the production of hydrogen, carbon monoxide and syngas [Aban06]. Currently most of the research is dealing with ceria as a potential candidate for solar fuel generation via two-step thermochemical splitting of water and carbon dioxide [Chue10, Sche12, Call13, Acke14, Call15, Acke15, Marx15, Lang16, Taka17, Bhos19]. Applying (non-stoichiometric) ceria in STCC modifies the general Equations (2a) and (2b) as follows. In the first step of a ceria-based thermochemical cycle, CeO_2 is partially reduced to $CeO_{2-\delta}$, releasing oxygen from the crystal lattice:

$$CeO_2 \leftrightarrow CeO_{2-\delta} + \frac{\delta}{2}O_2(g)\,. \tag{4}$$

In the second step Ce^{3+} reoxidizes to Ce^{4+} in the presence of H_2O/CO_2 to produce H_2/CO, as discussed previously:

$$CeO_{2-\delta} + \delta H_2O(g) \rightarrow CeO_2 + \delta H_2(g)\,, \tag{5a}$$
$$CeO_{2-\delta} + \delta CO_2(g) \rightarrow CeO_2 + \delta CO(g)\,. \tag{5b}$$

The thermodynamic properties and the redox kinetics of cerium dioxide can be influenced by doping with additional cationic elements.

Here the term “doping” should not be confused with the notion of doping commonly used in semiconductor physics, as it has the meaning of adding a cationic element M^{y+} into the cationic sublattice of ceria via a suitable metal oxide, resulting in a solid solution having the structure of $Ce_{1-x}M_xO_{2-\delta}$. Ceria is actually rather substituted than doped.

Today´s research has shown comprehensive attempts to modify ceria with di -, tri -, tetra - and pentavalent dopants to improve the redox performance of ceria. Di -, tri - and pentavalent dopants include Ca^{2+}, Mg^{2+}, Cu^{2+}, Sr^{2+}, Al^{3+}, Sc^{3+}, $Mn^{4+/3+/2+}$, $Fe^{3+/2+}$, Ni^{2+}, Y^{3+}, La^{3+}, $Pr^{4+/3+}$, Sm^{3+}, Gd^{3+}, Nb^{5+}, V^{5+} and Ta^{5+} [Kane07, Kane08, Chue09, Aban10, Meng11, Meng12, LeGa12, LeGa13, Sche13, Ramo14, Jian14, Muhi17].

Di - and trivalent dopants cause defects in the crystal structure of ceria that influence the transport properties of oxygen ions as well as the surface reactivity (see i.e. [Yang14]). Tetravalent dopants as Zr^{4+} and Hf^{4+}, however, have been shown to improve the redox capacity of ceria [Meng11, LeGa11, Hao14, Scar15].

A pivotal criterion to select promising dopants is their solubility in ceria. As long as the dopant cations feature radii close to that of Ce^{4+}, the fluorite structure is very tolerant to dissolution of up to 40 % of foreign oxides. In the case of oxides with cations much smaller or bigger than Ce^{4+} the solubility is very limited. Isovalent dopants, such as Zr^{4+}, feature excellent solubilities in ceria [Kim89, Moge00]. Within the catalysis community, doping of cerium dioxide with zirconium dioxide (CZO) has become standard [Pijo95, Forn96, Janv98, Kasp99, Vida01, Yang06, Delg13].

To enhance the catalytic properties of ceria the use of trivalent dopants caused attraction, which feature similar chemical properties, but induce extrinsic oxygen vacancies and therefore enhance the oxygen diffusion. The utilization of divalent dopants such as Ca^{2+} would induce even more oxygen vacancies, one per dopant ion, but due to the larger radius mismatch of divalent compared to trivalent dopants they exhibit significantly lower solubility [Ni08].

A more thorough discussion of the effects of doping ceria by adding a cationic element in terms of the redox properties, induced defects and their influence on the oxygen diffusion as well as the surface reactivity can be found in chapter 4.

2.3 The relevancy of understanding surface exchange reaction and oxygen bulk diffusion

Ceria-based redox materials are an integral part of investigations associated to solar thermochemical cycling. Nevertheless, important detailed questions, in particular regarding the reaction kinetics, the exact influence of cation doping elements, the macroscopic structural parameters, the microstructure and porosity of the redox material as well as the cyclic stability still have to be improved in order to meet industrial requirements.

As the redox kinetics of ceria-based materials is in general either controlled by surface exchange reactions or by bulk transport of oxygen, one legitimate approach to simplify the characterization of the carbon dioxide (or water) splitting process is as shown in Figure 3.

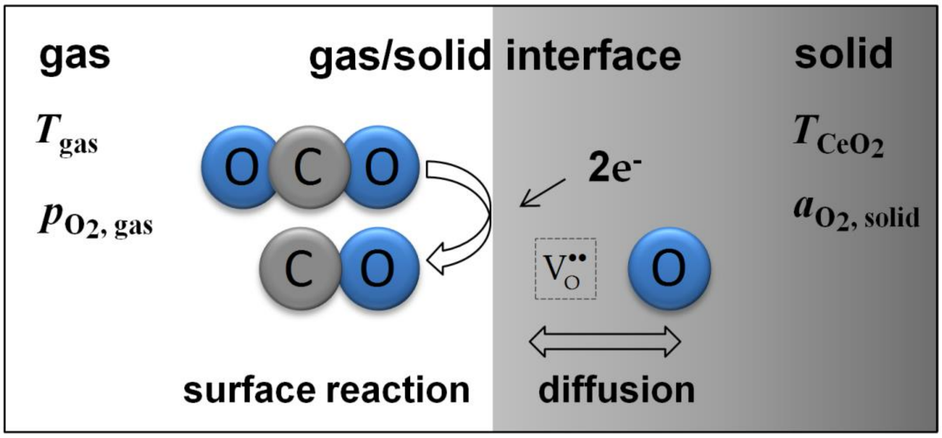

Figure 3. Simplification of the carbon dioxide splitting process with the surface reaction at the gas solid interface and (chemical) diffusion of oxygen in the solid where oxygen ions and bulk oxygen vacancies are involved. Both processes can be described by means of phenomenological quantities that are experimentally accessible. Further complication in the physical description is achieved by coupling both process steps.

First, there is the surface reaction at the gas/solid interface with the splitting of carbon dioxide to carbon monoxide, involving several reaction steps, including charge transfer and the exchange step of oxygen, involving surface oxygen vacancies. Second, (chemical) diffusion of oxygen occurs in the solid where oxygen ions and bulk oxygen vacancies are involved. Both processes can be described by means of phenomenological quantities that are experimentally accessible. Further complication in the physical description is achieved by coupling both process steps. The mathematical modelling based on this approach is discussed in detail in appendix E.

The characteristic parameter δ defining the non-stoichiometry of the ceria sample is experimentally determined by applied T-p_{O_2} conditions of the surrounding gas atmosphere (see Equation (4)) and material specific. In consequence, the most important prerequisite for the targeted further development of the ceria redox material is the exact knowledge of the fundamental phenomenological parameters, here the surface exchange coefficient, K_O, (with respect to the surface reaction) and the diffusion coefficient, D_O, of oxygen.

Transport properties of oxides are relevant in processes where the availability of an oxidant from the gas phase is not constant, and are determined by the presence, concentration and mobility of defects in the crystal lattice [Trov02]. If the oxygen diffusion is fast, a continuous supply of oxygen ions from the bulk to the surface and vice versa guarantees a constant surface concentration of oxygen or oxygen vacancies.

The global reaction for CO_2 splitting on reduced $CeO_{2-\delta}$ surfaces is summarized in KRÖGER-VINK notation [Kroe56] as follows:

$$\mathrm{CO_2(g)} + 2\mathrm{Ce}'_{\mathrm{Ce}} + \mathrm{V}_{\mathrm{O}}^{\bullet\bullet} \rightarrow 2\mathrm{Ce}_{\mathrm{Ce}}^{\times} + \mathrm{O}_{\mathrm{O}}^{\times} + \mathrm{CO(g)}\,. \qquad (6)$$

Depending on the experimental conditions, different reaction routes are possible, where the overall reaction path may be divided into different reaction steps. In relation to this, the reactive material and its macroscopic and microscopic structure play a decisive role. In general, reactive ceramic bodies in the macroscopic form of beads, foams or honeycomb structures, as exemplified in Figure 4, can be applied [Haus12]. The microscopic structure is that of a sintered solid sample, displaying pores, grain boundaries and a specific grain size.

Literature data indicate that, even in bulk ceria samples, surface processes dominate the Ce^{3+}/Ce^{4+} redox reaction in the first place, due to fast chemical diffusion of oxygen [Knob15]. Recent investigations showed a high surface concentration and a high stability of reactive surface Ce^{3+} ions over a wide range of temperature and of oxygen partial pressure on ceria [Chue12b, Zhao16]. Currently, Ce^{3+} ions and oxygen vacancies $\mathrm{V}_{\mathrm{O}}^{\bullet\bullet}$ are believed to be the active sites on ceria surfaces. NAMAI et al. [Nama03] reported hexagonally arranged surface oxygen ions, oxygen point defects and multiple oxygen defects at CeO_2 (111) surfaces visualized by non-contact atomic force microscopy as well as hopping of surface oxygen ions at room temperature (RT), at which also the complete re-oxidation of slightly reduced CeO_2 (111) surfaces occurred.

Costa-Nunes et al. [Cost05] investigated thin ceria films supported on yttria-stabilized zirconia (YSZ) with atomic force microscopy. In the films the ions are highly mobile at moderate temperatures, and the morphology of the films depends on the respective conditions of the gas environment which they have been exposed to.

For T- p_{O_2} conditions, which are relevant for the solar thermal redox reactions, however, the available data is still very fragmentary, especially regarding the surface oxygen exchange kinetics in the re-oxidation by CO_2 (or H_2O). Beside computer simulations on the reaction between CO_2 and $CeO_{2-\delta}$ based on DFT calculations (see i.e. [Hahn13] and [Chen13]), there are only a few recent experimental studies on this question.

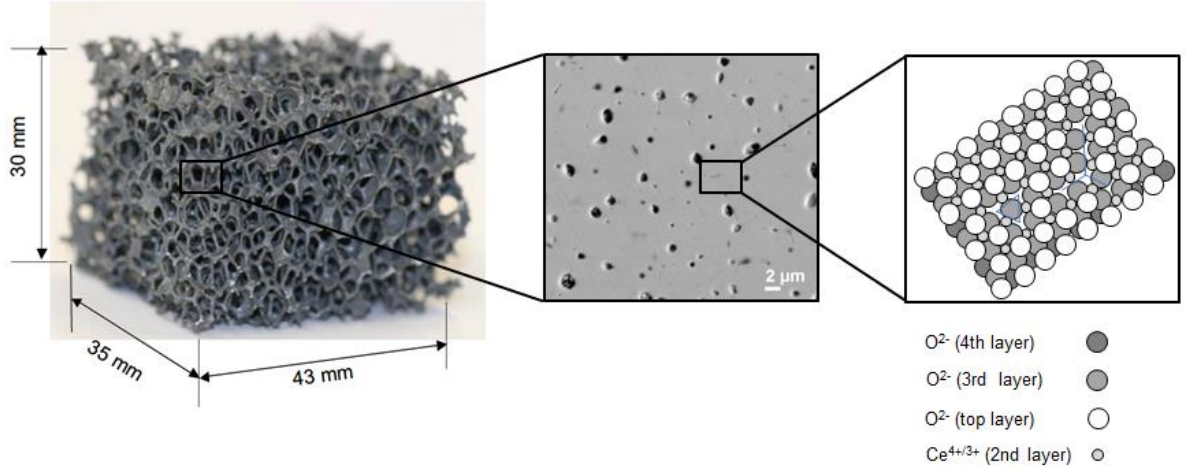

Figure 4. Schematic representation of the decisive role of the macroscopic and microscopic structure of the ceria redox material applied in solar-thermochemical splitting of water and/or carbon dioxide. The atomic structure of the respective ceria surface at the gas/solid interface has a crucial role in terms of the surface reaction. Scetch of the defective ceria surface adapted from [Nama03].

In principle, the in-operando analysis of the surface offers the possibility to follow the state of the surface as a function of the temperature, the oxygen activity and the enrichment/depletion of doping components or impurities during a reaction. Representing this type of experimental methodology, some recent work by the groups of Chueh and Eichhorn are exemplary [Zhan12, Feng14]. These in-operando/in-situ work, together with (older) ex-situ investigations with surface-sensitive methods such as XPS, UPS, HREELS [Pfau94] or LEIS [Kiln11] deliver experimental results, which contrast a considerable increase in the number of theoretical papers. For purely practical reasons it is not possible to give an exhaustive list here.

While these computer calculations are not well suited for a direct quantitative comparison with experimental data, they provide an excellent source for the selection of potentially rate-limiting steps in the reactions treated [Paie13].

Recent work on the system $CeO_{2-\delta}$ and $Ce_{1-x}M_xO_{2-\delta}$ (M = tri - and tetravalent dopants), which were carried out in the context of thermochemical cycling processes, aim primarily at the thermodynamic characterization of the redox system [Taka15, Bulf16, Dave16], at the design of the solar-heated reactor [Furl12, Acke14b], at the influence of cation dopants [LeGa13, Kuhn13, Call15], and pursue a primarily technically oriented objective. These works also reveal the gaps in the understanding of the observed phenomena.

The experimentally determined activation energies are treated only as process parameters in the process-oriented studies (see i.e. [Acke15]). The correlations with the kinetics and the thermodynamics of the responsible defects are only partially discussed. A more detailed discussion of classical models regarding the role of oxygen vacancies and electronic defects in the (exchange) reaction between O_2/CO_2 and $CeO_{2-\delta}$ can be found in section 4.3.

3 Research objective and outline

The present thesis focuses on experimental investigations of ceria, with carbon dioxide reduction and oxygen exchange being most important. As the redox kinetics of ceria-based materials is in general either controlled by surface exchange reactions or by bulk transport of oxygen, this work aims to provide the quantitative basis for improving the CO yield in CO_2 splitting using CeO_2-based redox systems by investigating oxygen exchange and transport. From the current state of research, the following critical problem complexes can be identified:

1. Surface reaction with carbon dioxide reduction, comparison to the oxygen exchange reaction, phenomenological description (K_O, D_O), interpretation of the rate constants, influence of the doping elements, influence of the oxygen partial pressure of the gas atmosphere, influence of the respective kinetic regime.

2. Tracer diffusion of oxygen in ceria, influence of targeted doping and doping through impurities, diffusion mechanism.

3. Diffusion in chemical non-equilibrium (chemical potential gradient at the gas/solid interface) from room temperature to $T = 800$ °C, possible influence of cation doping elements with respect to trapping, influence of oxygen vacancy concentration and possible defect complex formation.

The most direct method of measuring oxygen diffusivities and surface exchange coefficients in oxides is oxygen isotope exchange followed by Secondary Ion Mass Spectrometry (SIMS) depth profiling (IEDP) or cross section line scan (IELS). By utilizing oxygen isotope-enriched $^{18}O_2$ and $C^{18}O_2$ gas atmospheres and various experimental conditions this well established approach represents the core of the experimental work of this thesis.

After introducing in general the materials and methods employed in this work in chapter 2, the chapters 4 to 6 pursue the main research objectives. Chapter 4 discusses the current theory regarding defect structure and non-stoichiometry of cerium dioxide, oxygen diffusion in ceria and oxygen surface exchange from O_2 and CO_2 gas atmospheres.

In chapter 5 sample preparations, the experimental setup for isotope exchange utilizing $^{18}O_2$ and $C^{18}O_2$, the experimental realization of chemical equilibrium and non-equilibrium conditions and the applied secondary ion mass spectrometry and analysis are described in detail.

Chapter 6 is fully committed to the experimental findings and their thorough discussion, including subsequent calculations of relevant kinetic parameters and their interpretation. In the summary and conclusion part the most important findings of this work and their perspectives for upcoming studies are highlighted.

4 Theory and state of the art

4.1 Defect structure and non-stoichiometry of cerium dioxide

The perfect crystal structure of an ionic solid is defined by an error-free, periodically repeating spatial arrangement of the ions. This arrangement and the smallest repetitive structural motif are called grids and unit cells. Fully oxidized ceria crystallizes cubic face centered (f.c.c.) and has a fluorite structure. Ce^{4+} ions are located on the edges and in the center of the cubic unit cell. The oxygen ions lie on a cubic primitive sublattice of half the lattice constant. If one considers the arrangement of the Ce^{4+} ions as cubic close-packed, the positions of the oxygen ions correspond to the tetrahedral gaps [Trov02].

A deviation from the perfect crystal structure is accordingly an error in the grid and is referred to as a defect [Maie04]. In general defects in ionic crystals such as cerium dioxide can be classified as intrinsic or extrinsic. Intrinsic refers to defects related to thermal disorder or defects created by reaction between the solid and the surrounding gas atmosphere (i.e. redox processes). Extrinsic defects are formed by impurities or by the introduction of cation dopants due to charge compensation.

Furthermore, defects can be categorized into point defects (zero-dimensional) and spatially extended (multi-dimensional) defects. By the formation of point defects, each crystalline solid reaches a thermodynamically desirable state of lower free enthalpy G for temperatures $T > 0$ K. Point defects are thus unavoidable and their concentration is linked to the thermodynamic equilibrium [Maie04].

The three basic point defects found in oxides are vacant lattice sites (vacancies), interstitial ions, and - intentional or unintentional - introduced foreign ions (impurities or dopants). Point defects are not neutral to the regular lattice and must be compensated by an appropriate number of other point defects of opposite charge, maintaining the electro-neutrality, stoichiometry and mass of the system. Therefore, these point defects in ionic compounds always occur in oppositely charged, interlinked combinations and their concentrations are determined by disordering equilibria [Maie04]. Point defects in solids can be accurately described by the KRÖGER-VINK notation [Kroe56].

Regarding intrinsic type defects in cerium dioxide, three possible thermally generated intrinsic disorder reactions (SCHOTTKY -, FRENKEL - and anti-FRENKEL-type in Equations (7) to (9)), that do not involve exchange with the gas phase, can be deduced in KRÖGER-VINK notation [Kroe56] as follows, with ΔH_f being the respective defect formation enthalpy [Trov02]:

$$\mathrm{Ce}_{\mathrm{Ce}}^{\times} + 2\mathrm{O}_{\mathrm{O}}^{\times} \leftrightarrow \mathrm{V}_{\mathrm{Ce}}^{''''} + 2\mathrm{V}_{\mathrm{O}}^{\bullet\bullet} + \mathrm{CeO}_2 \qquad \Delta H_{\mathrm{f}} = 3.53\ \mathrm{eV}, \tag{7}$$

$$\mathrm{Ce}_{\mathrm{Ce}}^{\times} \leftrightarrow \mathrm{Ce}_{\mathrm{i}}^{\bullet\bullet\bullet\bullet} + \mathrm{V}_{\mathrm{Ce}}^{''''} \qquad \Delta H_{\mathrm{f}} = 11.11\ \mathrm{eV}, \tag{8}$$

$$\mathrm{O}_{\mathrm{O}}^{\times} \leftrightarrow \mathrm{O}_{\mathrm{i}}^{''} + \mathrm{V}_{\mathrm{O}}^{\bullet\bullet} \qquad \Delta H_{\mathrm{f}} = 3.2\ \mathrm{eV}. \tag{9}$$

The predominant defect category is the anti-FRENKEL-type (Eq. (9)), which leads to the formation of pairs of oxygen vacancies and interstitial oxygen ions. The concentration of these defects is in general low and they do not produce any deviation from the stoichiometric composition.

Another way to influence the defect concentrations of ceria, however, is to simply change the ambient oxygen activity by exposure to reducing gas atmospheres. According to Equation (3), oxides can be in equilibrium with their surrounding gas atmosphere by increasingly degrading oxygen from its lattice with increasing temperature and decreasing oxygen activity. The concentration of oxygen vacancies $\mathrm{V}_{\mathrm{O}}^{\bullet\bullet}$ in the crystal lattice is compensated by polarons localized on cerium cations $\mathrm{Ce}_{\mathrm{Ce}}^{'}$.

The corresponding law of mass action combines the defect concentrations with a temperature-dependent equilibrium constant $K_{\mathrm{red}} = \exp\left(-\frac{\Delta G_{\mathrm{red}}}{RT}\right)$ and can be written for Equation (3) as follows:

$$K_{\mathrm{red}} = \frac{a_{\mathrm{Ce}_{\mathrm{Ce}}^{'}}^{2} \cdot a_{\mathrm{V}_{\mathrm{O}}^{\bullet\bullet}} \cdot a_{\mathrm{O}_2}^{\frac{1}{2}}}{a_{\mathrm{Ce}_{\mathrm{Ce}}^{\times}}^{2} \cdot a_{\mathrm{O}_{\mathrm{O}}^{\times}}}. \tag{10}$$

As it is shown in the appendix section D.1, there is proportionality between the oxygen vacancy concentration $\mathrm{V}_{\mathrm{O}}^{\bullet\bullet}$ and the oxygen partial pressure p_{O_2}. The oxygen non-stoichiometry δ is thus proportional to $p_{\mathrm{O}_2}^{-\frac{1}{6}}$:

$$\delta \sim p_{\mathrm{O}_2}^{-\frac{1}{6}}. \tag{11}$$

However, this only applies to the model of isolated point defects with statistically distributed oxygen vacancies in the crystal lattice. In principle, the fluorite structure remains during partial reduction up to 2-δ = 1.651. But even when the deviation from oxygen stoichiometry is small, there is evidence in the literature that the defect structure of non-stoichiometric phases is more complex.

First measurements of the oxygen non-stoichiometry of ceria as a function of oxygen partial pressure where conducted by BEVAN and KORDIS as well as PANLENER et al. [Beva64, Panl75]. As early as 1975 PANLENER and co-workers discussed the formation of defect complexes in reduced $CeO_{2-\delta}$ because the observed proportionality between the oxygen non-stoichiometry and the oxygen partial pressure changed to a more general form of $\delta \sim p_{O_2}^{-n}$, even for small values of δ [Panl75].

Over the past decade, the group of WACHSMAN has been working intensively on the subject of bulk defect equilibria of cerium dioxide, investigating the oxygen non-stoichiometry as a function of oxygen partial pressure as well as the chemical expansion of ceria upon reduction (see i.e. [Dunc06, Bish09a, Bish09b]).

Isolated defects on the oxygen sublattice can interact to form defect complexes that are themselves new defects, which is related to an increasing concentration of oxygen vacancies. The defect complex is assumed to have a smaller volume then the isolated defects, which leads to less strain upon its formation. Furthermore, the defect complexes can neutralize local electrostatic charges by locating oppositely charged defects. BISHOP et al. discussed various defect complexes that can potentially form and found isolated defects and trimers composed of reduced cations and oxygen vacancies $\left(\mathrm{Ce}'_{\mathrm{Ce}}\mathrm{V}_{\mathrm{O}}^{\bullet\bullet}\mathrm{Ce}'_{\mathrm{Ce}}\right)^{\times}$ to be the most significant ones [Bish09b]. Other discussed defect complexes include dimers $\left(\mathrm{V}_{\mathrm{O}}^{\bullet\bullet}\mathrm{Ce}'_{\mathrm{Ce}}\right)^{\bullet}$ and hexamers $\left(4\mathrm{Ce}'_{\mathrm{Ce}}2\mathrm{V}_{\mathrm{O}}^{\bullet\bullet}\right)^{\times}$ [Bish09a]. The trimer consists of an oxygen vacancy and two reduced cerium cations. The formation and the corresponding mass action constant are given by:

$$2\mathrm{Ce}_{\mathrm{Ce}}^{\times} + \mathrm{O}_{\mathrm{O}}^{\times} \leftrightarrow \left(\mathrm{Ce}'_{\mathrm{Ce}}\mathrm{V}_{\mathrm{O}}^{\bullet\bullet}\mathrm{Ce}'_{\mathrm{Ce}}\right)^{\times} + \frac{1}{2}\mathrm{O}_2(\mathrm{g}), \tag{12}$$

$$K_{\mathrm{red}} = \frac{a_{\left(2\mathrm{Ce}'_{\mathrm{Ce}}\mathrm{V}_{\mathrm{O}}^{\bullet\bullet}\right)^{\times}} \cdot a_{\mathrm{O}_2}^{\frac{1}{2}}}{a_{\mathrm{Ce}_{\mathrm{Ce}}^{\times}}^{2} \cdot a_{\mathrm{O}_{\mathrm{O}}^{\times}}}. \tag{13}$$

As it is shown in the appendix section D.2, there is proportionality between the trimer concentration and the oxygen partial pressure, and the concentration of trimers $\left[\left(\mathrm{Ce}'_{\mathrm{Ce}}\mathrm{V}_{\mathrm{O}}^{\bullet\bullet}\mathrm{Ce}'_{\mathrm{Ce}}\right)^{\times}\right]$ is proportional to $p_{\mathrm{O}_2}^{-\frac{1}{2}}$:

$$\left[\left(\mathrm{Ce}'_{\mathrm{Ce}}\mathrm{V}_{\mathrm{O}}^{\bullet\bullet}\mathrm{Ce}'_{\mathrm{Ce}}\right)^{\times}\right] \sim p_{\mathrm{O}_2}^{-\frac{1}{2}}. \tag{14}$$

This slope is distinguishable from the slope for isolated oxygen vacancies in a $d\log\left[\left(\mathrm{Ce}'_{\mathrm{Ce}}\mathrm{V}_{\mathrm{O}}^{\bullet\bullet}\mathrm{Ce}'_{\mathrm{Ce}}\right)^{\times}\right]/d\log p_{\mathrm{O}_2}$ plot, leaving the possibility to effectively model the measured oxygen non-stoichiometry as a function of oxygen partial pressure. In principle, the often cited experimental work on the oxygen non-stoichiometry of ceria from BEVAN and KORDIS and PANLENER et al. [Beva64, Panl75] as shown in Figure 5 matches very well and defines the standard until today. Later experimental work [Wang98, Kim06, Bish09a] is usually only compared with it.

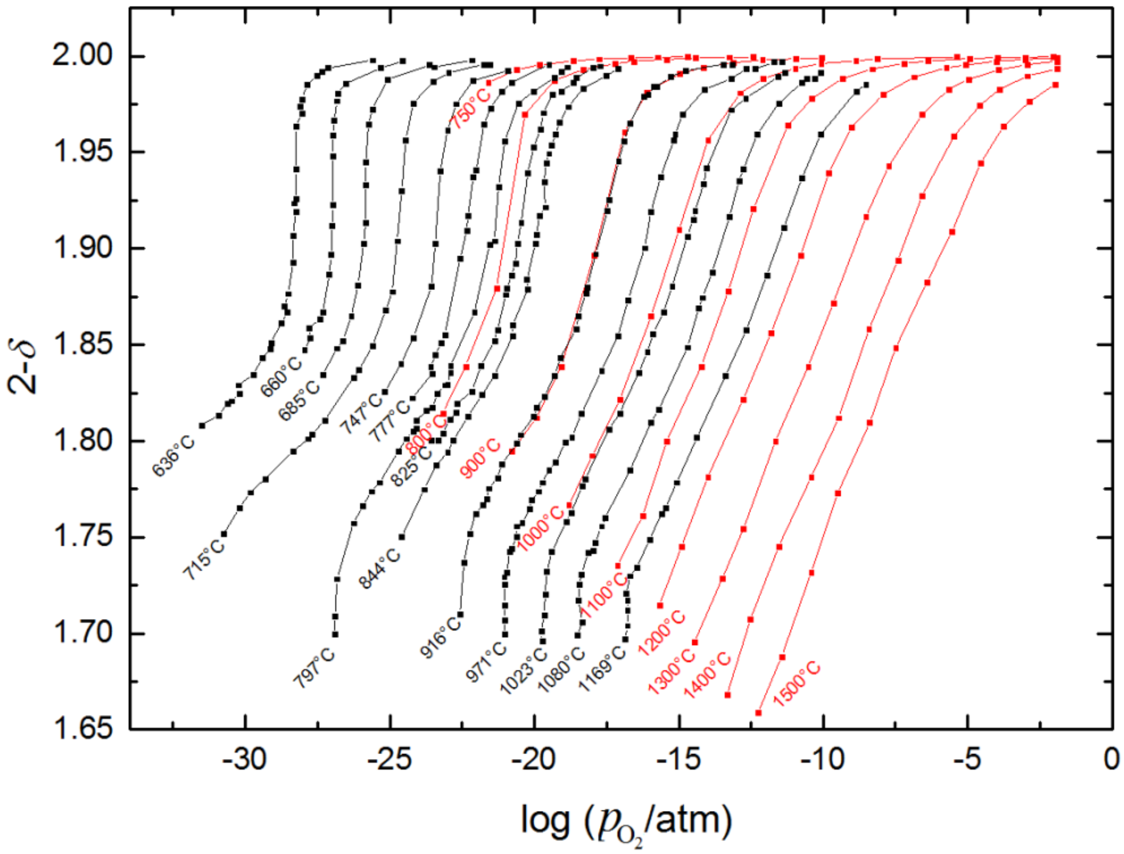

Figure 5. Isothermal plot of the measured oxygen non-stoichiometry δ of ceria in the temperature range T = 638 to T = 1500 °C, adapted from [Beva64] (black symbols) and [Panl75] (red symbols).

By intentionally introducing foreign cations into the crystal lattice (doping), point defect concentrations can be extrinsically influenced. Isovalent dopants (tetravalent dopants such as Zr^{4+} and Hf^{4+}) that have a neutral effective charge will not affect other point defect concentrations as long as they are ideally diluted, since no oppositely charged point defects are needed for compensation, i.e. for Zr-doping:

$$\mathrm{ZrO_2} \xrightarrow{\mathrm{CeO_2}} \mathrm{Zr}_{\mathrm{Ce}}^{\times} + 2\mathrm{O}_{\mathrm{O}}^{\times} . \tag{15}$$

The introduction of non-isovalent dopants results in compensating point defects that determine the properties of the doped material. Dopants with negative effective charge are called acceptors. Upon introduction of a lower-valent cation dopant such as di- and trivalent dopants, including i.e. Ca^{2+}, Mg^{2+}, Cu^{2+}, Sr^{2+}, Al^{3+}, Sc^{3+}, Ni^{2+}, Y^{3+}, La^{3+}, Sm^{3+} and Gd^{3+}, by its corresponding oxide in ceria, the negative excess charge of the acceptor is compensated by oxygen vacancies $\mathrm{V}_{\mathrm{O}}^{\bullet\bullet}$, i.e. for Ca- and Y-doping:

$$\mathrm{CaO} \xrightarrow{\mathrm{CeO_2}} \mathrm{Ca}_{\mathrm{Ce}}'' + \mathrm{V}_{\mathrm{O}}^{\bullet\bullet} + \mathrm{O}_{\mathrm{O}}^{\times} , \tag{16}$$

$$\mathrm{Y_2O_3} \xrightarrow{\mathrm{CeO_2}} 2\mathrm{Y}_{\mathrm{Ce}}' + \mathrm{V}_{\mathrm{O}}^{\bullet\bullet} + 3\mathrm{O}_{\mathrm{O}}^{\times} . \tag{17}$$

The resulting oxygen vacancies strongly influence the ionic transport properties. Doping is thus a powerful method to extrinsically adjust the defect concentrations and the resulting material properties according to the present needs.

The experimental work done on trivalent-doped ceria focuses on non-stoichiometry, chemical expansion, transport properties and defect structure, and includes Y-doped ceria, Gd-doped ceria and Sm-doped ceria [Cale84, Wang97, Wang98, Zhou07b, Bish09a, Bish09b]. In principle di - and trivalent dopants do not promote the oxidative splitting step in STCC, as two electrons must be promoted into the high energy Ce f-band during reduction if the oxygen vacancies are to store sufficient energy to drive the splitting step [Muhi17a]. Nevertheless, the more acceptors introduced into cerium dioxide up to a critical concentration, the higher is the ionic conductivity based on the migration of oxygen vacancies, which will be discussed in section 4.2. The oxygen deficiency caused by doping is correspondingly represented in the thermogravimetric measurements, as shown for example in Figure 6 for Gd-doped ceria. BISHOP et al. [Bish09a] discussed, based on their thermogravimetric measurements, the formation of mixed trimers from isolated defects in $Ce_{1-x}Gd_xO_{2-0.5x-\delta}$ (x = 0.1, 0.2), according to

$$\mathrm{Gd}'_{\mathrm{Ce}} + \mathrm{Ce}^{\times}_{\mathrm{Ce}} + \mathrm{O}^{\times}_{\mathrm{O}} \leftrightarrow \left(\mathrm{Gd}'_{\mathrm{Ce}}\mathrm{V}^{\bullet\bullet}_{\mathrm{O}}\mathrm{Ce}'_{\mathrm{Ce}}\right)^{\times} + \frac{1}{2}\mathrm{O}_2(\mathrm{g})\,, \tag{18}$$

and found that the mixed trimer concentration cannot be separated from the isolated oxygen vacancy concentration using thermogravimetric derived non-stoichiometry data and mass action-based models.

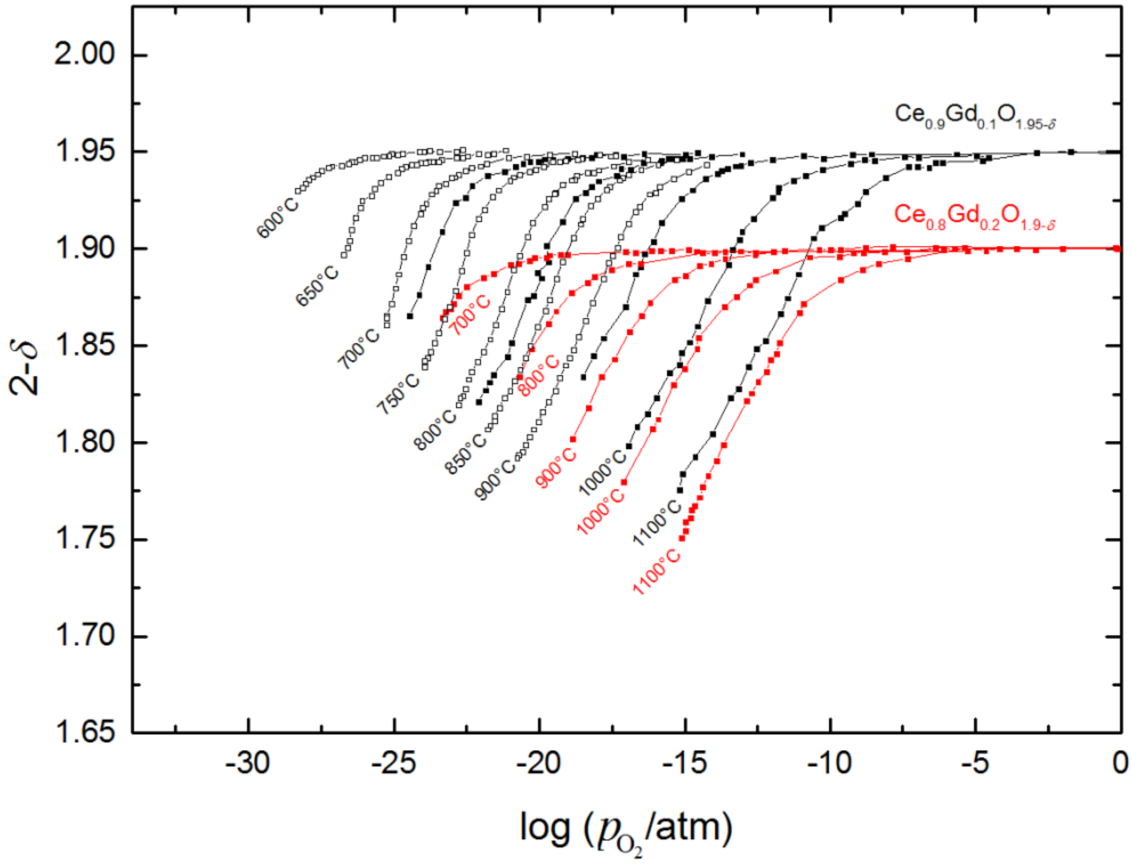

Figure 6. Isothermal plot of the measured oxygen non-stoichiometry δ of $Ce_{1-x}Gd_xO_{2-0.5x-\delta}$ (x = 0.1, 0.2) in the temperature range $T = 600$ to $T = 1100$ °C adapted from [Wang97, Wang98, Bish09a, Bish09b].

Recently the group of MARTIN has been doing theoretical work on the subject of defect distribution and interaction in lower-valent-doped non-stoichiometric ceria, namely Y - and Gd-doped ceria (see i.e. [Grie14], [Grie16] and [Grie17]). In principle they were able to model the $\delta - p_{O_2}$ relations including the variation of the slopes and the flattening of the curves at low oxygen partial pressures based on different pair interactions, which are discussed in general in section 4.2.

Doping with ZrO_2 as given in Equation (15) is promising with regard to the oxygen dissolution during the reduction, which increases. The solubility of zirconium in the cubic cerium dioxide is given until 20 mol-%.

The numerous experimental and theoretical work focus primarily on structural changes in the ceria-zirconia crystal structure, the improved reduction ability, defect chemistry and thermodynamic characterization [Forn96, Bald97, Kim06, Zhou07a, Kuhn13, Hao14, Bulf16].

Thermodynamic characterization studies were done, for example, by KUHN et al., ZHOU et al. and HAO et al. [Zhou07a, Kuhn13, Hao14]. Measurements of the oxygen non-stoichiometry of $Ce_{1-x}Zr_xO_{2-\delta}$ as a function of oxygen partial pressure as done for example by HAO et al. and KUHN et al. (shown in Figures 7 and 8) show a higher degree of reduction compared to the undoped cerium dioxide. The zirconium ions incorporated into the ceria structure improve the reduction properties, increasing the release of oxygen, and studies showed that the degree of reduction increases with increasing zirconium concentration.

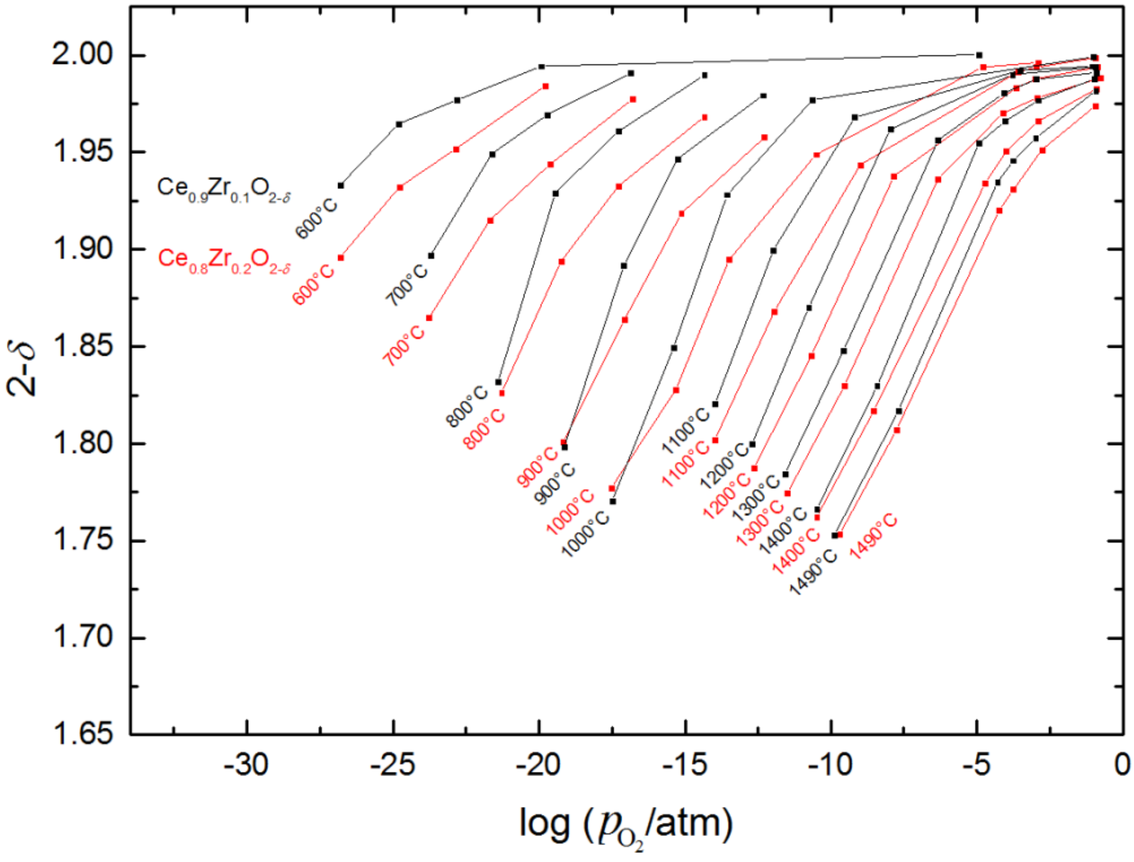

Figure 7. Isothermal plot of the measured oxygen non-stoichiometry δ of $Ce_{1-x}Zr_xO_{2-\delta}$ (x = 0.1, 0.2) in the temperature range T = 600 to T = 1490 °C adapted from [Hao14].

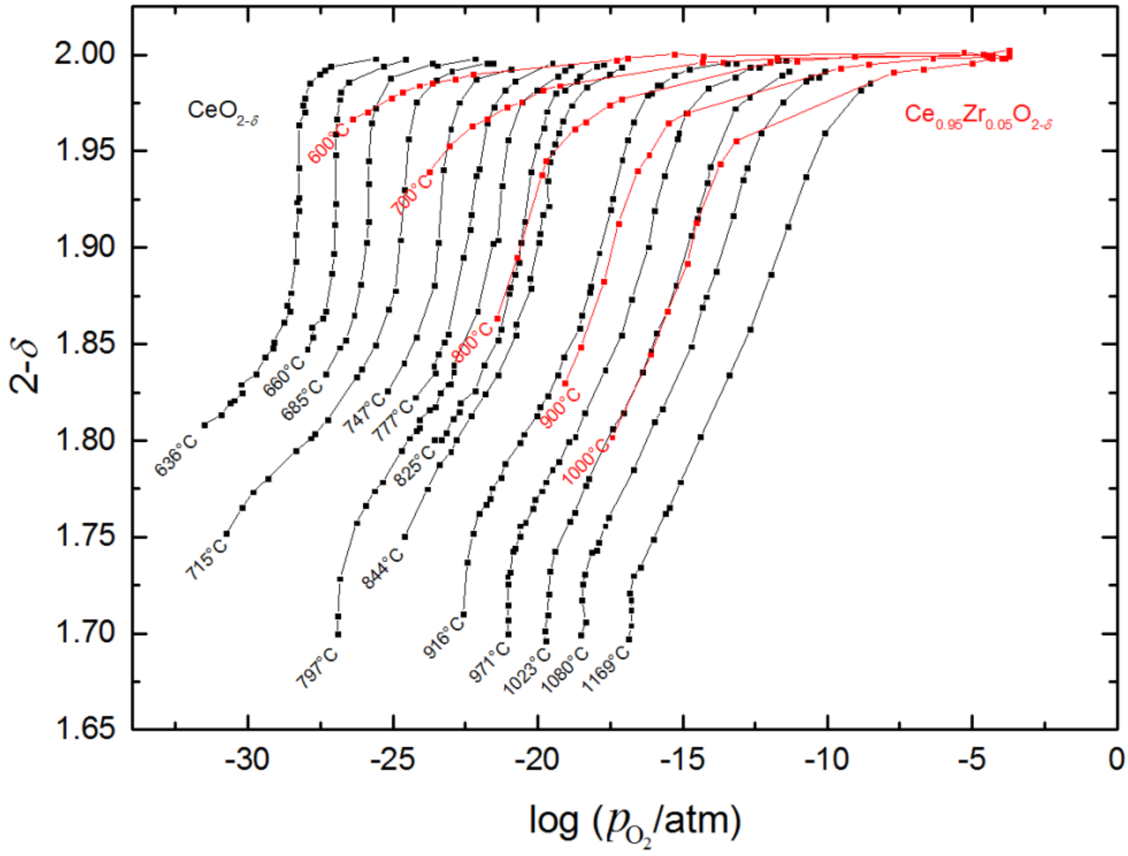

Figure 8. Comparison of the isothermal plot of the measured oxygen non-stoichiometry δ of undoped ceria and $Ce_{0.95}Zr_{0.05}O_{2-\delta}$ in the temperature range T = 600 to T = 1169 °C adapted from [Kuhn13] and [Beva64].

The improvement is attributed to the smaller ionic radius of Zr^{4+} which compensates for stresses due to volume changes in the lattice caused by the larger Ce^{3+} ions. In addition, the smaller Zr^{4+} ion should prefer a 7-fold coordination with oxygen in contrast to the 8-fold coordination as in the CaF_2-structure, which promotes the formation of oxygen vacancies (see i.e. [Bald97] and [Kuhn13]).

In summary, all studies initially show that the standard enthalpies of formation and the standard entropy of redox reactions of ceria-zirconia solid solutions are lower than those of the redox reaction of undoped cerium dioxide. Furthermore, experimental studies on the STCC performance of ceria-zirconia solid solutions could show an initial increase and subsequent decrease in the splitting performance with increasing zirconium content [Sche13, Taka15]. Theoretical calculations by MUHICH et al. [Muhi17a] explained the increased oxygen exchange capacity with stored energy in tensiley strained Zr-O bonds which is released upon oxygen vacancy formation and depends on the number of oxygen anions coordinated to zirconium dopants (and therefore on the dopant concentration).

4.2 Transport properties and oxygen diffusion in cerium dioxide

Electrical conduction and ionic transport are mainly determined by the presence, concentration and mobility of defects in the crystal lattice, as previously discussed in section 4.1. In general, ceria can be classified as a mixed conductor (MIEC) showing both electronic and ionic conduction [Trov02]. At high temperatures and/or low oxygen partial pressures, ceria behaves as an n-type semiconductor and electrons are the primary charge carriers (since $\left[\mathrm{Ce}'_{\mathrm{Ce}}\right] \approx \left[\mathrm{V}_{\mathrm{O}}^{\bullet\bullet}\right] >> \left[\mathrm{h}^{\bullet}\right]$). According to Equation (3) the equivalent to the presence of $\mathrm{Ce}'_{\mathrm{Ce}}$ is the electronic defect e' which is accompanied by the formation of an ionic defect, the oxygen vacancy $\mathrm{V}_{\mathrm{O}}^{\bullet\bullet}$, with $2\left[\mathrm{Ce}'_{\mathrm{Ce}}\right] = 2\left[\mathrm{e}'\right] = \left[\mathrm{V}_{\mathrm{O}}^{\bullet\bullet}\right]$, both representing the majority charge carriers. In cerium dioxide, electronic conduction is not described by a band model as known from semiconductor physics, but occurs instead through the formation of small polarons, where the electron is self-trapped at a given lattice site (Ce^{4+}), forming Ce^{3+} ions, and can move only by an activated hopping process similar to that known from ionic diffusion [Paie13].

Ionic conductivity in pure ceria results from intrinsic disorder generated by three possible defect mechanisms described in Equations (7) - (9) and is negligible as the experimentally observed values strongly depends on the level of impurities, as described in section 4.1. By intentionally introducing foreign ions into the ionic crystal (doping), defect concentrations can be extrinsically influenced.

Ionic conductivity is in general linked to the diffusion coefficient D_{i} of ionic carriers via the NERNST-EINSTEIN relation:

$$D_{\mathrm{i}} = \frac{\kappa_{\mathrm{i}} k_{\mathrm{B}} T}{c_{\mathrm{i}} q_{\mathrm{i}}^{2}}, \tag{19}$$

where κ_{i} is the ionic conductivity, k_{B} is the BOLTZMANN constant, T the temperature, c_{i} the concentration of the ionic carriers i and q_{i} their charge [Maie04].

Two basic concepts can be used to describe the diffusion of a species in the bulk of an ionic crystal. A macroscopic definition of diffusion is usually done by FICK's laws, which serve for the experimental determination of diffusion coefficients. The consideration of the mechanistic motion of single atoms on the basis of the Random-Walk theory allows the description of the diffusion in bulk at the microscopic level [Mann68, Mehr07].

The first FICK's law describes the particle current density j_i of a species i in one dimension through a defined area per unit time t:

$$j_\mathrm{i} = -D_\mathrm{i} \frac{\partial c_\mathrm{i}}{\partial x} . \tag{20}$$

Here, c_i denotes the concentration of the species i and x the location coordinate. The proportionality constant between the particle current density and the concentration gradient is the diffusion coefficient D_i. If the number of diffusing species i remains constant during the diffusion process, it can be determined using the continuity Equation, which is defined for diffusion in one dimension:

$$-\frac{\partial j_\mathrm{i}}{\partial x} = \frac{\partial c_\mathrm{i}}{\partial t} . \tag{21}$$

The second FICK's law is formed by combining Equations (20) and (21):

$$\frac{\partial c_\mathrm{i}}{\partial t} = \frac{\partial}{\partial x}\left(D_\mathrm{i} \frac{\partial c_\mathrm{i}}{\partial x} \right). \tag{22}$$

If the diffusion coefficient is concentration-independent and thus independent of location, the following relation applies:

$$\frac{\partial c_\mathrm{i}}{\partial t} = D_\mathrm{i} \frac{\partial^2 c_\mathrm{i}}{\partial x^2} . \tag{23}$$

This Equation is a partial differential Equation of the second order. It describes the location and time-dependent concentration of the species i. In general analytical solutions are possible through relevant initial boundary conditions.

The temperature dependence of the diffusion coefficient D_i is described by an ARRHENIUS Equation of the form:

$$D_\mathrm{i} = D_\mathrm{i}^0 \exp\left(-\frac{\Delta H_\mathrm{a}}{k_\mathrm{B} T} \right), \tag{24}$$

where D_i^0 is the pre-exponential factor, which contains terms related to the concentration of ionic carriers. ΔH_a is the overall activation enthalpy of diffusion, which includes terms related to the migration, defect formation and defect association.

The actual driving force of diffusion is not the concentration gradient $\frac{\partial c_{\mathrm{i}}}{\partial x}$ (see Equation (20)), but a gradient in the chemical potential μ_{i} of the species i within the solid. The chemical potential of species i is defined as the partial derivative of the free enthalpy G by the amount n_{i} of species i:

$$\mu_{\mathrm{i}} = \left(\frac{\partial G}{\partial n_{\mathrm{i}}}\right). \tag{25}$$

As a result, all mobile species diffuse, changing the local chemical composition of the solid until the gradient is balanced and the thermodynamic equilibrium is reached. If tracers are used to determine the self-diffusion, which are chemically identical isotopes to the elements of the observed solid, the driving force of the diffusion is purely entropic nature.

In order to understand diffusion processes at the atomic level, the following mechanistic processes of the diffusion of ions in the solid state have to be considered. In any crystal, there is a regular array of lattice sites which are energetically favored positions for atoms. The ordered crystal lattice restricts the possible atom motions and allows a simple description of each specific atom displacement. The basics assumption made to explain diffusion is that each diffusing atom makes a series of jumps between the various equilibrium lattice sites, which are in random directions [Mann68, Mehr07]. The mean square displacement $\left\langle x_{\mathrm{i}}^{2}\right\rangle$ of the diffusing species i in one dimension is given by the product of the one-dimensional diffusion coefficient D_{i} and the time interval t:

$$\left\langle x_{\mathrm{i}}^{2}\right\rangle = 2D_{\mathrm{i}}t\,. \tag{26}$$

The diffusion in isotropic three-dimensional cubic crystal systems can be described by the mean total displacement of the diffuser in isotropic media $\left\langle R_{\mathrm{i}}^{2}\right\rangle$:

$$\left\langle R_{\mathrm{i}}^{2}\right\rangle = 6D_{\mathrm{i}}t\,. \tag{27}$$

According to the random walk theory, the mean total displacement of a diffuser that overcomes N uncorrelated jumps over a distance x is given by:

$$\left\langle R_{\mathrm{i}}^{2}\right\rangle = Nx^{2}\,. \tag{28}$$

With the introduction of the jump rate Γ_{i} of a particle to one of its W neighboring sites in a cubic ion crystal $\Gamma_{\mathrm{i}} W = \frac{N}{t}$, we obtain with Equations (27) and (28):

$$D_{\mathrm{i}} = \frac{x^2}{6} W \Gamma_{\mathrm{i}} . \tag{29}$$

The jump rate can be described by the ARRHENIUS Equation with the activation enthalpy ΔH_a:

$$\Gamma_{\mathrm{i}} = \nu \exp\left(\frac{\Delta H_{\mathrm{a}}}{k_{\mathrm{B}} T} \right), \tag{30}$$

with v being the attempt frequency of all oxygen vacancies or oxygen ions to jump to one nearest neighbor site. Combining Equations (29) and (30) yields for the pre-exponential factor D_{i}^0 as given in Equation (24):

$$D_{\mathrm{i}}^0 = \frac{x^2}{6} W \nu . \tag{31}$$

The conductivity of an oxygen ion conductor as described by Equation (19) can be defined for both oxygen ions and vacancies. The absolute value of the oxygen ion charge is then equal to the KRÖGER-VINK charge of the oxygen vacancies. Therefore the diffusion coefficients of the ionic carriers - here being oxygen ions $D_{\mathrm{O}^{2-}}$ and vacancies $D_{\mathrm{V}_{\mathrm{O}}^{\bullet\bullet}}$ - are related in the following way [Koet17]:

$$D_{\mathrm{O}^{2-}} = \frac{\left[\mathrm{V}_{\mathrm{O}}^{\bullet\bullet}\right]}{\left[\mathrm{O}^{2-}\right]} D_{\mathrm{V}_{\mathrm{O}}^{\bullet\bullet}} , \tag{32}$$

with $\left[\mathrm{O}^{2-}\right]$ and $\left[\mathrm{V}_{\mathrm{O}}^{\bullet\bullet}\right]$ being the concentrations of oxygen ions and oxygen vacancies. Determination of the defect diffusion coefficient (here: $D_{\mathrm{V}_{\mathrm{O}}^{\bullet\bullet}}$) requires thus knowledge of the defect concentration. In the case of the introduction of a lower-valent dopant (confer Equations (16) and (17)) the defect concentration can be estimated with reference to the electroneutrality condition $2\left[\mathrm{V}_{\mathrm{O}}^{\bullet\bullet}\right] = \left[\mathrm{Me}_{\mathrm{Ce}}'\right]$ in the following way [Kami00]:

$$D_{\mathrm{O}^{2-}} \sim \left[\mathrm{Me}_{\mathrm{Ce}}'\right] D_{\mathrm{V}_{\mathrm{O}}^{\bullet\bullet}} . \tag{33}$$

The diffusion coefficients discussed above are not directly accessible experimentally to measurement and are referred to as microscopic diffusion coefficients. Due to the requirement of electroneutrality the charge carriers cannot simply be moved through the solid, instead, the electroneutrality problem leads to the measurement of three respective macroscopic diffusion coefficients that can be differentiated according to MAIER [Maie04] in the following way.

In a stationary conductivity experiment a flux of ions within the oxide solid is maintained when an equivalent electron flux passes through an external circuit and the measured conductivity is the sum of electronic and ionic conductivities. According to Equation (19) it is then possible to convert the measured oxygen ion conductivity into a diffusion coefficient, being the ionic self-diffusion coefficient $D^{Q}_{\mathrm{O}^{2-}}$.

A second approach consists of exchanging the ambient oxygen surrounding an oxide (being primarily $^{16}O_2$) with gas enriched with oxygen isotopes (either $^{17}O_2$ or $^{18}O_2$) which behave chemically identical, but make up a tracer gradient between the solid and the gas atmosphere. The chemical composition is not altered, where it is important to avoid stoichiometric gradients. The consequence is a tracer exchange driven by tracer diffusion which can be characterized as counterdiffusion of the oxygen isotopes, being purely of entropic nature. The determined parameter is the tracer diffusion coefficient $D^{*}_{\mathrm{O}^{2-}}$ which reflects the self-diffusion coefficient of the oxygen ions.

The third approach highlights the diffusion kinetics of composition changes of oxide compounds with a chemical potential gradient, the chemical diffusion coefficient $\tilde{D}_{\mathrm{O}}$, which, for ionic compounds, formally characterizes a charge-neutral ambipolar diffusion process of at least two chemically different charged particles. Here the diffusion of oxygen takes place as a result of coupled transport of O^{2-} and $2e^{-}$ in opposite directions. As a consequence, $\tilde{D}_{\mathrm{O}}$ is going to be of the order of magnitude of the defect diffusion coefficients and represents a combination of ionic and electronic defect diffusivities. A further discussion on the interrelation of the three macroscopic diffusion coefficients can be found in appendix E.1.

Further complication arises from the possibility of defect interaction, as described in section 4.1, which interferes with matter transport, ordering of oxygen vacancies and formation of defect clusters, or a modified jump probability of the oxygen vacancies. In the simplest case of defect association oxygen vacancies are not free and randomly distributed, but linked to dopant cations instead.

Therefore the most studied defect clusters have been those formed by acceptor dopant cations and oxygen vacancies [Moge00, Trov02, Mehr07]. This association (as given in Equation (18)) is mainly due to the coulombic attraction of the defects caused by their effective charges in the lattice. The oxygen vacancies are trapped or immobilized by the almost immobile dopants and thereby the concentration of free vacancies is reduced. This may be taken into account by modifying the activation enthalpy of Equation (24) by another enthalpy contribution of formation of associated defects (association enthalpy), where there are dependencies on the dopant fraction and type of dopant. When the binding energy is strong, full association can persist to very high temperatures.

Experimentally derived electrical conductivity data of ceria and ceria-based materials have been reported for example by EGUCHI et al. for CeO_2, $Ce_{0.8}Sm_{0.2}O_{1.9}$, $Ce_{0.8}Y_{0.2}O_{1.9}$ and $Ce_{0.8}Gd_{0.2}O_{1.9}$ [Eguc92] and by HUANG et al. for CeO_2, $Ce_{0.83}Sm_{0.17}O_{1.915}$ and $Ce_{0.91}Ca_{0.09}O_{1.91}$ [Huan97]. Oxygen ion conductivity depends on the concentration, charge and mobility of the carriers. High values of conductivity were correlated with minimum binding energy of the oxygen vacancy with dopant cations. A minimum in the binding energy is predicted when the dopant and the host radii are the same [Trov02]. High ionic conductivities are observed for trivalent dopants such as Gd, Eu and Sm and divalent dopants such as Ca. The behavior of ionic conduction with dopant concentration depends on several factors. In general it increases with the number of oxygen vacancies (as can be deduced by combining Equations (19) and (32)) as a consequence of a low value for the migration enthalpy ΔH_m. The latter depends on the oxygen binding energy in the lattice and the free volume through which the oxide ions migrate. However, experimental findings imply that the conductivity is not simply proportional to the concentration of oxygen vacancies, but that it goes through a maximum [Wang81, Fabe89, Huan97, Dikm98]. The most recent and comprehensive discussion of this phenomenon is given by KOETTGEN and co-workers [Koet18], which aims to explain the relationship between defect interactions at the microscopic level and the macroscopic oxygen ion conductivity in doped ceria.

Experimental data of oxygen diffusion (tracer diffusion or chemical diffusion) in (bulk) ceria and ceria-related materials are relatively rare. They have been reported for example by KAMIYA et al. for oxygen tracer diffusion in CeO_2 [Kami98, Kami00], by FLOYD et al. for oxygen tracer diffusion in CeO_2, $Ce_{0.9}Y_{0.1}O_{1.95}$, $Ce_{0.8}Y_{0.2}O_{1.9}$ and $Ce_{0.6}Y_{0.4}O_{1.8}$ [Floy73], by MANNING et al. for oxygen tracer diffusion in $Ce_{0.9}Gd_{0.1}O_{1.95}$ [Mann97], by RUIZ-TREJO et al. for oxygen tracer diffusion in $Ce_{0.69}Gd_{0.31}O_{1.85}$ [Ruiz98] and by MILLOT et al. for chemical diffusion of oxygen in $CeO_{1.9837}$, $CeO_{1.965}$, $CeO_{1.919}$, $CeO_{1.8681}$, $CeO_{1.8135}$ and $CeO_{1.7504}$ [Mill84]. In principle, oxygen tracer diffusion can be distinguished in extrinsic and intrinsic diffusion. In the extrinsic regime, which is also referred to as a "low temperature" regime, the measured oxygen diffusion coefficient is controlled by aliovalent dopants or impurities which introduce extrinsic oxygen vacancies as given in Equations (16) and (17), so that the magnitude of the measured diffusion coefficient depends on the defect concentration as given by Equation (32). At higher temperatures ($T \geq 1000$ °C) the region of true intrinsic diffusive behavior of undoped ceria can be found, where the measured oxygen diffusion coefficient is controlled by thermally generated oxygen vacancies [Kami98, Kami00]. In the case of chemical diffusion as studied by MILLOT and DE MIERRY [Mill84] a dependency of the measured chemical diffusion coefficient of oxygen on the non-stoichiometry δ of $CeO_{2-\delta}$ at constant temperature was found, with a maximum value of $\tilde{D}_{\mathrm{O}}$ being given for $CeO_{1.8135}$ at $T = 971$ °C.

As computer modeling techniques are now well-established in the field of solid state chemistry, they have been applied to studies of structures, energetics and dynamics of a variety of materials on the atomic level. As early as 1982 KILNER and WATERS [Kiln82] calculated the effect of association of dopant cations and oxygen vacancies on the free vacancy concentration in ceria. BUTLER and others [Butl83] carried out computer simulations of dopant-vacancy clusters, in which the binding energy was calculated for divalent and trivalent dopants (Sc^{3+}, Y^{3+}, Gd^{3+}, Ce^{3+}, La^{3+}, Mg^{2+}, Ca^{2+}) in doped ceria and the energy change for association of oxygen vacancies and dopant cations at nearest-neighbor positions was evaluated.

In recent years further work concentrated on other possible pair interactions such as vacancy-vacancy-interaction, polaron-vacancy-interaction, polaron-polaron-interaction, dopant-dopant-interactions and dopant-polaron-interactions. It focuses mainly on computer simulation based calculations such as kinetic Monte Carlo simulations (KMC), molecular dynamics simulations (MD) and density functional theory based calculations (DFT) [Adle93a, Adle93b, Pryd95, Bald97, Meye97, Inab99, Bald00, Haya00, Mart06, Naka09, Grop12, Gries14, Yuan15, Gries16, Gries17a, Gries17b, Gries18, Koet17, Koet18]. In principle these work aims to understand the experimentally found dependencies of the transport properties such as conductivity and diffusivity on the dopant fraction and type of dopant in stoichiometric and non-stoichiometric ceria (with the contribution of additional oxygen vacancies in the crystal lattice due to reduction for the latter case).

The general interpretation of the observed conductivity data is confirmed due to these calculations and the results show also that the ionic size has a large effect on ionic conductivity. Further it is widely accepted now that the migration of oxygen in ceria and ceria-related materials takes places via oxygen vacancy hopping and that the presence of dopants as well as other defects in the crystal lattice changes the migration barrier, which is then referred to as trapping and blocking [Gries18, Koet18]. The activation energy for oxygen migration can be estimated using atomistic calculations, where it is assumed that an oxide ion migrates to a nearest-neighbor vacant site along a linear path. An energy profile can be determined by simulating the oxide ion at a number of intermediate positions along this migration path. The activation energy is finally obtained as the difference between the maximum energy and the energy of the starting configuration. A comprehensive summary of experimentally derived activation enthalpies (extracted from conductivity measurements) as well as calculated activation energies is given by KOETTGEN et al. in [Koet18], sections 2.3 and 4.4.

4.3 Oxygen surface exchange from O_2 and CO_2 gas atmospheres

The respective $CeO_{2-\delta}$ surface at the gas/solid interface has a crucial role in terms of the surface reaction for CO_2 splitting (Equation (6)), as previously discussed in section 2.3. The exchange and incorporation of oxygen is hereby considered as fundamental reaction, which is extensively discussed in the respective literature [Mann97, Maie00, Leon02, DeSo06, Merk08, Chue12, Scha19]. The surface reaction of oxygen incorporation, in particular, is made up of several complex individual steps [Maie04]. First the oxygen has to be transported within the gas phase, which is generally a rapid process. Then it must be adsorbed, dissociated, ionized and enter the solid. Consideration of the various oxygen species that have been proposed to exist on oxide surfaces indicates that one possible pathway for the forward reaction is [DeSo05]:

$$\mathrm{O_2(g) + S_{ad} \rightarrow O_2(ad)}, \tag{34}$$

$$\mathrm{O_2(ad) + e' \rightarrow O_2'(ad)}, \tag{35}$$

$$\mathrm{O_2'(ad) + e' + S_{ad} \rightarrow 2O'(ad)}, \tag{36}$$

$$\mathrm{O'(ad) + e' \rightarrow O''(ad)}, \tag{37}$$

$$\mathrm{O''(ad)} + \mathrm{V_O^{\bullet\bullet}} \rightarrow \mathrm{O_O^x} + \mathrm{S_{ad}}\,. \tag{38}$$

The reaction thus involves the adsorption and dissociation of oxygen molecules on the surface (S_{ad}), the reaction with an oxygen vacancy $\mathrm{V_O^{\bullet\bullet}}$ and the transfer of oxygen ions through the surface, in addition to several charge transfer steps. These are required to take place before dissociation because the dissociation energy is about 5 eV for O_2, but very much lower for O_2^- and O_2^{2-}. It is also discussed that steps (37) and (38) have to be in one step since O^{2-}(ad) is not stable at the surface [DeSo05, Paie13, Scha19].

As a consequence of this proposed pathway the most likely rate determining step (rds) is charge transfer leading to dissociation. According to BODENSTEIN´s principle one step in the pathway is assumed to be rate determining and all pre - and succeeding reaction steps are treated as being at quasi-equilibrium. The rate of the overall process is thus given by the rate of the rate determining step [Maie98, DeSo06].

In principle it is then possible to represent the whole reaction scheme (34) - (38) in the form of a network of elementary steps in parallel and series [Maie04]. The network concentrates on the rate determining step, if the rate constants differ sufficiently. Limiting cases here are situations close to and far from equilibrium. The incorporation reaction of oxygen (Equations (34) - (38)) can thus be considered as a serial coupling of surface reaction (incorporation into the first layer of the solid at $x = 0$) and a transport step:

$$\mathrm{A} \leftrightarrow \mathrm{B}(x=0) \leftrightarrow \mathrm{B}(x>0)\,. \tag{39}$$

If the surface reaction is sufficiently fast the surface concentration $[\mathrm{B}]$ at $x=0$ is in equilibrium with the preceding steps. If the diffusion is much more rapid than the surface reaction, $[\mathrm{B}]$ at $x = 0$ is in equilibrium with $[\mathrm{B}]$ at $x > 0$, meaning homogenous concentration profiles within the solid oxide. Both limiting cases are defining the possible kinetic regimes of oxygen exchange from a gas phase to an oxide solid. In reality, the rate determining step is located within the reaction $\mathrm{A} \leftrightarrow \mathrm{B}(x=0)$ [Maie04].

In contrast to the diffusion case, where the proportionality constant between the particle current density and the concentration gradient is the diffusion coefficient D_i as represented by Equation (20), the respective kinetic parameter of the surface reaction, the surface exchange coefficient K_i of the species i, is understood to be the ratio of the flux to the concentration difference Δc_i at the first layer of the bulk at $x = 0$ [Maie00, Maie04, DeSo06, Fiel16]:

$$j_\mathrm{i}(x=0) = -K_\mathrm{i}\Delta c_\mathrm{i}(x=0)\,. \tag{40}$$

In comparison with diffusion the surface exchange reaction as outlined in the whole reaction scheme (34) - (38) is not well understood at the atomistic level and as a result no atomistic expression equivalent to Equations (29) - (31) for the diffusion case exists [DeSo06]. The phenomenological Equation (40) defines K_i without recurring to any microscopic mechanism [Fiel16].

Depending on the experimental conditions three respective macroscopic surface exchange coefficients $K^{Q}_{\mathrm{O}^{2-}}$, $K^{*}_{\mathrm{O}^{2-}}$, $\tilde{K}_\mathrm{O}$ can be differentiated in analogy to the different macroscopic diffusion coefficients according to MAIER [Maie04]. Equation (40) is only valid for surface reactions at $x = 0$, meaning that the surface exchange coefficient K_O depends on the defect chemistry of the surface only.

MAIER proposed a relation between the surface exchange coefficient K_i and the (equilibrium) exchange rate $\Re^{0}_\mathrm{i}$ (being a measure of the dynamics at equilibrium, quantifying defect chemical reactions at the interface, and which can be interpreted as an exchange current density) of the rate determining step in the consecutive reaction sequence at the gas/solid interface [Maie98, Maie00, Maie04]:

$$\frac{K_\mathrm{i}}{\Delta x} = \frac{\Re^{0}_\mathrm{i}}{c_\mathrm{i}(x=0)} w_\mathrm{i}(x=0)\,, \tag{41}$$

where $c_\mathrm{i}(x = 0)$ is the concentration of the species i (here oxygen) near the surface and $w_\mathrm{i}(x=0) = \frac{c_\mathrm{i}(x=0)}{RT}\left.\frac{\partial \mu_\mathrm{i}}{\partial c_\mathrm{i}}\right|_{x=0}$ is the thermodynamic factor near the surface. The elementary distance Δx appears here, since K_O was defined as $-\frac{j_\mathrm{O}(x=0)}{\Delta c_\mathrm{O}(x=0)}$ in Equation (40). The quantitative measure Δx of having been left undefined, Equation (41) essentially means that K_O is proportional to $\Re^{0}_\mathrm{O}$ [Fiel16].

A first approach to develop an empirical, atomistic expression to describe the exchange kinetics of gaseous oxygen with oxides was given by DE SOUZA in 2006 [DeSo06], which showed that the exchange rate $\Re^{0}_\mathrm{O}$ obeys:

$$\Re_{\mathrm{O}}^{0} \sim \left([\mathrm{O}_{\mathrm{O}}^{\times}][\mathrm{e}'][\mathrm{h}^{\bullet}]\right)^{\frac{1}{2}} \frac{p_{\mathrm{O}_2}{}^{\frac{1}{4}}}{[\mathrm{V}_{\mathrm{O}}^{\bullet\bullet}]^{\frac{1}{2}}} . \qquad (42)$$

Because electron and hole concentrations typically exhibit opposite dependences on the oxygen partial pressure, they do not contribute a net dependence to the exchange rate. In appendix E.2 it is shown how the equilibrium exchange rate can be defined depending on the actual rate determining step (rds) of the assumed reaction scheme.

In terms of the surface concentration of oxygen vacancies $\mathrm{V}_{\mathrm{O}}^{\bullet\bullet}$ it is often assumed that bulk behavior corresponds to the surface behavior, implying that the surface concentration can be replaced by the bulk concentration experimentally derived, in order to correlate it with the oxygen partial pressure of the gas atmosphere. Here DE SOUZA [DeSo06] noted that the validity of analyzing surface reaction constants in terms of bulk defect thermodynamics is questionable.

Recent experimental findings showed that surface and bulk oxygen non-stoichiometry must be differentiated [Bish09b] and that the dependences of surface and bulk defect concentration on temperature and oxygen partial pressure are different [Chue12b], especially under experimental conditions involving splitting reactions [Zhao16].

Furthermore, if surface defects such as $\mathrm{Ce}_{\mathrm{Ce}}'$ and $\mathrm{V}_{\mathrm{O}}^{\bullet\bullet}$ are indeed the active sites, displaying very high concentrations, site saturation effects can lead to very weak oxygen partial pressure and temperature dependences. This then limits the extent to which such dependences can be used to further distinguish between reaction pathways as proposed and discussed in the respective literature [Chue12a].

In principle it is assumed until to date [Kiln11, Blai15, Anan16] that K_{O} and D_{O} are independent parameters, each of which reflects an independent microscopic mechanism. There is empirical evidence that this is not the case as KILNER et al. [Kiln96b] showed that there is, for a large number of different oxide materials, a quite obvious correlation $K_{\mathrm{O}} \sim D_{\mathrm{O}}^{½}$ between the oxygen surface exchange coefficient and the oxygen diffusion coefficient.

Furthermore, experimental findings by ARMSTRONG et al. [Arms11, Arms13] and KNOBLAUCH et al. [Knob15] suggest that the measured oxygen surface exchange coefficient K_{O}, if measured in the mixed regime or in the diffusion controlled kinetic regime, depends not only on the equilibrium oxygen exchange rate $\Re_{\mathrm{O}}^{0}$ at the gas/solid interface but also on the oxygen diffusion coefficient D_O in the bulk, which contradicts the postulated dependency of K_O on $\Re_\mathrm{O}^0$ in Equation (41) in all kinetic regimes.

As FIELITZ and BORCHARDT [Fiel16] discussed, differences in the reported range of activation enthalpies of the surface exchange can therefore be explained by the differences in the experimental conditions. They were able to extend the approach of MAIER in consistent manner by deriving different expressions for the surface exchange coefficient (confer appendix E.3), depending whether it was determined in the surface exchange regime:

$$K_\mathrm{O}^{h\to 0} = \frac{h}{2} w_\mathrm{O}(x=0) \frac{\Re_\mathrm{O}^0}{c_\mathrm{O}(x=0)} , \tag{43}$$

or in the mixed regime or diffusion controlled regime:

$$K_\mathrm{O}^{h\to\infty} = \left(w_\mathrm{O}(x=0) D_\mathrm{O} \frac{\Re_\mathrm{O}^0}{c_\mathrm{O}(x=0)} \right)^{\frac{1}{2}} , \tag{44}$$

which then allows to rationalise the correlation $K_\mathrm{O} \sim D_\mathrm{O}^{1/2}$, assuming $\Re_\mathrm{O}^0$ to be virtually constant. The expected different temperature dependencies then comprise the range of apparent activation enthalpies reported.

In recent years several experimental and theoretical studies on the actual characteristics of the carbon dioxide reduction on reduced ceria as given in Equation (6) have so far not given a consistent picture. As was shown by BUENO-LÓPEZ et al. [Buen08], the oxygen exchange mechanism between $C^{18}O_2$ and ceria samples in equilibrium consists of the exchange of oxygen atoms in two consecutive steps, yielding $C^{16}O^{18}O$ and $C^{16}O_2$. As the underlying chemistry is poorly understood at the molecular level, at the time of this work no model was proposed for the actual oxygen exchange mechanism between CO_2 and $CeO_{2-\delta}$ in the literature. On the basis of the reaction model in Equations (34) - (38) the reaction steps must involve adsorption and bond breaking of the CO_2 molecules at the respective surface of the reduced ceria.

Early experimental work focused on the interaction of the reduced ceria surface with CO_2-molecules in terms of adsorption and dissociation. APPEL et al. [Appe98] reported carbonate (CO_3^{2-}) formation on ceria powder and pressed ceria pellets at room temperature after exposure to CO_2, which was stable up to T = 400 °C and decreased the reactivity regarding oxygen exchange, but decomposed at T > 400 °C.

BINET et al. [Bine99] reported the formation of carbonate, hydrogen carbonate and carboxylate (CO_2^-) species on ceria bulk samples after exposure to CO_2, with the decomposition at 400 °C $\leq T \leq$ 600 °C.

LYKHACH et al. [Lykh10] reported the formation of carbonate and carboxylate species on CeO_2 (111) thin films at room temperature after exposure to CO_2 and the decomposition of those species at $T >$ 400 °C. STAUDT and co-workers [Stau10] continued experimental work on model systems of CeO_2 (111) thin films and could show that partial re-oxidation of $CeO_{2-\delta}$ by CO_2 occurs with high reaction probabilities even at temperatures as low as room temperature (as it was also discussed in section 2.3 in relation to re-oxidation of reduced ceria by pure oxygen at room temperature), without any noble metal co-catalysts, and in the absence of surface hydroxyl groups or water, pointing out the high activity of reduced pure metal-free ceria surfaces. Their findings also suggest that carboxylates are an intermediate step of re-oxidation [Stau11].

In principle, the in-operando analyzes of the surface offers the possibility to follow the surface characteristics as a function of temperature, oxygen activity and the enrichment/depletion of doping components or impurities during a reaction. Representing this type of experimental methodology, some recent experimental work by the groups CHUEH and EICHHORN [Zhan12, Feng14, Yu14, Feng15] are exemplary. They could show that surface oxygen transfer mediated by oxygen vacancies is fast, that electron transfer is rate determining and that carbonate species (CO_3^{2-}) are formed as reaction intermediates under certain experimental conditions, which are coupled to the surface Ce^{3+} concentration.

Recent theoretical work [Hahn13, Chen13, Kuma16] is applying density functional theory on CO_2 adsorption and dissociation on ceria surfaces. CHENG et al. [Chen13] found that CO_2 adsorption on reduced ceria surfaces is thermodynamically favored over adsorption on stoichiometric ceria and that the oxygen vacancy configuration at the surface plays a crucial role with regards to the reaction pathway. KUMARI et al. [Kuma16] concluded that the activation energies of CO_2 dissociation are energetically favored on oxygen divacancies compared to single vacancies at the surface and that coadsorption of hydrogen assists CO_2 dissociation by forming carboxyl intermediates.

5 Materials and methods

5.1 Sample preparation

CeO_2 and doped $Ce_{0.9}M_{0.1}O_2$ (with M = Y, Sm, Zr) powders were synthesized in the context of the Virtual Institute SolarSynGas by Dr. Nicole Knoblauch (DLR, Institut für Werkstoffforschung), as published [Knob15, Knob17], using the PECHINI method [Pech67], a citric acid assisted combustion method. Therefore, $Ce(NO_3)_3 \cdot 6H_2O$ (Alfa Aesar, 99.99 %) and salts of doping Elements Zr, Sm and Y ($ZrO(Cl)_2 \cdot 8H_2O$, $Sm(NO_3)_3 \cdot 6H_2O$, $Y(NO_3)_3 \cdot 6H_2O$, 99.9 %, Alfa Aesar) were dissolved in demineralized water in the corresponding concentrations and citric acid (VWR chemicals) and ethylene glycol (VWR chemicals) were added in a molar ratio of 1:2:3 (cations:citric acid:ethylene glycol).

The obtained mixture was stirred at $T = 100$ °C for $t = 1$ h. A stepwise increase of the temperature up to $T = 200$ °C resulted in a concentrated solution due to water evaporation. Finally, a viscous yellow gel was formed by polyesterification. This gel was heated to $T = 450$ °C for the pyrolysis of any organic species. The product was calcined in an electrical furnace at $T = 750$ °C in ambient air for $t = 2$ h to remove any remaining carbonaceous species.

The obtained oxide powder was analyzed by X-ray diffractometry (XRD) (D-5000, Siemens) using Ni-filtered Cu-Kα radiation. The CaF_2-type CeO_2 phase was identified. Inductively coupled plasma optical emission spectrometry (ICP-OES) was done to reveal the impurity concentration. While the concentration of lanthanum (about 0.2 at-%) has to be taken into account as trivalent dopant, the other impurities were mutually compensating and in total below about 0.09 at-%.

In order to prepare disc-shaped pellets the powder was milled using a laboratory ball mill (planetary micromill pulverisette 7, Fritzsch, $t = 3 \cdot 10$ min, 500 rpm, mass ratio of 1:10:60 powder:isopropyl alcohol:ZrO_2 balls) and uniaxially cold-pressed at $p = 283$ MPa. After sintering at $T = 1650$ °C for $t = 2$ h the pellets had a relative density of about 95 % and an average grain size of about 20 µm.

The samples were embedded by Sebastian Fischer (TU Clausthal, Institut für Metallurgie) in cold-curing embedding agent (Technovit 5071, Kulzer) and then placed on a polishing machine and counter-rotating (i.e. counter plate runs clockwise and sample holder counterclockwise) on a polishing medium ($F = 30$ N, Allegro, Struers) with 15 µm polycrystalline diamond polishing suspension (Struers) polished. The second step (*t* = 30 min, *F* = 30 N) was polishing with 6 µm polycrystalline diamond suspension on the polishing pad until the eruptions and scratches of the previous stage are removed. The third step involved polishing with polishing wheels (single-stage grinding, *t* = 45 - 60 min, 25 N, Largo, Struers, and STEP-PLUS, Microdiamant) with 6 µm and 3 µm polycrystalline diamond suspension to refine the scratch image. For the final polishing step the samples were processed with a cloth (*t* = 60 min, *F* = 20 N, NAP, Struers) with 1 µm polycrystalline diamond suspension. Then the embedding agent was dissolved in acetone. The samples were cleaned with isopropanol and annealed. In order to prepare the samples for SIMS IELS measurements they were newly embedded (Technovit 5071, Kulzer), cut and dissolved again with acetone. Thereafter, the samples were collapsed, cold-embedded (EPO-FIX, Struers) and prepared as described above.

5.2 Experimental setup for isotope exchange utilizing $^{18}O_2$ and $C^{18}O_2$

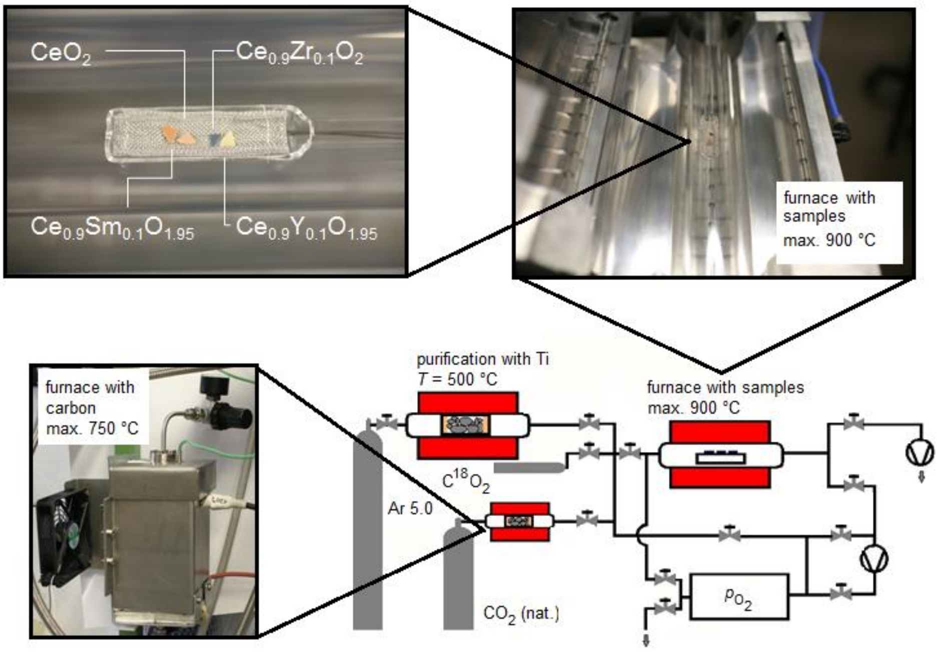

Figure 9. Scheme of the self-constructed experimental setup with an IR radiation heated furnace which allows fast heating rates up to 100 K/s in the temperature range between *T* = 300 °C and *T* = 900 °C. Further can be seen the purification unit where the argon gas flow is reduced by a titanium sponge at *T* = 500 °C, which enables oxygen partial pressures for the reduction step of $p_{O_2} \leq 10^{-24}$ bar. These were measured for all experiments in situ with a lambda probe (further details are given in the text).

The cut, polished and cleaned (ultrasonic cleaning in acetone followed by isopropanol) CeO_2 and $Ce_{0.9}M_{0.1}O_2$ samples were annealed in a self-constructed experimental setup with an IR radiation heated furnace (Quad Elliptical, RI Controls/Research Incorporated), which allows fast heating rates up to 100 K/s in the temperature range 300 °C $\leq T \leq$ 900 °C. As shown in Figure 9 the samples were placed on a platinum mesh (avoiding contact of the platinum with the polished sample surface) in a quartz holder in well-defined atmosphere conditions (vacuum down to 10^{-9} bar, purified argon gas flow with $p_{\mathrm{O}_2} \leq 10^{-24}$ bar, oxygen isotope enriched gas mixture or other gas atmospheres being used).

5.3 Experimental realization of chemical equilibrium and non-equilibrium conditions

The experimental work in oxygen atmosphere in so-called equilibrium conditions started with an equilibration of the samples in 0.2 bar $^{16}O_2$ (natural oxygen gas) for at least 10 times the annealing time of the subsequent isotope exchange ($t_{\mathrm{eq}} = 10 \cdot t_{\mathrm{ex}}$) in $^{18}O_2$ enriched oxygen gas (96 % enrichment) at the same temperature ($T_{\mathrm{eq}} = T_{\mathrm{ex}}$). To avoid a change in oxygen partial pressure during the first experimental step the pre-treatment was conducted in steps with renewing gas, and one of the samples was taken as a reference for measuring the actual oxygen isotope background concentration (about 0.2 %). For the second experimental step, which is the actual oxygen isotope exchange step, the samples were quenched to room temperature, the gas atmosphere was changed from natural oxygen to $^{18}O_2$ (96 % enrichment) and the oxygen isotope exchange was then conducted at t_{ex} and T_{ex}.

The oxygen partial pressure during experiments using a carbon dioxide gas atmosphere was much lower in comparison to established experimental work using pure oxygen. It is determined mainly by the CO:CO_2 ratio of the given gas mixture by the respective temperature T and/or additional oxygen sources. Because of the considerable cost of $C^{18}O_2$ (835 ppm CO, < 250 ppm O_2, Campro Scientific) a gas mixture of purified argon with “labelled” carbon dioxide with an Ar:$C^{18}O_2$ ratio of 10:1 in a closed volume (V = 1 l) was used for the experimental work. As given in Figure 10, the calculated a_{O_2} of the CO_2 containing gas mixture was less than 10^{-15} at T = 700 °C.

The utilization of a carbon dioxide gas atmosphere promoted the challenge of preconditioning the samples to reach real chemical equilibrium. The pre-treatment of the samples was done in a first so-called equilibration step utilizing an Ar/$C^{\mathrm{nat}}O_2$ gas mixture, realizing equivalent oxygen activities as given in the isotope exchange experiment with $C^{18}O_2$ (for example a_{O_2} is about 10^{-15} at T = 700 °C) and plotted in Figure 10. As can be seen, the purchased $C^{\mathrm{nat}}O_2$ and the $C^{18}O_2$ have different content of CO and O_2 impurities, which necessitated to shift the CO:CO_2 ratio in natural carbon dioxide gas through the reduction of CO_2 via a self-constructed furnace with pure carbon (confer Figure 9) at $T = 650$ °C, which is shown in Figure 11. In the general case of measurements with a chemical potential gradient (difference in the chemical potential of oxygen) at the gas/solid interface the experimental work started with a reduction step of the sample utilizing purified argon gas with $p_{O_2} \leq 10^{-24}$ bar, where the respective oxygen non-stoichiometry δ of the sample depends on the temperature of the reduction step and the ceria sample type, as described in section 4.1.

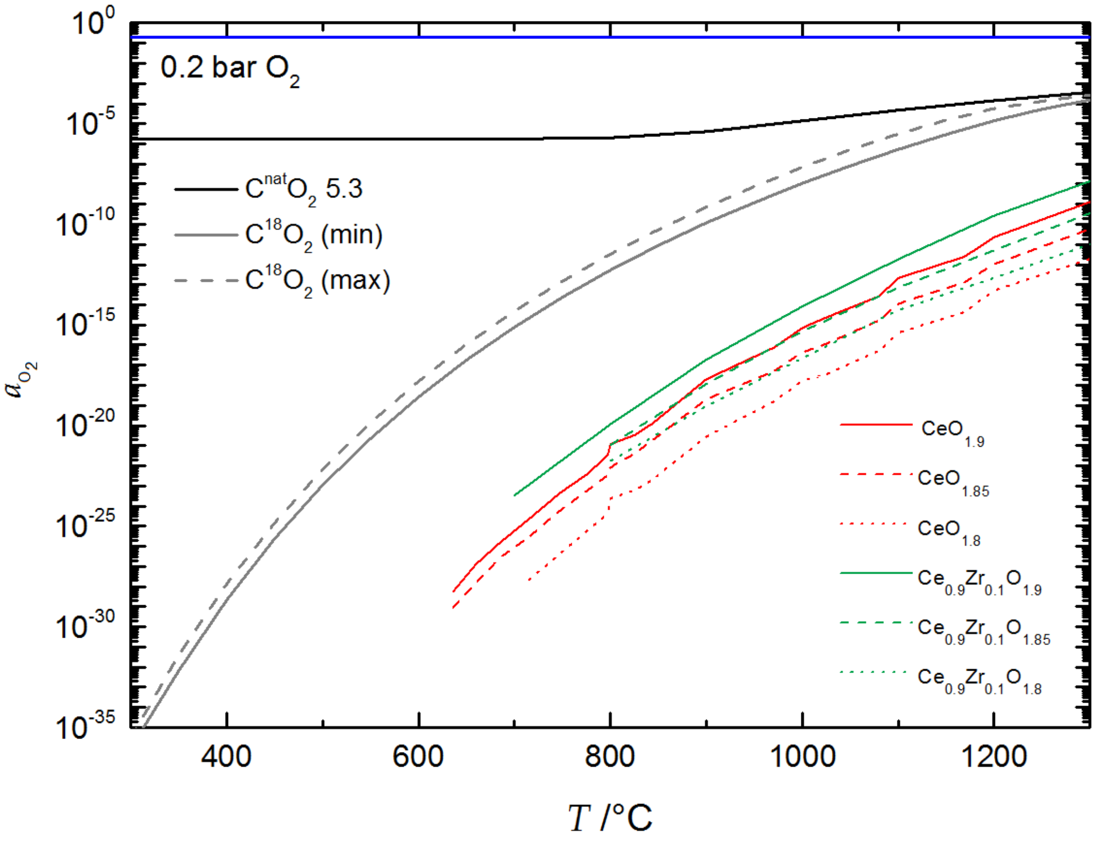

Figure 10. Comparison of oxygen activities of different gas atmospheres and sample types as used in this work. The solid blue line represents ambient oxygen atmosphere. The solid black line represents the calculated oxygen activity of the purchased natural carbon dioxide, $C^{nat}O_2$ 5.3 (Linde), calculated for 1 mol CO_2, $5 \cdot 10^{-7}$ mol CO, $2 \cdot 10^{-6}$ mol O_2. The dotted grey line represents $C^{18}O_2$ (Campro Scientific), calculated for 1 mol CO_2, $8.35 \cdot 10^{-4}$ mol CO, and a maximum value of $2.5 \cdot 10^{-4}$ mol O_2. The solid grey line represents the calculation without any oxygen. The green and red solid and dotted lines are the measured oxygen activities of $CeO_{2-\delta}$ and $Ce_{0.9}Zr_{0.1}O_{2-\delta}$, taken from references [Kuhn13], [Beva64] and [Panl75]. All calculations were done with FactSage Equilib-Web (which can be found via https://www.factsage.com and http://www.crct.polymtl.ca/equiweb.php).

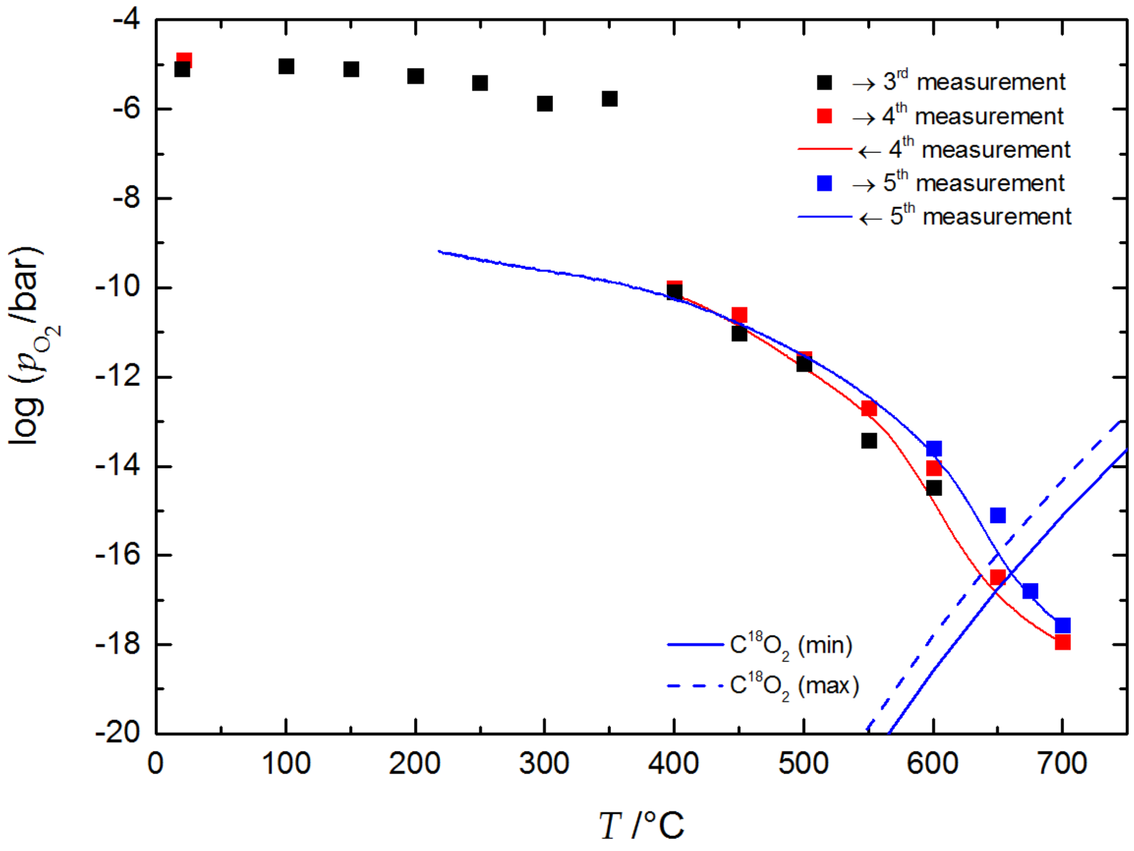

Figure 11. Measured oxygen partial pressure of the purchased natural carbon dioxide, $C^{nat}O_2$ 5.3 (Linde), where the CO:CO_2 ratio is shifted through the reduction of CO_2 via a carbon furnace. The temperature of the carbon furnace is shown at the x axis. Solid points represent measurements from lower to higher temperatures (3rd, 4th and 5th forward measurement), solid lines represent measurements from higher temperatures to lower temperatures (4th and 5th backward measurement). At T = 650 °C the oxygen partial pressure is equal to the oxygen partial pressure of the $C^{18}O_2$ (Campro Scientific) and can therefore be used for the equilibration step of the samples.

Comparable to the low temperature step of the two-step thermochemical cycle for splitting CO_2, the equilibrium oxygen activity of the samples has to be lower than the oxygen activity of the Ar/$C^{18}O_2$ gas mixture (as shown in Figure 10) in which the samples are annealed at a given temperature: $\mu_{O_2}^{sample} < \mu_{O_2}^{gas}$. During the experiment the ^{18}O will be incorporated from $C^{18}O_2$ into the sample bulk (neglecting isotope exchange).

Because of the closed volume (continuous gas flow was not used due to the limited amount of $C^{18}O_2$) the gradient of the chemical potential of oxygen will change during the experiment for two reasons. First, the oxygen activity in the sample will increase, especially at the sample surface and in the near-surface region of the bulk, due to oxygen incorporation. Second, the oxygen uptake of the samples will decrease the oxygen partial pressure in the gas phase.

This is shown in Figure 12 for the reaction of reduced un-doped ceria with an Ar/C$^{18}O_2$ gas mixture at T = 700 °C.

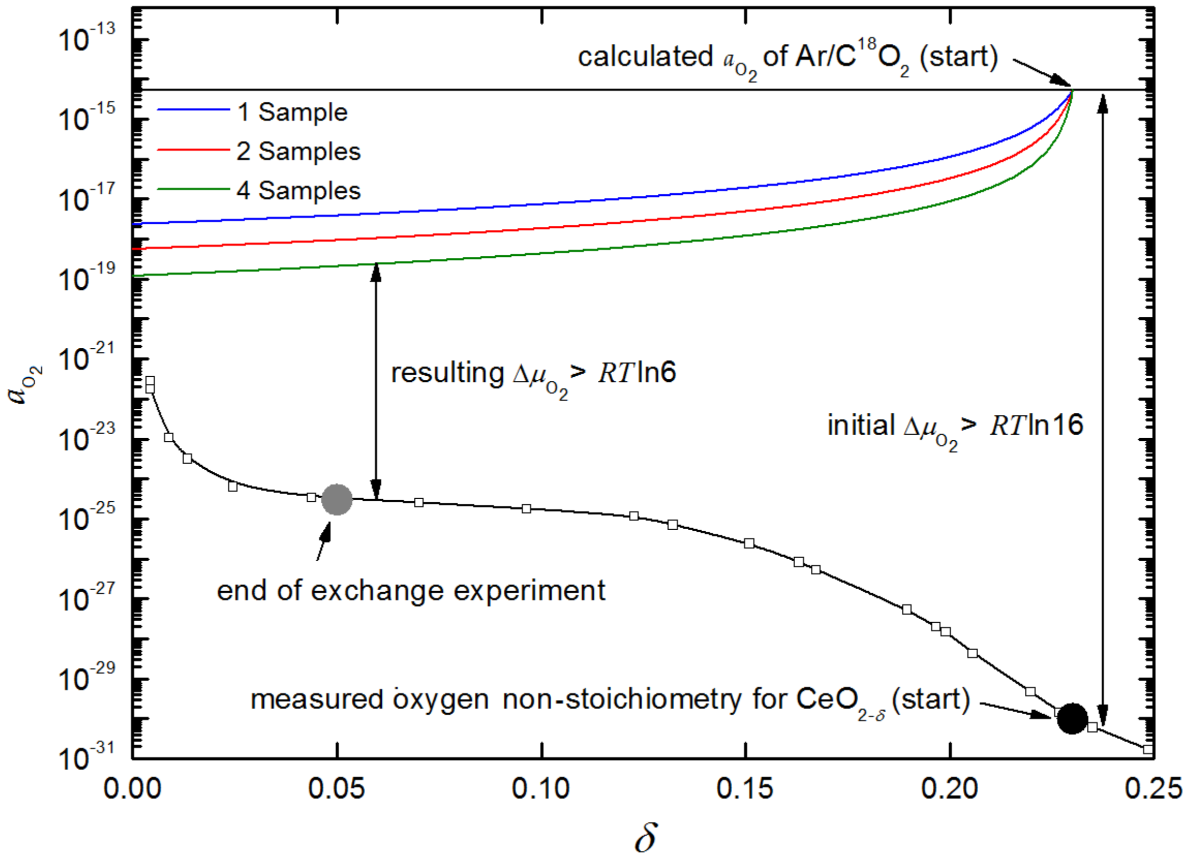

Figure 12. Illustration of the change of the chemical potential of oxygen during an exchange experiment, where the ^{18}O is incorporated from the C$^{18}O_2$ into the sample bulk. The initial oxygen non-stoichiometry depends on the temperature and oxygen partial pressure during the reduction step. Because of the closed volume the gradient of the chemical potential of oxygen will change during the experiment. The oxygen partial pressure of the Ar/C$^{18}O_2$ gas mixture was measured for all experiments in situ with a lambda probe, which enabled to estimate the oxygen activity of the sample at the end of the exchange experiment. The analytical solution given in Equation (B2) requires constant parameters D and K for the boundary conditions given in Equation (E9). It can therefore only be applied if the change in the chemical potential gradient is small and the boundary condition of a constant oxygen concentration at the gas/solid interface is sufficiently fulfilled through carefully choosing the initial oxygen non-stoichiometry of the sample, i.e. the initial non-stoichiometry in the flat range of the $p_{O_2} = f(\delta)$ plot.

All experimental conditions for the reduction step, equilibration step and isotope exchange step with the respective parameters as used in this work are summarized in Table 1.

Table 1. Summary of the experimental parameters related to the different steps of the respective experimental conditions as used in this work.

Step	1	2	3
Type	Reduction step	Equilibration step	Isotope exchange
O_2, equilibrium	-	$^{nat}O_2$ $T = T_{ex}$ $p_{total} = 0.2$ bar $p_{O_2} = 0.2$ bar	$^{18}O_2$ (96 %) $T = T_{ex}$ $p_{total} = 0.2$ bar $p_{O_2} = 0.2$ bar
CO_2, equilibrium	-	Ar/$C^{nat}O_2$ (10:1) $T = T_{ex}$ $p_{total} = 1$ bar $10^{-12} \leq p_{O_2} \leq 10^{-15}$ bar	Ar/$C^{18}O_2$ (10:1) $T = T_{ex}$ $p_{total} = 1$ bar $10^{-12} \leq p_{O_2} \leq 10^{-15}$ bar
O_2, chemical potential gradient at gas/solid interface	Ar $T \geq T_{ex}$ $p_{total} = 1$ bar $10^{-23} \leq p_{O_2} \leq 10^{-25}$ bar	-	$^{18}O_2$ (96 %) $T = T_{ex}$ $p_{total} = 0.2$ bar $p_{O_2} = 0.2$ bar
CO_2, chemical potential gradient at gas/solid interface	Ar $T \geq T_{ex}$ $p_{total} = 1$ bar $10^{-23} \leq p_{O_2} \leq 10^{-25}$ bar	-	Ar/$C^{18}O_2$ (10:1) $T = T_{ex}$ $p_{total} = 1$ bar $p_{O_2} \leq 10^{-12}$ bar

5.4 Applied secondary ion mass spectrometry and analysis

A general description of secondary ion mass spectrometry is given in appendix A, sections A.1 and A.2. A detailed overview about the applied SIMS methods and techniques as used in this work can be found in section A.3 of the appendix. In the context of this work, SIMS measurements were conducted with four different SIMS machines, as will be described in the following section.

SIMS IELS measurements were done a) together with Dr. Michal Schulz (TU Clausthal, Forschungszentrum Energiespeichertechnologien), using a SIMS Workstation (Hiden Analytical Ltd) with positive 10 keV argon ions as primary beam with 100 nA ion current and a spot size of about 50 · 110 µm; the raster-scanned area was 500 · 500 µm^2 in imaging mode; negative secondary ions were used for the analysis of the samples, sample charging was prevented by an electron flood gun; b) by Dr. Stefan Beschnitt (RWTH Aachen, Institut für Physikalische Chemie) using a TOF-SIMS IV (ION-TOF GmbH); after cleaning with a positive cesium ion beam (2 keV, 143 nA) the sample was analyzed with positive gallium ions (25 keV, 1.43 nA, beam size 1 µm), sample charging was prevented by an electron flood gun; c) by Prof. Christos Argirusis (TU Clausthal, Institut für Energieforschung und Physikalische Technologien) and Francois Jomard (Université de Versailles-Saint-Quentin, GEMaC) using a IMS 7f N (CAMECA) with positive 15 keV cesium ion primary beam with 10 - 15 nA ion current and a raster of 50 - 500 µm in imagining mode.

SIMS IEDP measurements were done using a IMS 3f/4f (CAMECA) with negative 15 keV oxygen ions as primary beam with 100 nA ion current. The raster-scanned area was 250 · 250 µm^2 and the area of the analyzed zone was 60 · 60 µm^2. Positive secondary ions were used for the analysis of the samples. Sample charging was prevented by sputtering a thin gold layer (about 20 nm) on top of the sample surface. Depth calibration was done by measuring the SIMS crater depth using a surface profiler (Alpha Step 500, Tencor).

The analysis of the measured SIMS depth profiles (^{18}O fraction depth profiles) was done as explained in appendix B, sections B.1 and B.2. The validation and correction of the measured oxygen isotope fraction distributions was done considering the conditions and requirements described in appendix C.

6 Results and discussion

6.1 Reaction model for CO_2 splitting on reduced $CeO_{2-\delta}$ surfaces

As CO_2 splitting on reduced $CeO_{2-\delta}$ surfaces involves the exchange and incorporation of oxygen it is expedient to consider the oxygen incorporation as fundamental reaction, as explained in section 4.3, and recently discussed by Schaube and co-authors [Scha20]. In accordance with the discussed established ideas on surface exchange from pure oxygen atmospheres the following reaction scheme can be deduced:

$$\mathrm{CO_2(g)+S_{ad}\rightarrow CO_2(ad)}\,, \tag{45}$$

$$\mathrm{CO_2(ad)+e'\rightarrow CO_2'(ad)}\,, \tag{46}$$

$$\mathrm{CO_2'(ad)+e'+S_{ad}\rightarrow CO(ad)+O''(ad)}\,, \tag{47}$$

$$\mathrm{CO(ad)+O''(ad)+V_O^{\bullet\bullet}\rightarrow CO(g)+O_O^x+2S_{ad}}\,. \tag{48}$$

Again, it is also reasonable that steps (47) and (48) have to be in one step since O^{2-}(ad) is not stable at the surface, as discussed in section 4.3. This reaction path represents the most simplified possibility as reaction intermediates like carbonate species (CO_3^{2-}) [Zhan12, Feng14, Yu14, Feng15] are not considered here. With appropriate adjustment of the thermodynamic parameters, i.e . electrochemical support or a kinetic inhibition in step (49), as recently discussed by Wang and co-authors [Wang19], the reaction could lead in principle to the dissociation of CO according to the reaction scheme (49) - (51):

$$\mathrm{CO(ad)+e'+O''(ad)+V_O^{\bullet\bullet}\rightarrow CO'(ad)+O_O^x+S_{ad}}\,. \tag{49}$$

$$\mathrm{CO'(ad)+e'+S_{ad}\rightarrow C(ad)+O''(ad)}\,. \tag{50}$$

$$\mathrm{C(ad)+O''(ad)+V_O^{\bullet\bullet}\rightarrow C(ad)+O_O^{\times}+2S_{ad}}\,. \tag{51}$$

As a consequence of this proposed pathway the most likely rate determining step (rds) again is charge transfer leading to dissociation.

In appendix E.2 it is shown how the equilibrium exchange rate $\Re_O^0$ for CO_2 splitting on a reduced $CeO_{2-\delta}$ surface can be defined depending on the actual rate determining step (rds) of the assumed reaction scheme (45) - (48):

$$\Re_{\mathrm{O}}^{0}=\left(\frac{\overleftarrow{k}_{\mathrm{rds}}\overrightarrow{k}_{\mathrm{rds}}K_{\mathrm{ad}}K_{\mathrm{diss}}}{K_{\mathrm{inc}}}\right)^{\frac{1}{2}}\frac{[\mathrm{CO}_2]\left(\left[\mathrm{O}_{\mathrm{O}}^{\times}\right]\right)^{\frac{1}{2}}}{\left[\mathrm{V}_{\mathrm{O}}^{\bullet\bullet}\right]^{\frac{1}{2}}p_{\mathrm{O}_2}^{\frac{1}{4}}}. \qquad (52)$$

The obvious differences of the p_{O_2} - dependency of $\Re_{\mathrm{O}}^{0}$ considering oxygen exchange from pure oxygen atmospheres and during carbon dioxide reduction (compare Equation (42) or (E8) and (52)) are discussed in section 6.7.

6.2 Oxygen exchange from $^{18}O_2$ atmospheres at 700 °C ≤ T ≤ 900 °C

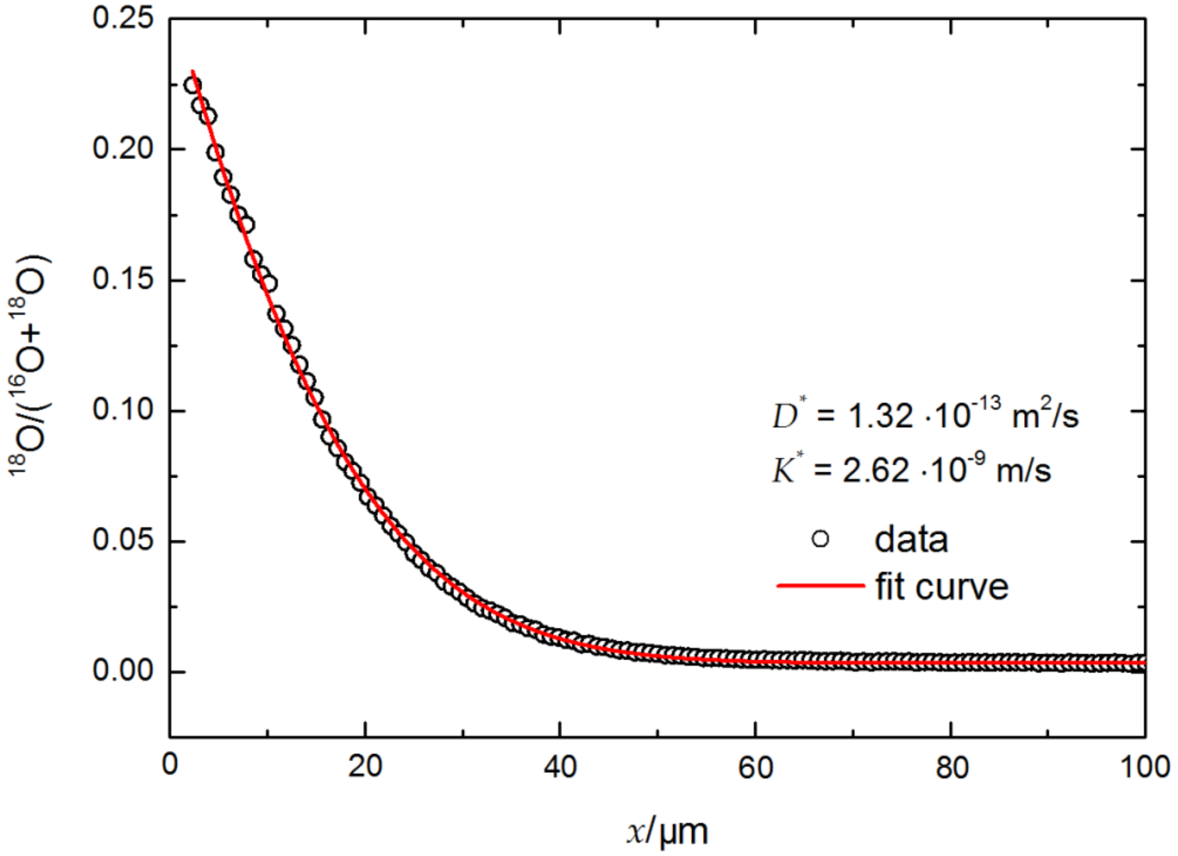

Figure 13. SIMS line scan depth profile for the ^{18}O distribution of a nominally un-doped ceria sample which was pre-annealed for t_{eq} = 5 h in 0.2 bar $^{16}O_2$ at T_{eq} = 900 °C and subsequently annealed for t_{ex} = 1800 s in 0.2 bar $^{18}O_2$ at T_{ex} = 900 °C. The isotope fraction is shown in comparison with the fit by Equation (B2), together with the simultaneously determined tracer values of D_{O} and K_{O}.

Figure 13 shows a typical SIMS depth profile for the ^{18}O distribution of a nominally un-doped ceria sample which was pre-annealed for t_{eq} = 5 h in 0.2 bar $^{16}O_2$ at T_{eq} = 900 °C and subsequently annealed for t_{ex} = 1800 s in 0.2 bar $^{18}O_2$ at T_{ex} = 900 °C.

The corresponding SIMS line scan depth profile is given in Figure A5 and the measurement related issues are discussed in the appendix A in section A.3. The simultaneous determination of the tracer values of D_O and K_O was done by fitting the data with Equation (B2), as discussed in the appendix B in sections B.1 and B.2. The determined oxygen tracer diffusion coefficients and oxygen tracer surface exchange coefficients in ceria containing 10 at-% dopants (Y, Sm, Zr) and of nominally un-doped ceria samples in the temperature range from $700\ °C \leq T \leq 900\ °C$ are shown in Figures 14 and 15, together with calculated activation enthalpies.

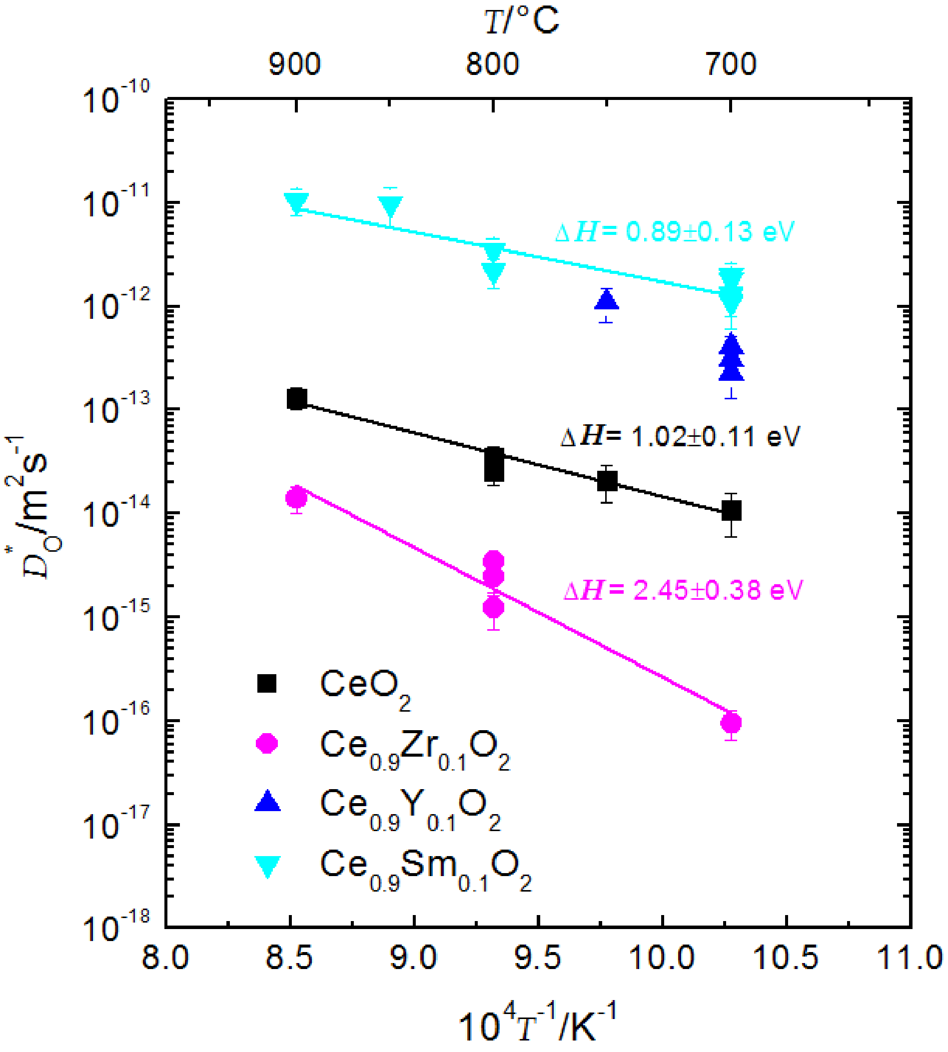

Figure 14. Determined oxygen tracer diffusion coefficients D_O^* in ceria containing 10 at-% of dopants (Y, Sm, Zr) and in nominally un-doped ceria samples in the temperature range from $T = 700$ °C to $T = 900$ °C, together with calculated activation enthalpies.

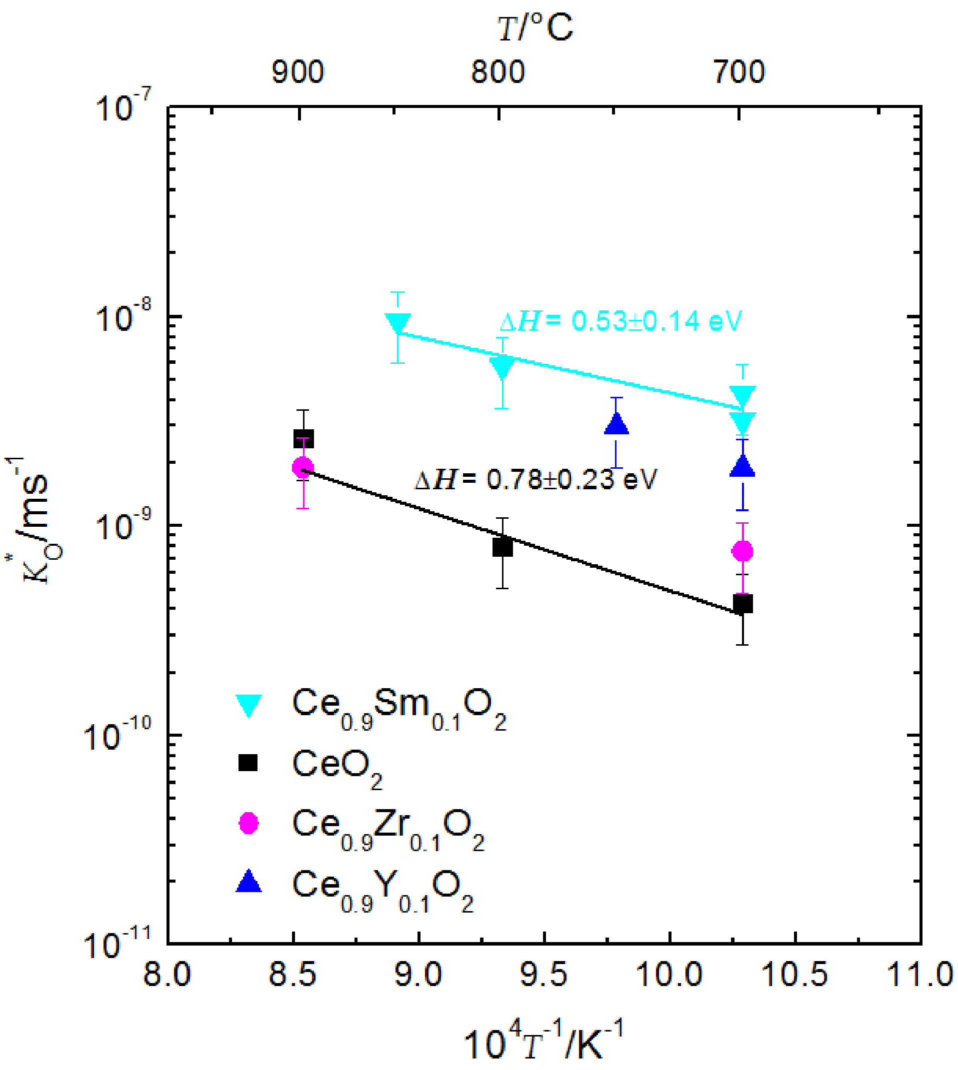

Figure 15. Determined oxygen tracer surface exchange coefficients K^*_O in ceria containing 10 at-% of dopants (Y, Sm, Zr) and in nominally un-doped ceria samples in the temperature range from $T = 700$ °C to $T = 900$ °C, together with calculated activation enthalpies.

In the case that only at two temperatures D^*_O and K^*_O data could be determined, as not all measurements could be validated and/or corrected according to the conditions and requirements described in appendix C, no activation enthalpies were calculated. In Figures 16 and 17 the determined D^*_O and K^*_O data is compared to literature data taken from KAMIYA et al. [Kami00], FLOYD [Floy73] and MANNING et al. [Mann97].

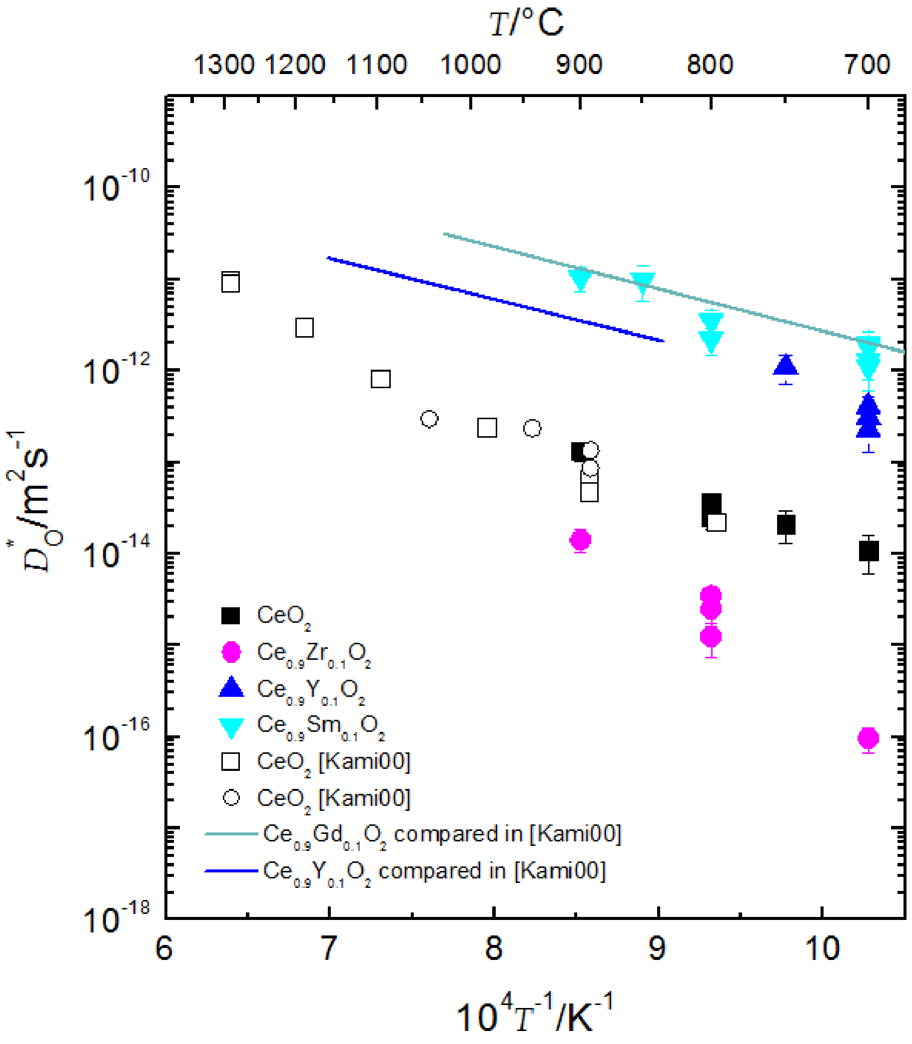

Figure 16. Comparison of the determined D_O^* data of this work to literature data taken from KAMIYA et al. [Kami00] (open symbols), which includes data from FLOYD [Floy73] (blue line) and MANNING et al. [Mann97] (green line).

During the isotope exchange step in non-equilibrium conditions the ^{18}O will be incorporated from the $^{18}O_2$ gas atmosphere into the sample bulk (neglecting isotope exchange), following the discussed reaction pathway in Equations (34) - (38), re-oxidizing the sample. In contrast to the pale-yellow colour of the oxidized ceria samples, the non-stoichiometric form has a blue to black colour, which can be seen in Figure 18. Here, the change in oxygen stoichiometry can be observed at the half-cut sample after re-oxidation.

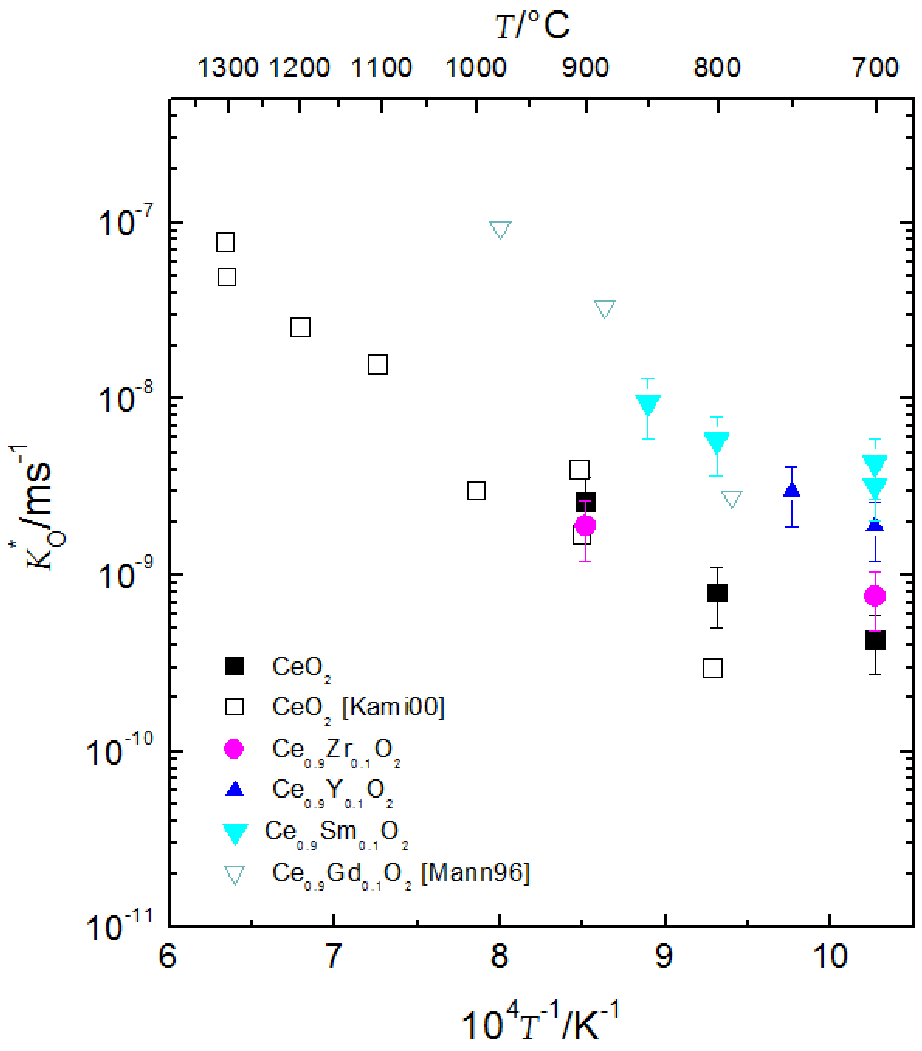

Figure 17. Comparison of the determined K_O^* data of this work to literature data taken from Kamiya et al. [Kami00] (open squares) and Manning et al. [Mann97] (open triangles).

Further it becomes obvious that with the utilization of sintered, disc-shaped pellets, which are relevant to the application in terms of the macroscopic structure of the ceria redox material, certain disadvantages occur. This refers mainly to the inhomogeneity of the sample bulk due to grain boundaries and cracks that occurred occasionally. In the case of the $Ce_{0.9}Zr_{0.1}O_2$ sample, the inhomogeneity were too pronounced to evaluate reliably $\tilde{D}_O$ and $\tilde{K}_O$ data.

The determined chemical (non-equilibrium) oxygen diffusion coefficients and oxygen surface exchange coefficients in ceria containing 10 at-% of dopants (Y, Sm) and in nominally un-doped ceria samples for T = 700 °C are summarized in Table 2.

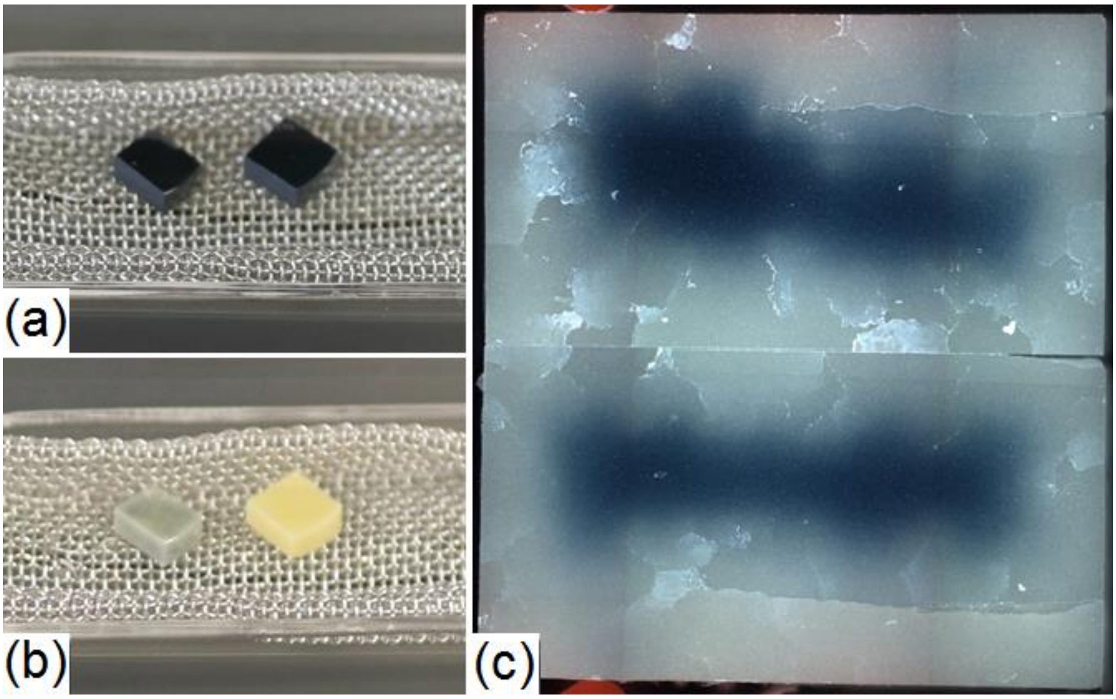

Figure 18. Visible colour change of Zr-doped and Sm-doped ceria samples. In contrast to the pale yellow colour of the oxidized ceria samples in (b), the non-stoichiometric form has a blue to black color (a). The change in oxygen stoichiometry during the isotope exchange experiment can be observed at the half-cut sample ($Ce_{0.9}Zr_{0.1}O_2$) in (c). The samples were reduced at T = 800 °C with $p_{O_2} = 10^{-24}$ bar for t_{red} = 16.5 h and re-oxidized at T = 700 °C with p_{O_2} = 0.2 bar for t_{ox} = 3.2 h in $^{18}O_2$ (96 %).

Table 2. Determined chemical oxygen diffusion coefficients $\tilde{D}_O$ and oxygen surface exchange coefficients $\tilde{K}_O$ in ceria containing 10 at-% of dopants (Y, Sm) and in nominally un-doped ceria samples for oxygen isotope exchange from $^{18}O_2$ (96 %) at T = 700 °C.

Sample type	$\tilde{D}_O$ /m^2·s^{-1}	$\tilde{K}_O$ /m·s^{-1}
CeO_2	$(9.2 \pm 0.2) \cdot 10^{-13}$	$(1.5 \pm 0.56) \cdot 10^{-9}$
$Ce_{0.9}Sm_{0.1}O_{1.95}$	$(1.2 \pm 0.26) \cdot 10^{-12}$	$(1.7 \pm 0.63) \cdot 10^{-9}$
$Ce_{0.9}Y_{0.1}O_{1.95}$	$(1.5 \pm 0.33) \cdot 10^{-12}$	$(2.4 \pm 0.88) \cdot 10^{-9}$

6.3 Oxygen exchange from $C^{18}O_2$ atmospheres at 300 °C ≤ T ≤ 800 °C

As discussed in section 5.3, the oxygen partial pressure during experiments using a carbon dioxide gas atmosphere is much lower in comparison to pure oxygen. The utilization of a carbon dioxide atmosphere promotes the challenge to reach equilibrium conditions. The pre-treatment of the samples was done in a first equilibration step utilizing an Ar/$C^{nat}O_2$ gas mixture, realizing equivalent oxygen activities as given in the isotope exchange experiment with $C^{18}O_2$ (i.e. a_{O_2} is about 10^{-15} at T = 700 °C).

During the annealing step, ^{18}O will be incorporated from $C^{18}O_2$ into the sample bulk, with the exchange of ^{16}O from the sample to the $C^{18}O$(ad), being the backward reaction of the reaction pathway in Equations (45) - (48). As was shown by BUENO-LÓPEZ et al. [Buen08], the oxygen exchange mechanism between $C^{18}O_2$ and ceria samples in chemical equilibrium consists of the exchange of oxygen atoms in two consecutive steps, yielding $C^{16}O^{18}O$ and $C^{16}O_2$.

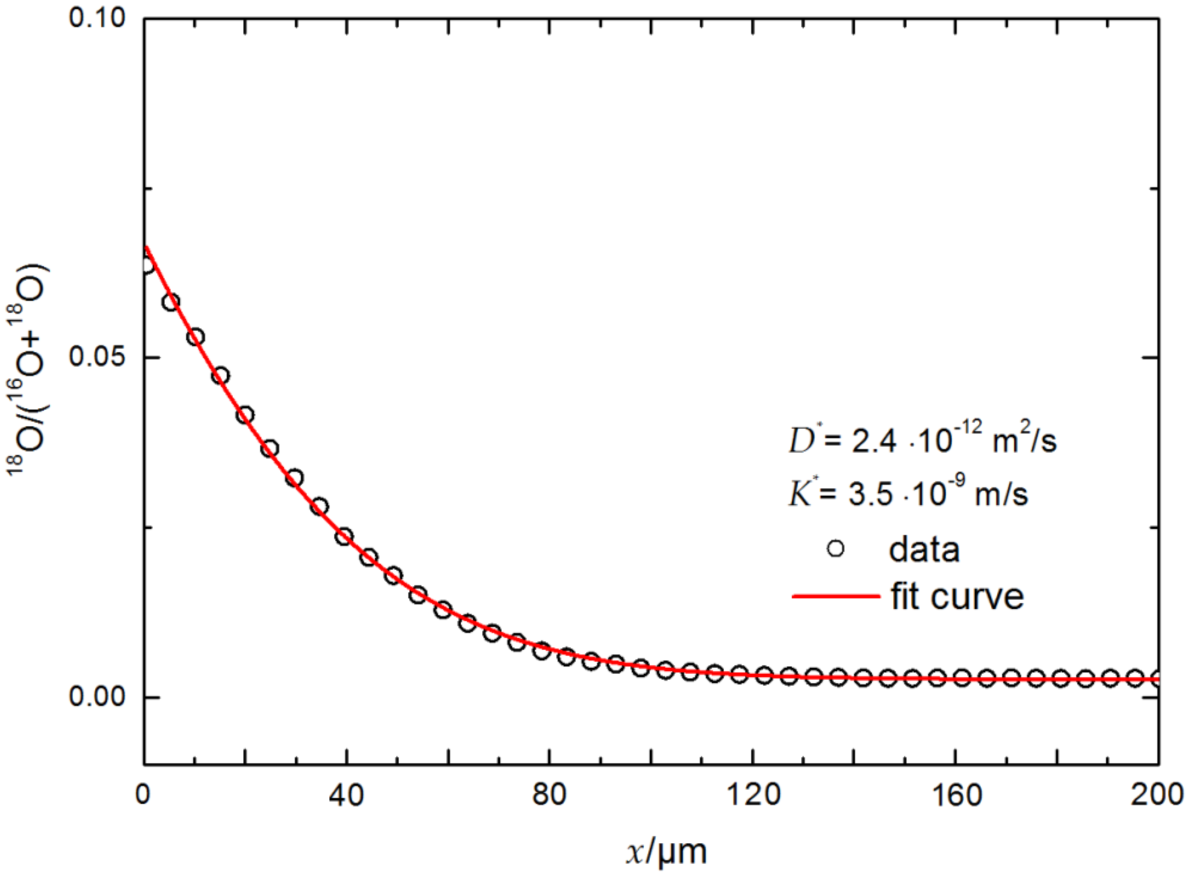

Figure 19. SIMS line scan depth profile for the ^{18}O distribution of a 10 at-% Y-doped ceria sample after an oxygen isotope exchange from $C^{18}O_2$ (Ar/$C^{18}O_2$ gas mixture) in equilibrium conditions at T_{ex} = 700 °C. The oxygen isotope fraction is shown in comparison with the fit by Equation (B2), together with the simultaneous determined equilibrium values of D_O and K_O.

Figure 19 shows a typical SIMS line scan profile for the ^{18}O distribution of a 10 % yttria doped ceria sample after an oxygen isotope exchange from $C^{18}O_2$ (Ar/$C^{18}O_2$ gas mixture) in equilibrium conditions at $T = 700$ °C. The corresponding SIMS ion image is given in Figure A4. The oxygen isotope fraction profiles of Figures 13 and 19 are in principle comparable and show no significant differences between the isotope sources ^{18}O and $C^{18}O_2$. The determined oxygen tracer diffusion coefficients and oxygen tracer surface exchange coefficients in ceria containing 10 at-% of dopants (Y, Sm, Zr) and in nominally un-doped ceria samples for $T = 700$ °C and $T = 800$ °C are summarized in Table 3 and Table 4.

Table 3. Determined oxygen tracer diffusion coefficients D_O^* and oxygen tracer surface exchange coefficients K_O^* in ceria containing 10 at-% of dopants (Y, Sm, Zr) and in nominally un-doped ceria samples for oxygen isotope exchange from in $C^{18}O_2$ (Ar/$C^{18}O_2$ gas mixture) at $T = 700$ °C.

Sample type	D_O^* /m^2·s^{-1}	K_O^* /m·s^{-1}
$Ce_{0.9}Zr_{0.1}O_2$	$(2.7 \pm 0.59) \cdot 10^{-15}$	$(2.6 \pm 0.96) \cdot 10^{-10}$
CeO_2	$(2.4 \pm 0.53) \cdot 10^{-13}$	$(2.4 \pm 0.89) \cdot 10^{-9}$
$Ce_{0.9}Sm_{0.1}O_{1.95}$	$(2.7 \pm 0.59) \cdot 10^{-12}$	$(4.0 \pm 0.15) \cdot 10^{-9}$
$Ce_{0.9}Y_{0.1}O_{1.95}$	$(2.4 \pm 0.53) \cdot 10^{-12}$	$(3.5 \pm 0.13) \cdot 10^{-9}$

Table 4. Determined oxygen tracer diffusion coefficients D_O^* and oxygen tracer surface exchange coefficients K_O^* in ceria containing 10 at-% of dopants (Y, Sm, Zr) and in nominally un-doped ceria samples for oxygen isotope exchange from in $C^{18}O_2$ (Ar/$C^{18}O_2$ gas mixture) at $T = 800$ °C.

Sample type	D_O^* /m^2·s^{-1}	K_O^* /m·s^{-1}
$Ce_{0.9}Zr_{0.1}O_2$	$(8.4 \pm 0.18) \cdot 10^{-14}$	$(1.6 \pm 0.59) \cdot 10^{-8}$
CeO_2	$(4.0 \pm 0.88) \cdot 10^{-13}$	$(1.9 \pm 0.7) \cdot 10^{-8}$
$Ce_{0.9}Y_{0.1}O_{1.95}$	$(2.2 \pm 0.48) \cdot 10^{-13}$	$(3.5 \pm 1.3) \cdot 10^{-7}$
$Ce_{0.9}Sm_{0.1}O_{1.95}$	$(8.0 \pm 1.8) \cdot 10^{-12}$	$(2.6 \pm 0.96) \cdot 10^{-7}$

In the case of oxygen isotope exchange experiments utilizing $C^{18}O_2$ and a chemical potential gradient at the gas/solid interface (non-equilibrium conditions), the experimental work starts, as discussed, with a reduction step with purified argon gas ($10^{-23} < p_{O_2} < 10^{-24}$ bar), where the respective oxygen non-stoichiometry δ of the sample depends on the temperature and the sample type, as described in section 4.1. Comparable to the low temperature step of the two-step thermochemical cycle for splitting CO_2, the equilibrium oxygen activity of the samples has to be lower than the oxygen activity of the Ar/$C^{18}O_2$ gas mixture (as shown in Figures 10 and 12) in which the samples are annealed at a given temperature: $\mu_{O_2}^{\mathrm{sample}} < \mu_{O_2}^{\mathrm{gas}}$. During the experiment the ^{18}O will be incorporated from $C^{18}O_2$ into the sample bulk (neglecting isotope exchange), probably following the proposed reaction pathway in Equations (45) - (48).

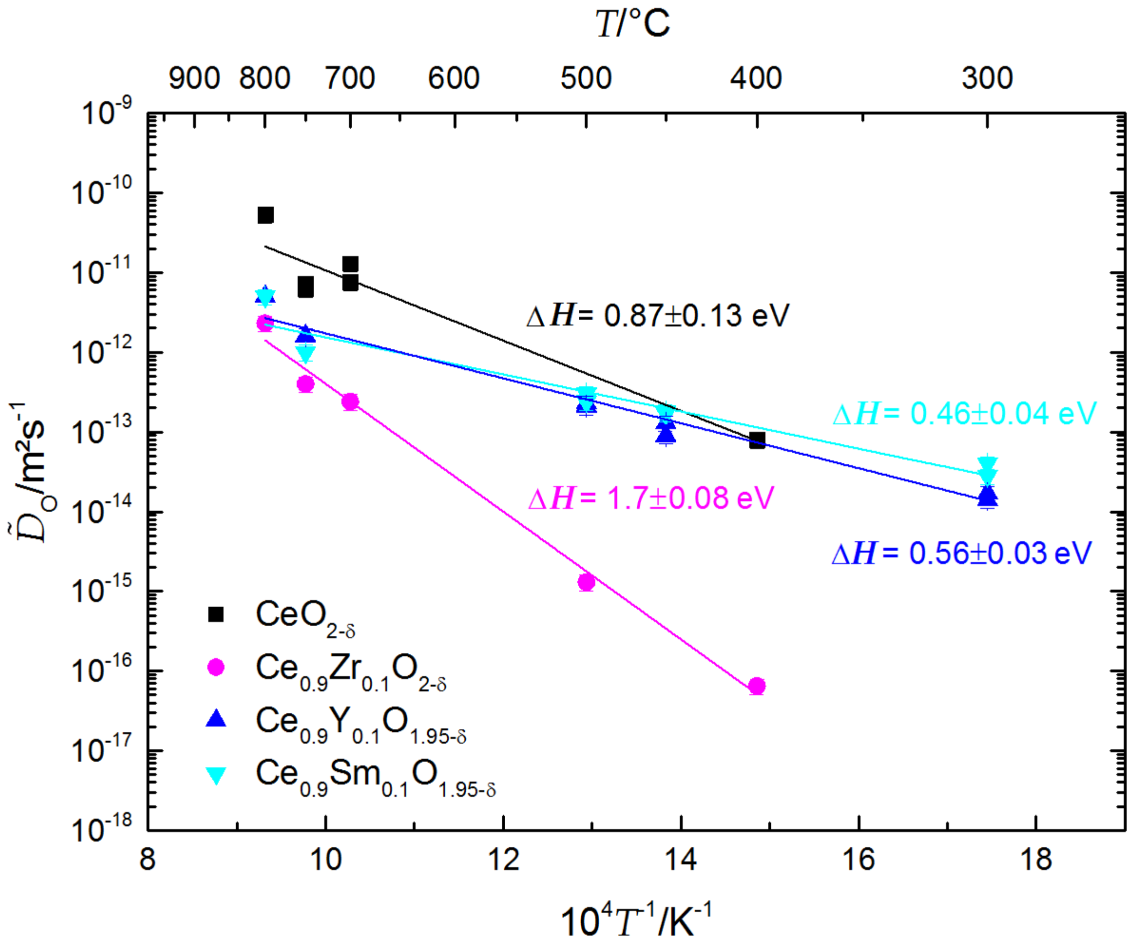

Figure 20. Determined chemical oxygen diffusion coefficients $\tilde{D}_O$ in ceria containing 10 at-% of dopants (Y, Sm, Zr) and in nominally un-doped ceria samples in the temperature range from T = 300 °C to T = 800 °C, together with calculated activation enthalpies.

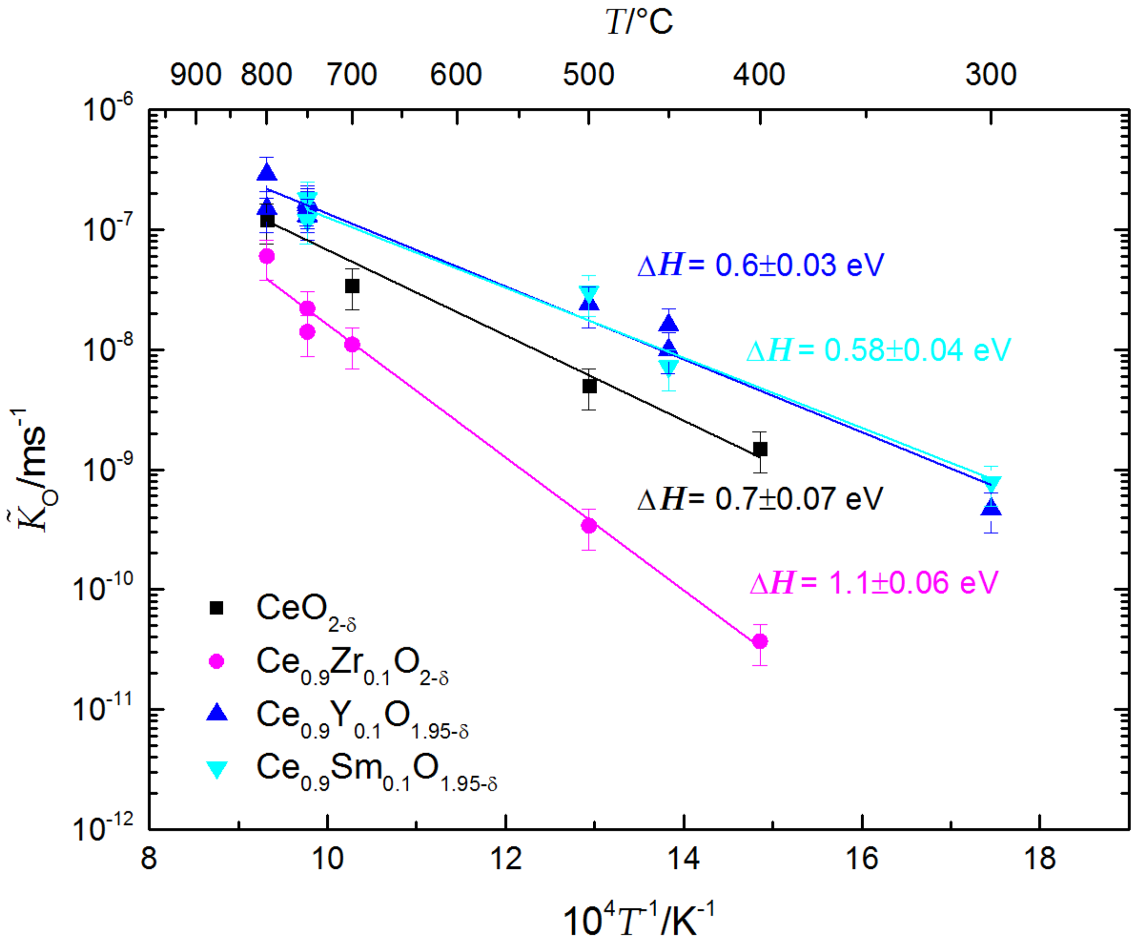

Figure 21. Determined chemical oxygen exchange coefficients $\tilde{K}_\mathrm{O}$ in ceria containing 10 at-% of dopants (Y, Sm, Zr) and in nominally un-doped ceria samples in the temperature range from T = 300 °C to T = 800 °C, together with calculated activation enthalpies.

The determined chemical oxygen diffusion coefficients $\tilde{D}_\mathrm{O}$ and oxygen surface exchange coefficients $\tilde{K}_\mathrm{O}$ in ceria containing 10 at-% of dopants (Y, Sm, Zr) and in nominally un-doped ceria samples in the temperature range from 300 °C $\leq T \leq$ 800 °C are shown in Figures 20 and 21, together with calculated activation enthalpies.

6.4 Oxygen exchange from $^{18}O_2$ atmospheres at room temperature

Re-oxidation phenomena of reduced ceria samples of various constitutions through interaction with O_2 and CO_2 at room temperature are discussed in the respective literature [Ban72, Laac91, Perr94, Nama03, Stau10]. Major issues such as the propagated transport of oxygen in the solid at room temperature as well as the degree of re-oxidation of the bulk remain unclear.

In order to determine the range of the room temperature re-oxidation phenomenon (surface vs. bulk related) as well as the influence of the different dopants on the postulated oxygen diffusion, non-equilibrium oxygen exchange experiments utilizing $^{18}O_2$ as described in section 6.2 were done in the context of this work. Within the initial reduction step two different non-stoichiometries were realized for all sample types, and the reduced samples were held in $^{18}O_2$ at T = 20 °C and t_{ex} = 37 h or rather 43 h. In Figure 22 it is shown how the maximum $^{18}O/O$ relation, which is linked to the oxygen vacancy concentration, can be estimated as a function of ceria non-stoichiometry according to Equation (B4).

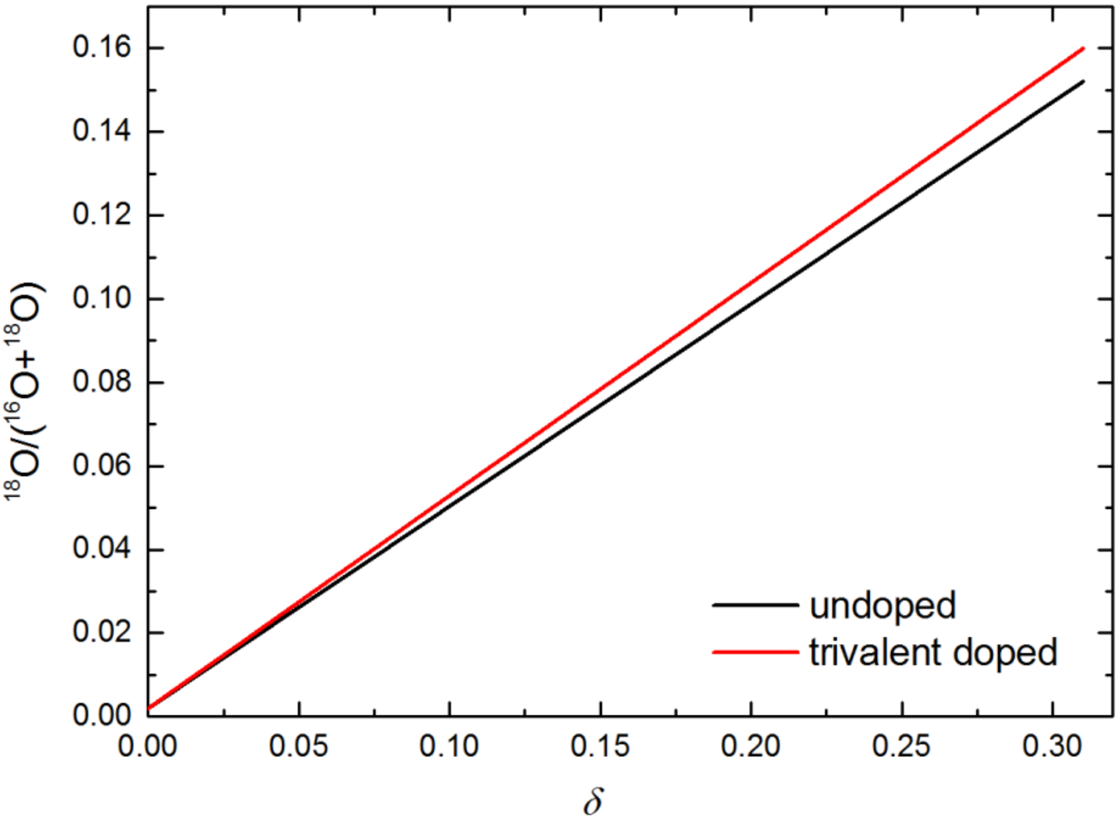

Figure 22. Calculated maximum $^{18}O/O$ relation, which is linked to the oxygen vacancy concentration, and can be estimated as a function of ceria non-stoichiometry δ according to Equation (B4), for undoped and trivalent doped ceria.

In Figures 23 and 24 the oxygen isotope fraction profiles determined via SIMS depth profiling are displayed for the initial non-stoichiometries of $\delta = 0.05$ and $\delta = 0.15$ for all samples. As can be seen, oxygen isotope exchange on doped and nominally undoped ceria can be observed at room temperature and results suggest a dependence of the amount of incorporated oxygen on the initial non-stoichiometry δ, and hence on the concentration of oxygen vacancies, which is in good agreement with the findings of PERRICHON et al. [Perr94] and STAUDT et al.

[Stau10]. As Fischer and Hertz [Fisc12] give a lower limit for the measurable concentration of ^{18}O via SIMS methods of twice the background concentration c_{bg} (= 0.4 %) the measured isotope fraction profiles are considered statistically significant.

Although differences considering the degree of re-oxidation are evident, results suggest that the re-oxidation is related only to the sample surface and near-surface bulk region and that bulk transport is fairly limited at $T \approx 20$ °C. These results are coherent with the surface related re-oxidation phenomena of CeO_2 [Laa1991, Per1994, Nam2003, Sta2010] as well as of ZrO_2 and MoO_3 [Stil21] at room temperature, but cannot confirm the bulk re-oxidation of ceria samples at $20 \leq T \leq 42$ °C based on a so-called rapid mass transport reported by Ban and Nowick [Ban1972].

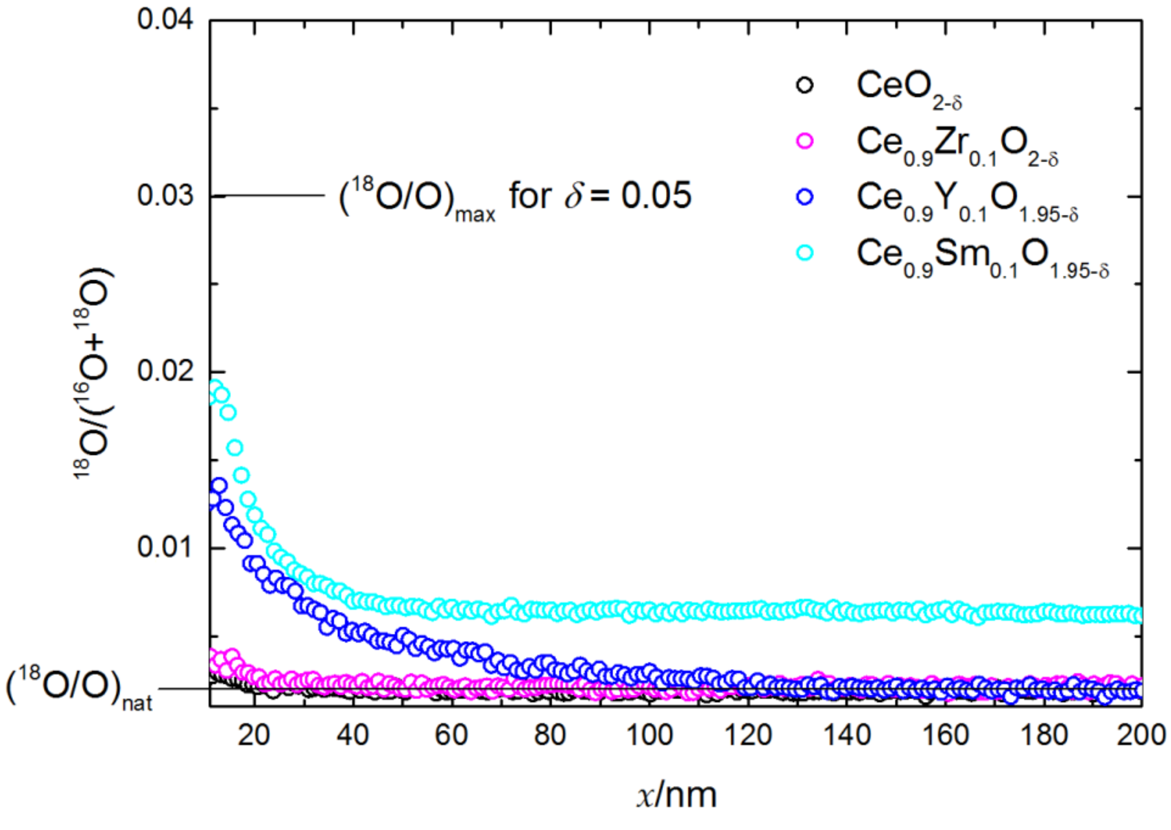

Figure 23. Oxygen isotope fraction profiles in ceria containing 10 at-% of dopants (Y, Sm, Zr) and in nominally un-doped ceria samples determined via SIMS depth profiling for the initial non-stoichiometry of $\delta = 0.05$. The reduced samples were held in $^{18}O_2$ (96 %) at $T = 20$ °C and $t_{ex} = 37$ h. The reason for the enhanced background concentration of ^{18}O in the Sm-doped ceria sample could not be conclusively clarified, but might be related to observed sample cracking.

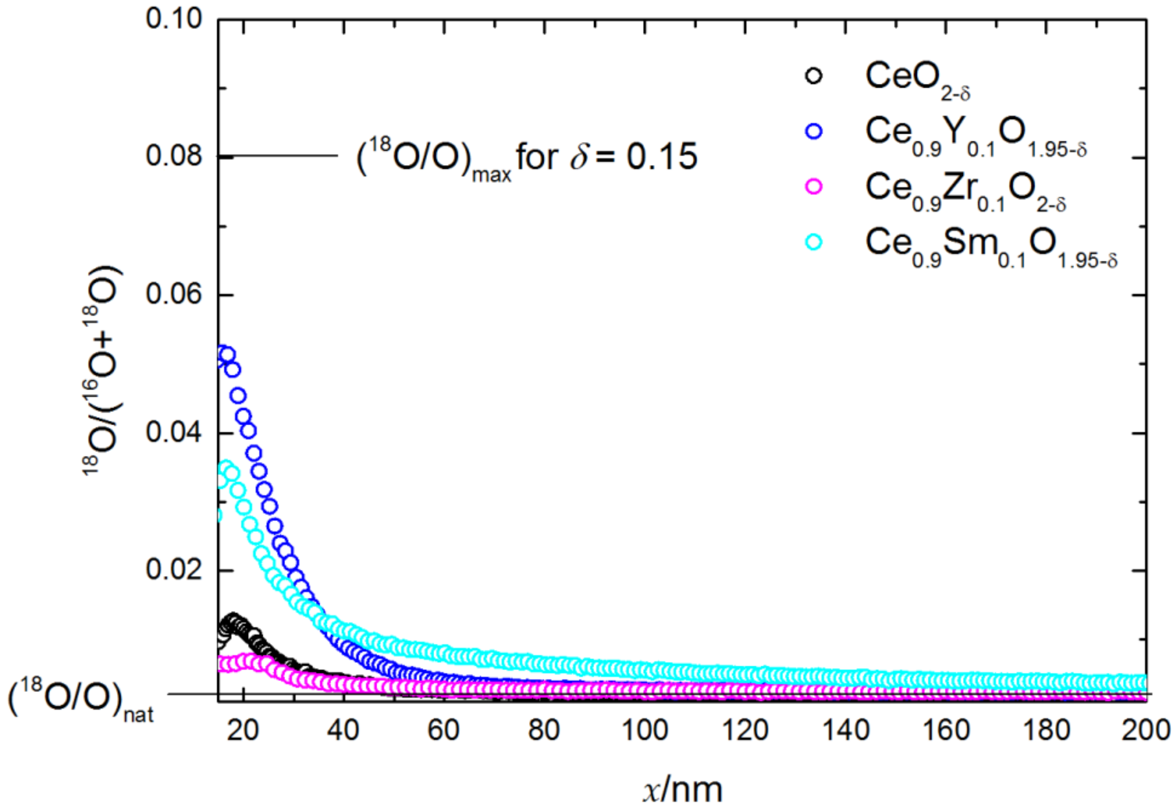

Figure 24. Oxygen isotope fraction profiles in ceria containing 10 at-% of dopants (Y, Sm, Zr) and in nominally un-doped ceria samples determined via SIMS depth profiling for the initial non-stoichiometry of $\delta = 0.15$. The reduced samples were held in $^{18}O_2$ (96 %) at $T = 20$ °C and $t_{ex} = 43$ h.

Table 5. Determined chemical oxygen diffusion coefficients $\tilde{D}_O$ in ceria containing 10 at-% dopants (Y, Sm, Zr) and of nominally un-doped ceria samples for oxygen isotope exchange at $T \approx 20$ °C with an initial non-stoichiometry of $\delta = 0.15$.

Sample type	$\tilde{D}_O$ /$m^2 \cdot s^{-1}$
$Ce_{0.9}Zr_{0.1}O_2$	$(8.5 \pm 1.9) \cdot 10^{-22}$
$Ce_{0.9}Y_{0.1}O_{1.95}$	$(8.2 \pm 1.8) \cdot 10^{-22}$
CeO_2	$(5.9 \pm 1.3) \cdot 10^{-22}$
$Ce_{0.9}Sm_{0.1}O_{1.95}$	$(2.0 \pm 0.44) \cdot 10^{-21}$

The oxygen isotope fraction profiles shown in Figure 24 were utilized to approximate the chemical oxygen diffusion coefficients $\tilde{D}_O$ at room temperature for the initial non-stoichiometry of $\delta = 0.15$ by fitting the measured curves with Equation (C9), which is valid for long annealing times and refers to the diffusivity only, as discussed in section C.2 in the appendix. The calculated non-equilibrium diffusivities are given for all samples in Table 5. Regarding the differences between the ceria sample types in terms of oxygen surface exchange and bulk transport at room temperature the following further conclusions are possible. The near-surface re-oxidation of 10 at.-% Sm-doped and Y-doped ceria is much more pronounced than for the Zr-doped and nominally undoped ceria for both δ values. It is probably due to different rates of oxygen surface exchange, which is indicated by the $\tilde{K}_{\mathrm{O}}$ data at high temperatures.

The calculated chemical oxygen diffusivities at room temperature show no significant differences for Zr-doped, Y-doped and nominally undoped ceria, but differ for 10 at.-% Sm-doped ceria by about one order of magnitude. This is indicated by the $\tilde{D}_{\mathrm{O}}$ data derived at higher temperatures and the calculated low activation enthalpy of (0.46 ± 0.04) eV of 10 at.-% Sm-doped ceria, which is further discussed in section 6.8.

6.5 Estimation of the kinetic regime by $K_{\mathrm{O}}/D_{\mathrm{O}}$ data

As discussed in the previous sections, redox kinetics of ceria is either controlled by surface exchange reactions or by bulk transport of oxygen. In the mixed regime the observed kinetics of the reduction/oxidation process is influenced by contributions of both parameters K and D. A deeper insight into mechanisms and kinetics of ceria reduction and re-oxidation with respect to the derived K^{*}/D^{*} and $\tilde{K}/\tilde{D}$ data is given by calculating the characteristic dimensionless parameter of the kinetic regimes L as discussed in the appendix E.3, with $L = \frac{h}{2}\frac{K}{D}$ and h = 1 mm (sample thickness).

In Figures 25 and 26 the derived K^{*}/D^{*} and $\tilde{K}/\tilde{D}$ data sets from sections 6.2 and 6.3 are given for the respective temperature range, together with the calculated regime boundaries. As can be seen for both data sets, oxygen tracer isotope exchange and non-equilibrium oxygen isotope exchange are either diffusion controlled or in the mixed kinetic regime in the temperature range $T \leq 900$ °C, depending also on the respective sample type. A partial temperature dependency of the K/D ratios is indicated in the given temperature range. In general the results show that the K^{*}/D^{*} ratios, in the case of trivalent-doped ceria samples, and the $\tilde{K}/\tilde{D}$ ratios overall, shift from the mixed regime and tend to reach the surface exchange controlled regime at high temperatures $T \geq 700$ °C.

These finding coincides with the results published by KNOBLAUCH et al. [Knob15], who discussed a surface controlled kinetic regime at higher temperatures $T \geq 1300$ °C for nominally undoped ceria (polycrystalline CeO_2 of 1 mm thickness) that was investigated using thermogravimetric analysis in non-equilibrium conditions. In addition to that MANNING et al. [Mann97] reported a surface controlled kinetic regime for Gd doped ceria in the temperature range $T \leq 1100$ °C (D^* and K^* data). This is attributed to the fact that the trivalent dopant increases the concentration of oxygen vacancies, and hence the diffusivity of oxygen, shifting the K^*/D^* ratio in comparison to the nominally undoped ceria samples.

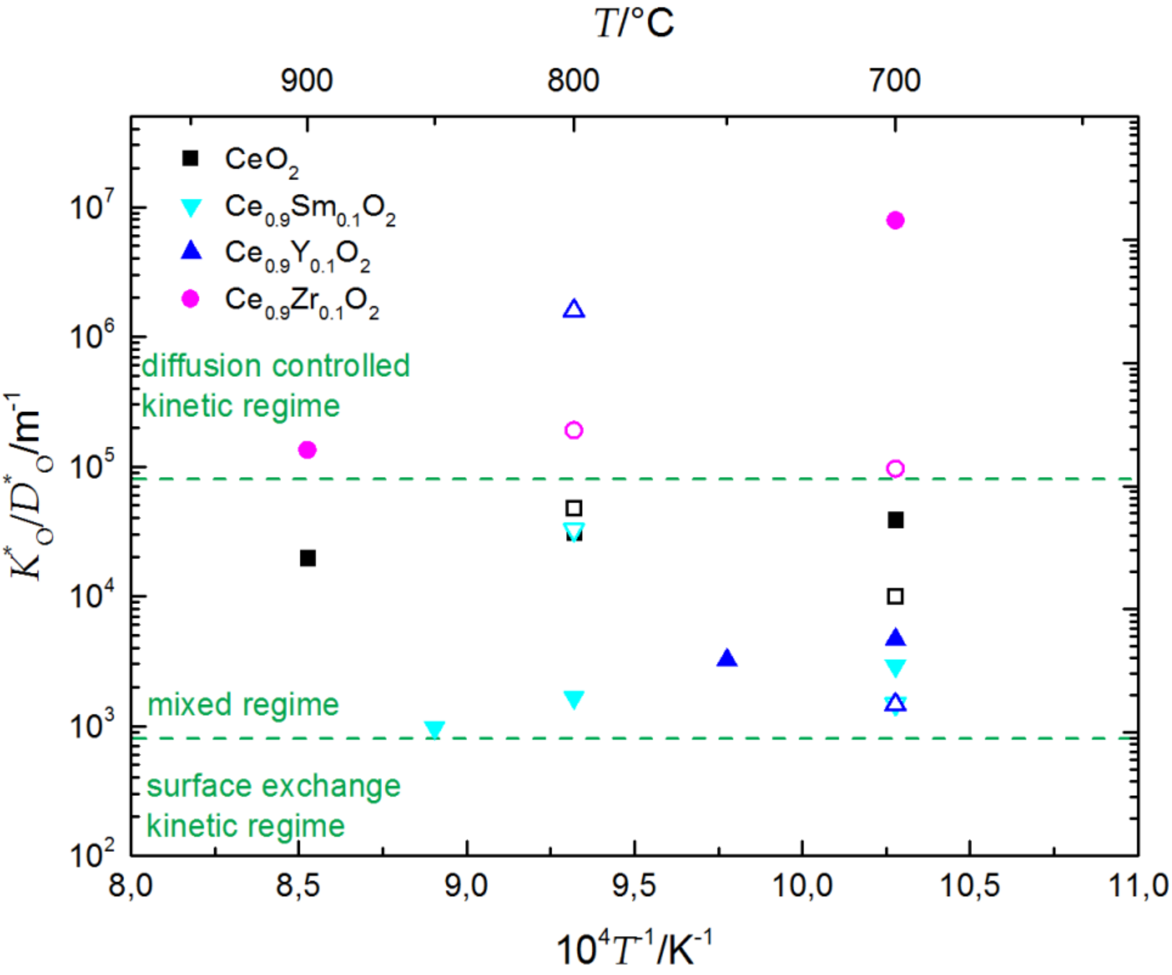

Figure 25. Calculated K^*/D^* ratios for equilibrium oxygen isotope exchange from $^{18}O_2$ (solid data points) and $C^{18}O_2$ (open data points) together with the calculated regime boundaries in the temperature range from $T = 700$ °C to $T = 900$ °C for ceria containing 10 at-% of dopants (Y, Sm, Zr) and in nominally un-doped ceria samples.

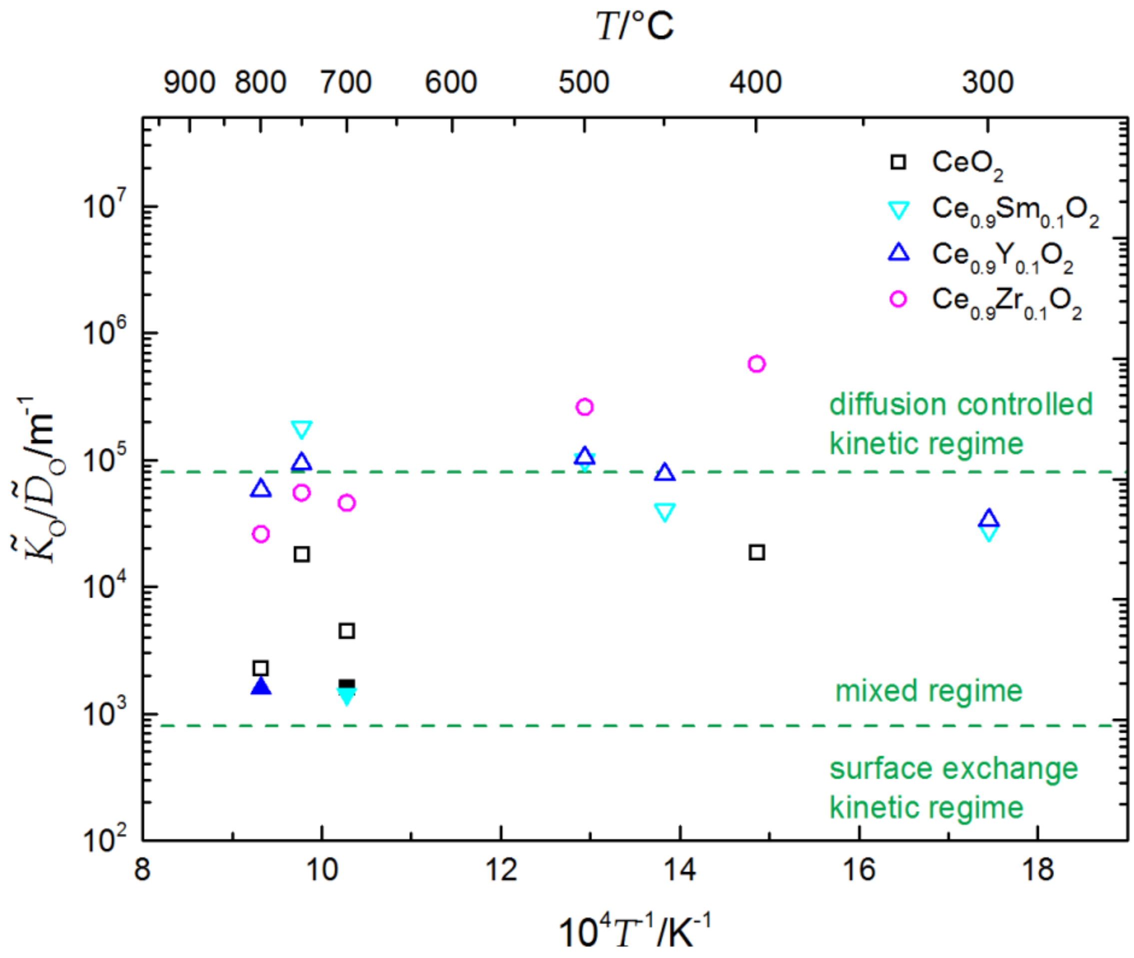

Figure 26. Calculated $\tilde{K}/\tilde{D}$ ratios for non-equilibrium oxygen isotope exchange from $^{18}O_2$ (solid data points) and $C^{18}O_2$ (open data points) together with the calculated regime boundaries in the temperature range from $T = 300$ °C to $T = 800$ °C for ceria containing 10 at-% of dopants (Y, Sm, Zr) and in nominally un-doped ceria samples.

In section 6.7 the oxygen exchange kinetics and their dependency on the given experimental conditions (gas atmosphere, sample type, temperature) is further discussed. The temperature dependency of the *K*/*D* ratios and therefore the observed kinetic regime has impact on the determination of the activation energy of the surface exchange coefficient [Knob15, Fiel16], as it is discussed in section 6.8.

6.6 Calculation of the effective equilibrium exchange rates of oxygen $\Re_O^0$

For a comprehensive understanding of the mechanisms and kinetics of ceria reduction and re-oxidation the normalized exchange rate $\Re_O^0$ (being a measure of the dynamics at equilibrium and quantifying defect chemical reactions at the interface) of the rate determining step in the reaction sequence as described in section 4.3 is calculated utilizing the K^*/D^* and $\tilde{K}/\tilde{D}$ data sets and Equation (44) in the case of mixed or diffusion controlled kinetic regimes.

In Figures 27 and 28 the derived data for oxygen isotope exchange from $^{18}O_2$ and $C^{18}O_2$ with $\Re_O^0 / c_O(x=0) = \left(K_O^*\right)^2 / D_O^*$ and $\Re_O^0 w_O(x=0) / c_O(x=0) = \left(\tilde{K}_O\right)^2 / \tilde{D}_O$ is given for the respective temperature range. They differ by the thermodynamic factor w_O which is equal to unity in terms of equilibrium conditions and further discussed in section 6.7. The normalized exchange rate constant is further identical with the reciprocal characteristic time constant τ^{-1} to reach (isotope) equilibrium at the surface, as discussed in section B.1 in context of Equation (B2).

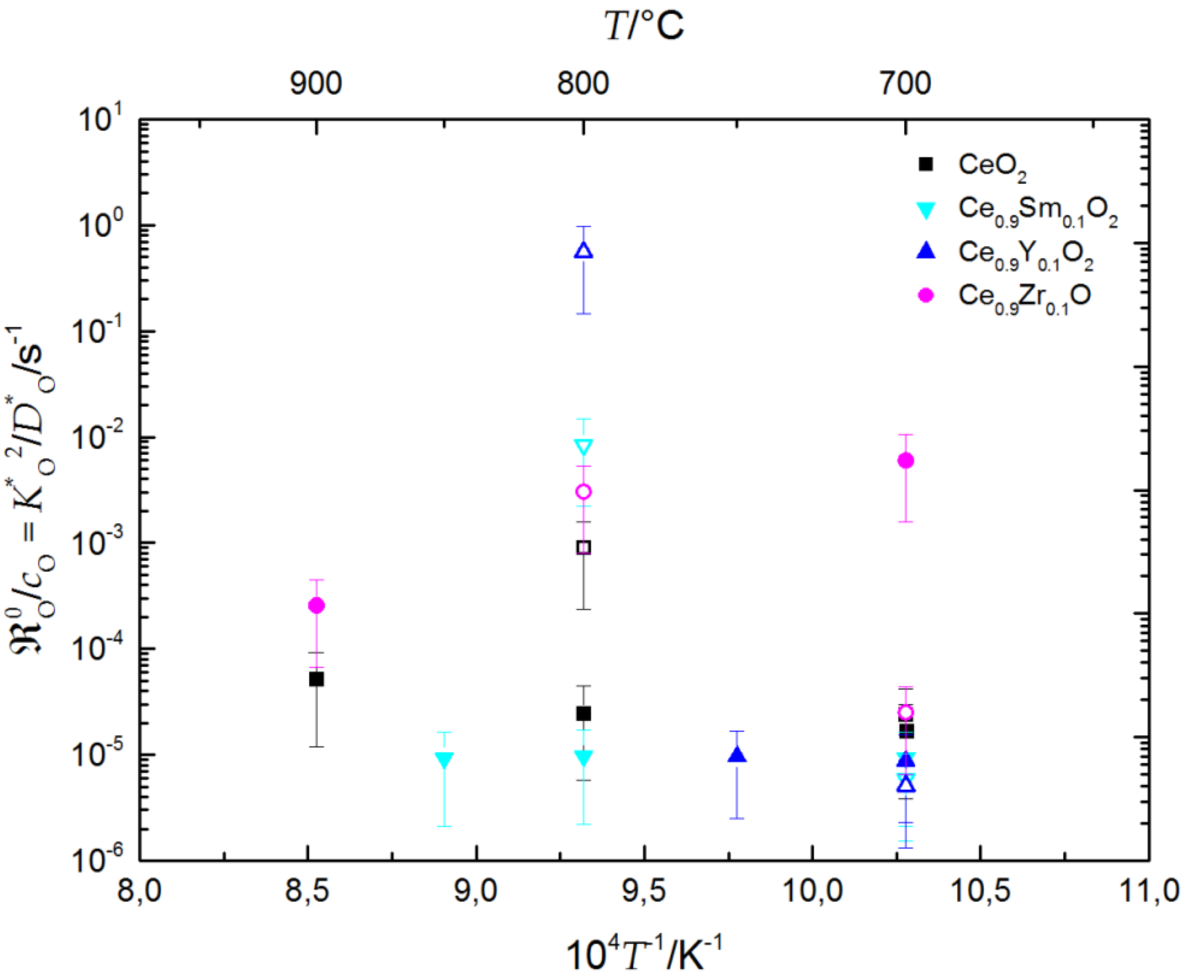

Figure 27. Calculated normalized exchange rate $\Re_O^0 / c_O(x=0) = \left(K_O^*\right)^2 / D_O^*$ for equilibrium oxygen isotope exchange from $^{18}O_2$ (solid data points) and $C^{18}O_2$ (open data points) in the temperature range from T = 700 °C to T = 900 °C for ceria containing 10 at-% of dopants (Y, Sm, Zr) and in nominally un-doped ceria samples.

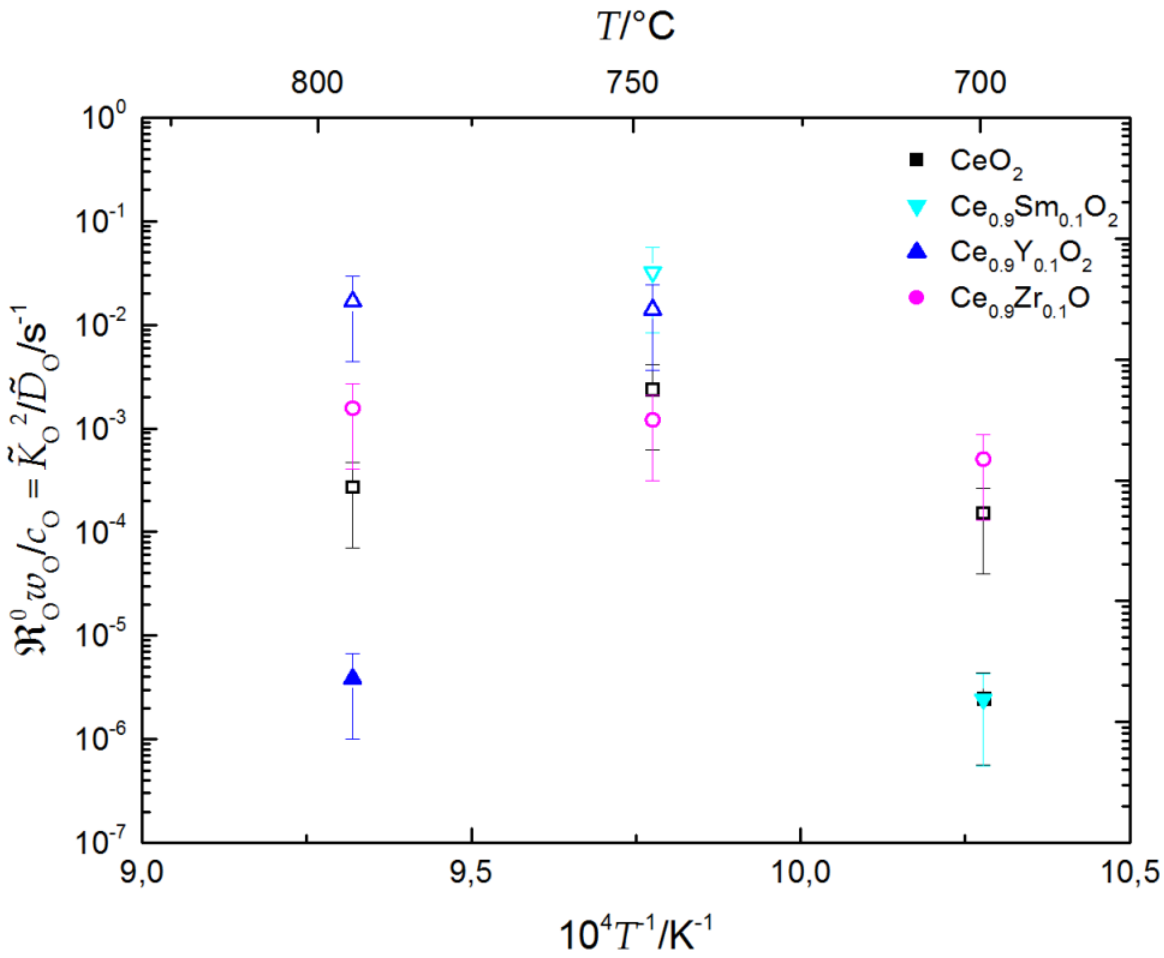

Figure 28. Calculated normalized exchange rate $\Re_O^0 w_O(x=0)/c_O(x=0)=\left(\tilde{K}_O\right)^2/\tilde{D}_O$ for non-equilibrium oxygen isotope exchange from $^{18}O_2$ (solid data points) and $C^{18}O_2$ (open data points) in the temperature range from $T = 700$ °C to $T = 800$ °C for ceria containing 10 at-% of dopants (Y, Sm, Zr) and in nominally un-doped ceria samples.

Because of the strong scattering of the calculated data, which is induced by the different gas atmospheres and sample types as discussed in section 6.7, a definite temperature dependency of the normalized exchange rate cannot be identified. The observed apparent temperature independency of $\Re_O^0$ and its further impact on the determination of the apparent activation energy of the surface exchange coefficient [Knob15, Fiel16] is discussed in section 6.8.

6.7 Discussion of the oxygen exchange kinetics under different experimental conditions

Further analysis of the oxygen exchange kinetics and their dependency on the given experimental conditions (gas atmosphere, sample type, temperature) is done by comparing the calculated diffusion coefficients $D_\mathrm{O}^*, \tilde{D}_\mathrm{O}$ and exchange coefficients $K_\mathrm{O}^*, \tilde{K}_\mathrm{O}$ as well as the exchange rates $\Re_\mathrm{O}^0 / c_\mathrm{O}(x=0) = \left(K_\mathrm{O}^*\right)^2 / D_\mathrm{O}^*$ and $\Re_\mathrm{O}^0 w_\mathrm{O}(x=0) / c_\mathrm{O}(x=0) = \left(\tilde{K}_\mathrm{O}\right)^2 / \tilde{D}_\mathrm{O}$ at temperatures of T = 700 °C and T = 800 °C, which is shown in Figures 29, 30 and 31.

The chemical diffusion coefficient of oxygen $\tilde{D}_\mathrm{O}$ is coupled via the thermodynamic factor of oxygen w_O with the tracer diffusion coefficient, $\tilde{D}_\mathrm{O} = w_\mathrm{O}(x=0) D_\mathrm{O}^*$, where $w_\mathrm{O}(x=0)$ is related to μ_O according to the relation $w_\mathrm{O}(x=0) = \frac{c_\mathrm{O}(x=0)}{RT} \left.\frac{\partial \mu_\mathrm{O}}{\partial c_\mathrm{O}}\right|_{x=0}$ as shown in section E.1 of the appendix. In contrast to the diffusivities, $\tilde{K}_\mathrm{O}$ and K_O^* are coupled via $\tilde{K}_\mathrm{O} = \sqrt{w_\mathrm{O}(x=0)} K_\mathrm{O}^*$, as discussed in section E.4. The relation between the thermodynamic factor of oxygen and the oxygen non-stoichiometry can be written in a more generalized form as $w_\mathrm{O}(n,\delta) = \frac{1}{2n}\frac{1}{\delta}$ as given in section E.5 in more detail. The three different experimental conditions that are compared are again summarized in Table 6 (similar to Table 1 in section 5.3).

Table 6. Experimental parameters related to the experimental condition numbers shown in Figures 29, 30 and 31. The oxygen activity during annealing in Ar/C^{18}O$_2$ gas atmosphere at T = 700 °C and T = 800 °C is estimated according to Figure 10.

Condition number	Gas atmosphere	Oxygen activity of gas atmosphere	Experimental condition
1	^{18}O$_2$	a_{O_2} = 0.2 bar	equilibrium
2	Ar/C^{18}O$_2$ (10:1)	$10^{-12} \leq p_{\mathrm{O}_2} \leq 10^{-15}$ bar	equilibrium
3	Ar/C^{18}O$_2$ (10:1)	$p_{\mathrm{O}_2} \leq 10^{-12}$ bar	chemical potential gradient

The exact role of the platinum support was neither an objective nor could it be quantified in the context of this work. Literature data [Buen08] suggests that at elevated temperatures a potential Pt effect is no longer dominant and also depends on the dopant. In general Pt accelerates the oxygen exchange rate at 200 °C ≤ T ≤ 400 °C, most probably through the accelerated nature of the bond breaking of C-^{18}O bonds [Buen08].

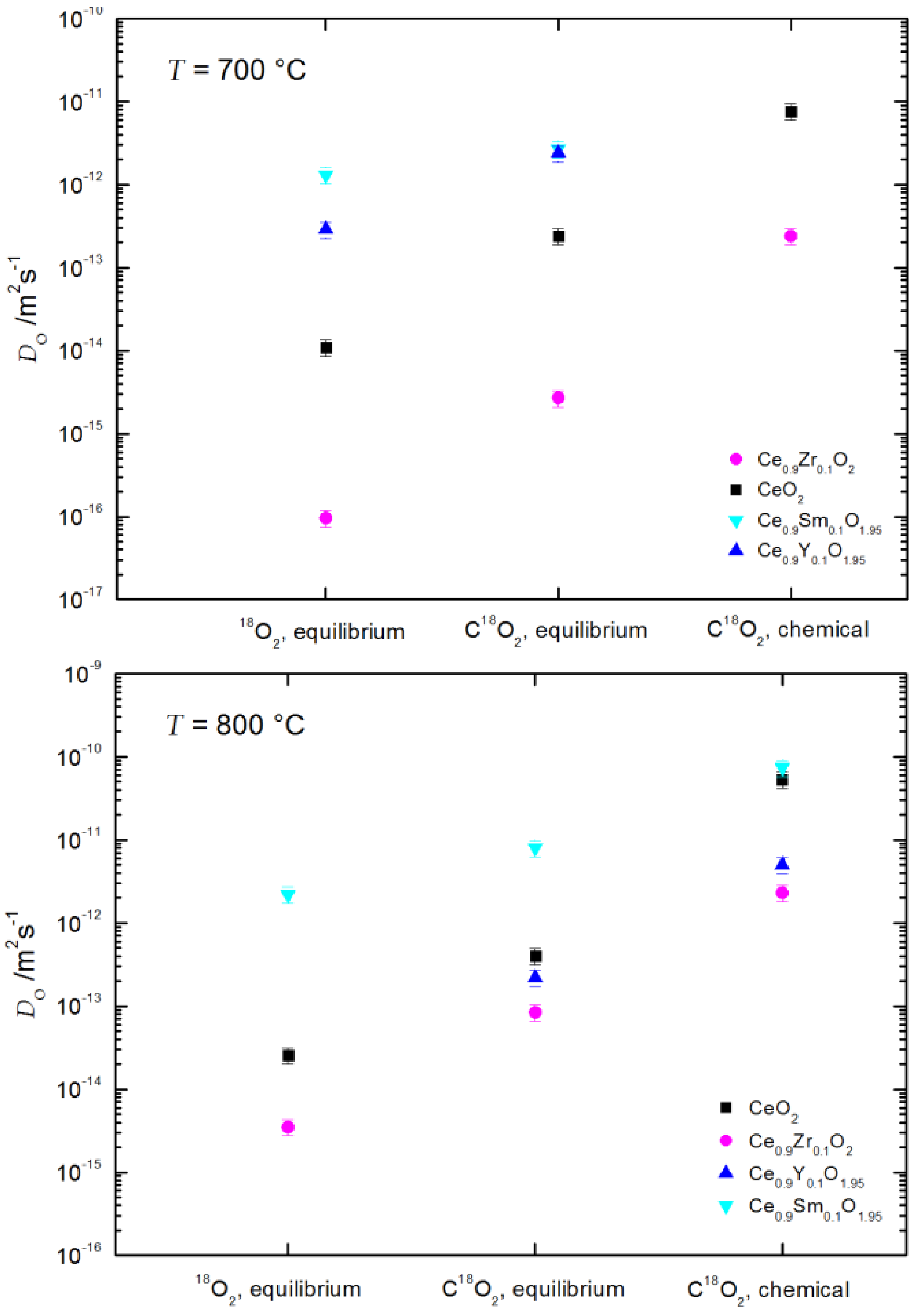

Figure 29. Graphical compilation of calculated diffusion coefficients $D_O^*, \tilde{D}_O$ at temperatures of T = 700 °C (top) and T = 800 °C (down) under three different experimental conditions (see Table 1) for ceria containing 10 at-% dopants (Y, Sm, Zr) and of nominally un-doped ceria samples.

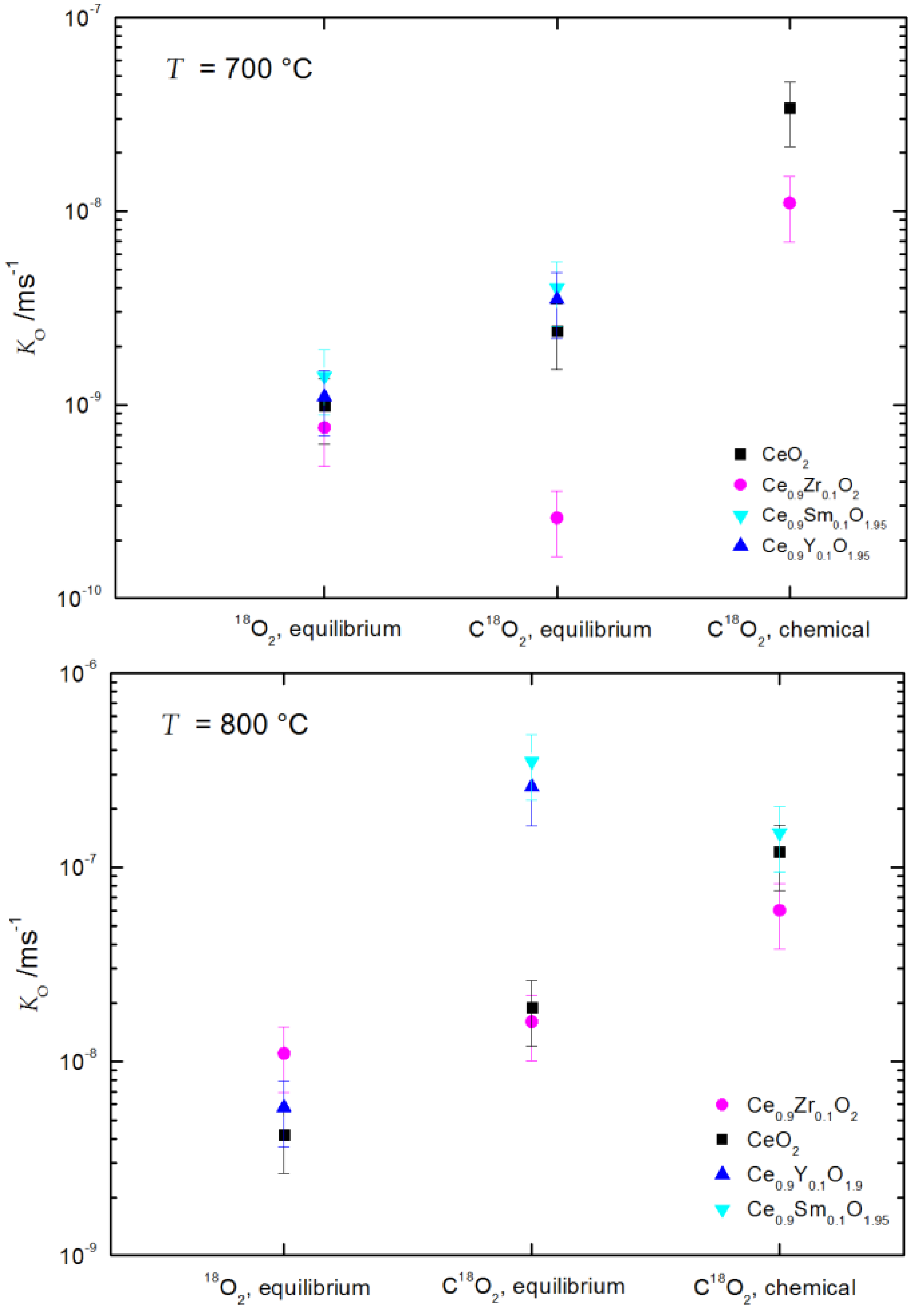

Figure 30. Graphical compilation of calculated exchange coefficients $K_0^*, \tilde{K}_0$ at temperatures of T = 700 °C (top) and T = 800 °C (down) under three different experimental conditions (see Table 1) for ceria containing 10 at-% dopants (Y, Sm, Zr) and of nominally un-doped ceria samples.

The overall trends of the calculated diffusion coefficients (as a function of the oxygen activity on the one hand and of the nature and the concentration of the different dopants on the other hand) can be semi-quantitatively rationalized based on the respective total oxygen vacancy concentration (Figure 29). With the exception of Zr-doped ceria at $T = 700$ °C and Sm/Y-doped ceria samples at $T = 800$ °C, a similar trend, though less directly evident, is observed for the exchange coefficients (Figure 30).

Differences in a_{O_2} between O_2 and Ar/CO_2 gas atmospheres at a given temperature, leading to non-stoichiometric ceria samples (confer Tables 7 and 8), have to be taken into account when comparing and interpreting the experimental results. Ceria samples in contact with Ar/CO_2 release oxygen and are non-stoichiometric in chemical equilibrium, due to the low oxygen activity in Ar/CO_2.

In Tables 9 and 10 the calculated values of the thermodynamic factor of oxygen w_O, derived from K and D data sets, and values for n for the general relation $\delta \sim p_{O_2}^{-n}$ (confer chapter 4 and section E.5 of the appendix) are given for $T = 700$ °C and $T = 800$ °C. In a chemical oxygen exchange experiment w_O typically yields values of $w_O >> 1$ [Clau00, Leon02]. CLAUS et al. give experimental values of $w_O \approx 10^5$ at 600 °C $\leq T \leq$ 800 °C for Fe-doped $SrTiO_3$, where internal trapping effects caused by valance changes of the redox-active Fe-doping (Fe^{3+} to Fe^{4+}) influence the thermodynamic factor [Clau00].

As can be seen the calculated values exhibit $32 \leq w_O = \frac{\tilde{D}_O}{D_O^*} \leq 89$ at $T = 700$ °C and $9 \leq w_O = \frac{\tilde{D}_O}{D_O^*} \leq 132$ at $T = 800$ °C, as well as $201 \leq w_O = \left(\frac{\tilde{K}_O}{K_O^*}\right)^2 \leq 1790$ at $T = 700$ °C and $0.2 \leq w_O = \left(\frac{\tilde{K}_O}{K_O^*}\right)^2 \leq 40$ at $T = 800$ °C, with $w_O = \left(\frac{\tilde{K}_O}{K_O^*}\right)^2 = 0.2$ at $T = 800$ °C for $Ce_{0.9}Y_{0.1}O_{2-\delta}$ obviously being an outlier. Due to the insufficient accuracy of the experimentally determined D and K values, these values should rather be regarded as estimates, including outliers.

Nevertheless, further estimations regarding the n value are possible. PANLENER and co-workers [Panl75] discussed the more general form of $\delta \sim p_{O_2}^{-n}$ for $CeO_{2-\delta}$ with $n << 1$ at $T = 750$ °C.

In this work values of 0.01 to 0.05 where calculated for $CeO_{2-\delta}$ at T = 700 °C and 0.02 to 0.06 at T = 800 °C utilizing the approximate relation $n = \frac{1}{2w_O\delta}$. The n values for other ceria sample types are in the same order of magnitude, with the outlier of $Ce_{0.9}Y_{0.1}O_{2-\delta}$ at T = 800 °C.

Table 7. Estimated non-stoichiometry (δ values) of ceria samples during the annealing in $Ar/C^{18}O_2$ gas atmosphere at T = 700 °C based on literature data [Beva64, Panl75]. The oxygen release in equilibrium conditions occurs due to the low oxygen activity of the Ar/CO_2 gas atmosphere and can only be delimited.

Sample type	δ of sample in Ar/CO_2 (chemical)	δ of sample in Ar/CO_2 (equilibrium)
$CeO_{2-\delta}$	0.3	< 0.025
$Ce_{0.9}Zr_{0.1}O_{2-\delta}$	0.35	< 0.025
$Ce_{0.9}Sm_{0.1}O_{1.95-\delta}$ /$Ce_{0.9}Y_{0.1}O_{1.95-\delta}$	-	-

Table 8. Estimated non-stoichiometry (δ values) of ceria samples during annealing in $Ar/C^{18}O_2$ gas atmosphere at T = 800 °C based on literature data [Beva64, Panl75]. The oxygen release in equilibrium conditions occurs due to the low oxygen activity of the Ar/CO_2 gas atmosphere and can only be delimited.

Sample type	δ of sample in Ar/CO_2 (chemical)	δ of sample in Ar/CO_2 (equilibrium)
$CeO_{2-\delta}$	0.2	< 0.025
$Ce_{0.9}Zr_{0.1}O_{2-\delta}$	0.32	< 0.025
$Ce_{0.9}Sm_{0.1}O_{1.95-\delta}$ /$Ce_{0.9}Y_{0.1}O_{1.95-\delta}$	0.175	-

Table 9. Calculated values of the thermodynamic factor w_O from *K*/*D* data sets for CO_2 splitting and values for *n* for the general relation $\delta \sim p_{\mathrm{O}_2}^{-n}$ at T = 700 °C.

Sample type	$w_\mathrm{O} = \frac{\tilde{D}_\mathrm{O}}{D_\mathrm{O}^*}$	$w_\mathrm{O} = \left(\frac{\tilde{K}_\mathrm{O}}{K_\mathrm{O}^*}\right)^2$	δ	$n = \frac{1}{2w_\mathrm{O}\delta}$
$CeO_{2-\delta}$	32	201	0.3	0.01 … 0.05
$Ce_{0.9}Zr_{0.1}O_{2-\delta}$	89	1790	0.35	0.001 … 0.015

Table 10. Calculated values of the thermodynamic factor w_O from *K*/*D* data sets for CO_2 splitting and values for *n* for the general relation $\delta \sim p_{\mathrm{O}_2}^{-n}$ at T = 800 °C.

Sample type	$w_\mathrm{O} = \frac{\tilde{D}_\mathrm{O}}{D_\mathrm{O}^*}$	$w_\mathrm{O} = \left(\frac{\tilde{K}_\mathrm{O}}{K_\mathrm{O}^*}\right)^2$	δ	$n = \frac{1}{2w_\mathrm{O}\delta}$
$CeO_{2-\delta}$	132	40	0.2	0.02 … 0.06
$Ce_{0.9}Zr_{0.1}O_{2-\delta}$	27	14	0.32	0.06 … 0.11
$Ce_{0.9}Sm_{0.1}O_{1.95-\delta}$	9	-	0.175	0.32
$Ce_{0.9}Y_{0.1}O_{1.95-\delta}$	23	0.2	0.175	0.125 … 14.5

For a deeper understanding, the normalized equilibrium exchange rate constants $\Re_\mathrm{O}^0 / c_\mathrm{O}(x=0) = \left(K_\mathrm{O}^*\right)^2 / D_\mathrm{O}^*$ and $\Re_\mathrm{O}^0 w_\mathrm{O}(x=0) / c_\mathrm{O}(x=0) = \left(\tilde{K}_\mathrm{O}\right)^2 / \tilde{D}_\mathrm{O}$ at temperatures of T = 700 °C and T = 800 °C have to be evaluated, which are identical with the reciprocal characteristic time constant to reach (isotope) equilibrium at the surface, as discussed in sections 4.3 and B.1 of the appendix. The results shown in Figure 31 reflect obvious dependencies on sample doping and oxygen activity (and thus on the respective experimental conditions).

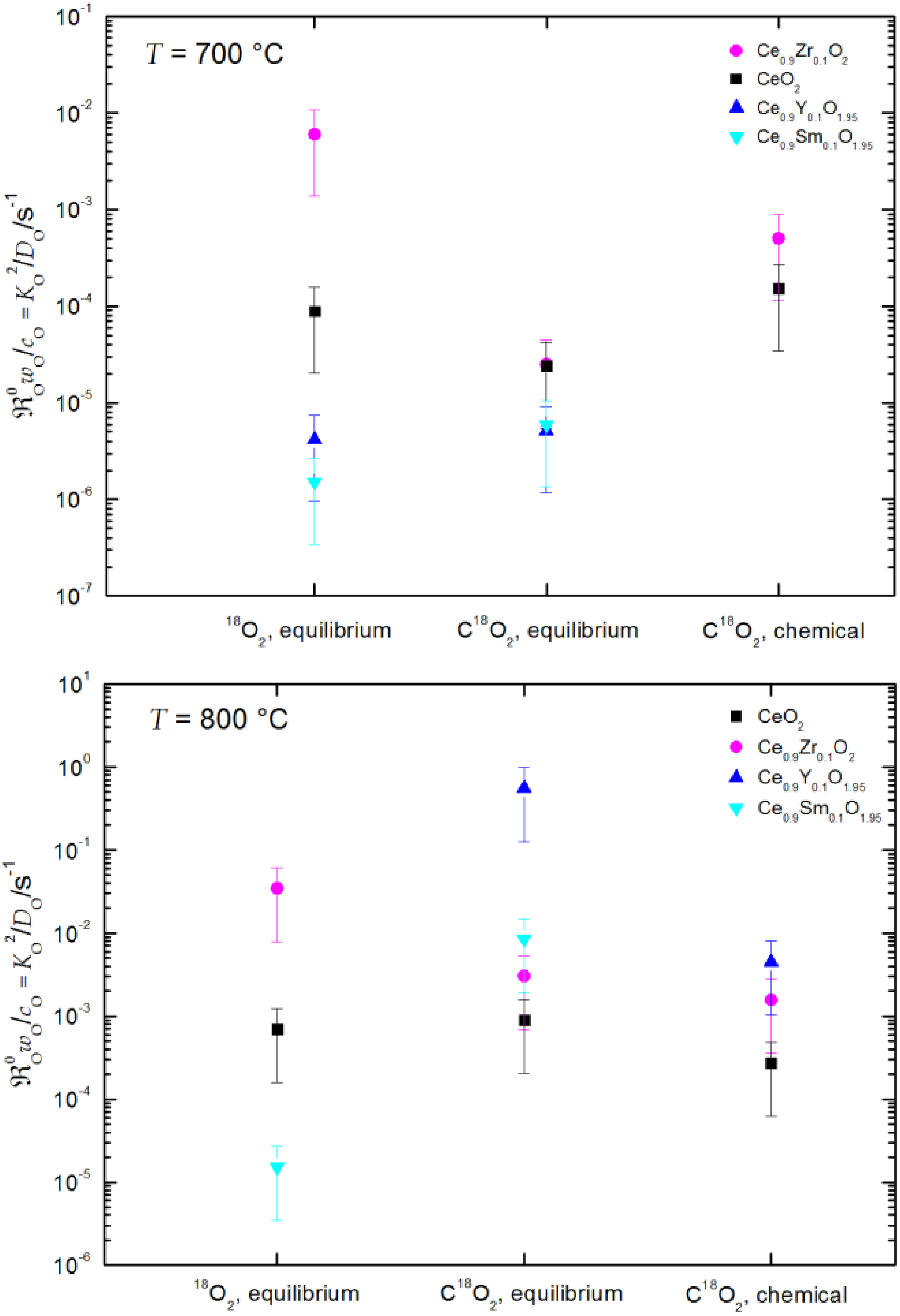

Figure 31. Graphical compilation of the calculated normalized equilibrium exchange rates at temperatures of T = 700 °C (top) and T = 800 °C (down) under three different experimental conditions (see Table 1) for ceria containing 10 at-% of dopants (Y, Sm, Zr) and in nominally un-doped ceria samples with 0.2 at-% La contamination.

They can be qualitatively interpreted with the aid of an empirical expression for $\Re_{\mathrm{O}}^{0}$ as discussed in section E.2 of the appendix (Equations (E8) and (E13)), which yields in the case of oxygen incorporation in ceria from pure oxygen:

$$\Re_{\mathrm{O}}^{0} \sim \left(\left[\mathrm{O}_{\mathrm{O}}^{\times}\right]\left[\mathrm{e}'\right]\left[\mathrm{h}^{\bullet}\right]\right)^{\frac{1}{2}} \frac{p_{\mathrm{O}_2}^{\frac{1}{4}}}{\left[\mathrm{V}_{\mathrm{O}}^{\bullet\bullet}\right]^{\frac{1}{2}}}. \tag{53}$$

For the case of CO$_2$ splitting on ceria the empirical expression changes to:

$$\Re_{\mathrm{O}}^{0} \sim \frac{\left[\mathrm{CO}_2\right]\left(\left[\mathrm{O}_{\mathrm{O}}^{\times}\right]\right)^{\frac{1}{2}}}{\left[\mathrm{V}_{\mathrm{O}}^{\bullet\bullet}\right]^{\frac{1}{2}} p_{\mathrm{O}_2}^{\frac{1}{4}}}. \tag{54}$$

The obvious differences concerning the p_{O_2} and $\left[\mathrm{V}_{\mathrm{O}}^{\bullet\bullet}\right]$ dependency of $\Re_{\mathrm{O}}^{0}$ considering both cases have to be taken into account. If the concentration terms are considered constant, it is possible to explain the relative ratio of the $\Re_{\mathrm{O}}^{0}$ values at T = 700 °C and T = 800 °C in Figure 31 for all experimental conditions by assuming values for p_{O_2} and $\left[\mathrm{V}_{\mathrm{O}}^{\bullet\bullet}\right]$, which is schematically also shown in Figure 32.

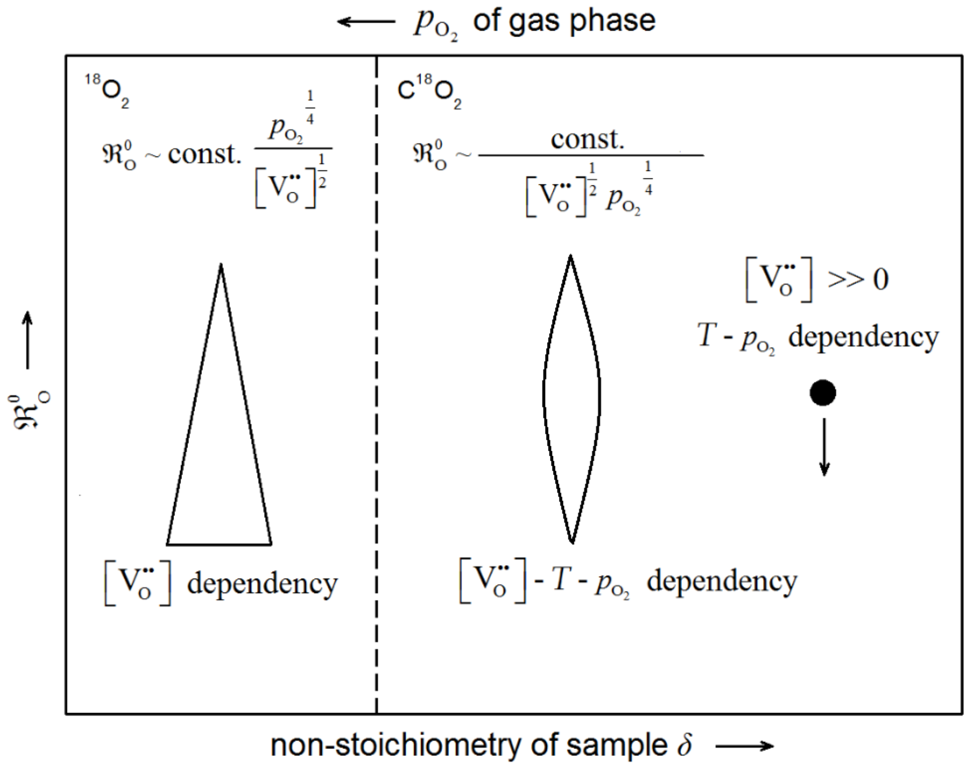

Figure 32. Scheme of the p_{O_2} and $\left[\mathrm{V}_{\mathrm{O}}^{\bullet\bullet}\right]$ dependency of $\Re_{\mathrm{O}}^{0}$ considering both O$_2$ and CO$_2$ gas atmospheres.

In the case of oxygen exchange from pure oxygen in equilibrium conditions (1) $\Re_{\mathrm{O}}^{0}$ increases with decreasing concentration of oxygen vacancies and tends toward an infinite value for $\left[\mathrm{V}_{\mathrm{O}}^{\bullet\bullet}\right] \rightarrow 0$. The concentration of lanthanum (about 0.2 at-%) in the nominally un-doped ceria sample has to be taken into account as trivalent dopant. As can be seen, $\Re_{\mathrm{O}}^{0}$ decreases with increasing concentration of the trivalent dopant in the case of $Ce_{0.9}Sm_{0.1}O_{1.95}$ and $Ce_{0.9}Y_{0.1}O_{1.95}$. Zr seems to neutralize the La contamination in the sense of suppressing the formation of oxygen vacancies.

In the case of oxygen exchange in equilibrium conditions from carbon dioxide gas atmosphere (2) the relation is more complex, as $\Re_{\mathrm{O}}^{0}$ increases with decreasing concentration of oxygen vacancies, but also depends on the oxygen partial pressure of the surrounding gas atmosphere. For this experimental condition the gas phase has an oxygen activity of a_{O_2} = 10^{-15} at T = 700 °C and a_{O_2} = 10^{-12} at T = 800 °C, leading to differences concerning the p_{O_2} dependency.

Considering the $\left[\mathrm{V}_{\mathrm{O}}^{\bullet\bullet}\right] - T - p_{\mathrm{O}_2}$ dependency it can be seen that $\Re_{\mathrm{O}}^{0}$ has higher values at T = 800 °C for the experimental condition (2) in comparison to (3). At T = 700 °C the $\Re_{\mathrm{O}}^{0}$ data is significantly overlapping, which is a hint that the samples might not have been in true equilibrium and that $\left[\mathrm{V}_{\mathrm{O}}^{\bullet\bullet}\right]$ is increased. This is the case for the experimental condition (3) where all samples are significantly non-stoichiometric and the high concentration of oxygen vacancies limits the influence of dopants. In non-equilibrium conditions during carbon dioxide splitting the oxygen activity of the gas phase controls the exchange rate of oxygen. This leads to the unexpected, though not really paradox, result that at T = 700 °C the determined values reach nearly the same order of magnitude as at T = 800 °C because of the $T - a_{\mathrm{O}_2}$ correlation given in Figure 10.

6.8 Discussion of the oxygen exchange kinetics considering the determined apparent activation enthalpies

As discussed in section 4.1, defects in cerium dioxide can be classified as intrinsic or extrinsic. Intrinsic defects may be present because of thermal disorder or can be created by reaction between the solid and the surrounding atmosphere, whereas extrinsic defects are formed by impurities or by the introduction of dopants.

Therefore the determined oxygen tracer diffusivity can be classified either as extrinsic or intrinsic. In the extrinsic regime, which is also referred to as a “low temperature” regime, the measured oxygen diffusion coefficient is controlled by aliovalent dopants or impurities which introduce extrinsic oxygen vacancies as given in Equations (16) and (17), so that the magnitude of the measured diffusion coefficient depends on the defect concentration as given by Equation (32). At higher temperatures (T > 1000 °C) the region of true intrinsic diffusive behavior of undoped ceria can be found, where the measured oxygen diffusion coefficient is controlled by thermally activated oxygen vacancies [Kami98, Kami00].

The defect concentration can be estimated with reference to the electroneutrality condition by $D_{\mathrm{O}^{2-}} \sim \left[\mathrm{Me}'_{\mathrm{Ce}}\right] D_{\mathrm{V}_{\mathrm{O}}^{\bullet\bullet}}$ (as discussed previously in section 4.2). In a $\log\left(D_{\mathrm{O}^{2-}}\right) - \log\left(\left[\mathrm{Me}'_{\mathrm{Ce}}\right]\right)$ plot a linear relationship between the determined diffusivity and the impurity concentration can be observed [Kami00]. The concentration of lanthanum (about 0.2 at-%) in the nominally undoped ceria sample has to be taken into account as trivalent dopant, similar to the 10 at-% Y-doped and Sm-doped ceria samples, and it is therefore reasonable to assume that the oxygen tracer diffusion in the low temperature region $700\ ^{\circ}\mathrm{C} \leq T \leq 900\ ^{\circ}\mathrm{C}$ is impurity controlled and therefore extrinsic, as can be seen in Figure 16.

The activation enthalpy ΔH_{a} in the extrinsic region corresponds to the enthalpy of oxygen ion migration ΔH_{m} and the calculated values of (1.02 ± 0.11) eV for nominally undoped ceria and of (0.89 ± 0.13) eV for 10 at-% Sm-doped ceria are close to the value of 0.87 eV reported by Kamiya et al. [Kami00] for pure ceria and of 0.9 eV reported by Manning et al. [Mann97] for 10 at-% Gd-doped ceria. The difference in magnitude of the oxygen tracer diffusivity for nominally undoped ceria and Sm-doped ceria samples is therefore due to the difference in the concentration of the trivalent dopant/impurity.

Interestingly the calculated value of ΔH_{a} for oxygen tracer diffusion in 10 at-% Zr-doped ceria in the low temperature region yields (2.45 ± 0.38) eV, which is very close to the value of 2.34 eV Kamiya et al. reported for the intrinsic region T > 1000 °C of pure ceria, where ΔH_{a} corresponds to both the enthalpy of defect formation and oxygen ion migration by $\Delta H_{\mathrm{a}} = \left(\Delta H_{\mathrm{f}} / 3\right) + \Delta H_{\mathrm{m}}$ [Kami00] (see section 4.2).

As discussed in section 6.7 the Zr dopants seem to neutralize the La contamination in the nominally undoped ceria. The calculated value for ΔH_{f} of 4.29 eV is close to the reported values of 4.45 eV by Kamiya et al. [Kami00] and 4.7 eV by Blumenthal et al. [Blum71], although it is not possible to conclude on the reason for this apparent intrinsic-type oxygen diffusion in Zr-doped ceria in the low temperature region based on the results of the oxygen tracer diffusion measurements.

In Figure 17 a comparison of the determined oxygen tracer surface exchange coefficients of this work to literature data taken from KAMIYA et al. [Kami00] for nominally undoped ceria and FLOYD [Floy73] and MANNING et al. [Mann97] for trivalent doped ceria is shown. In general the determined K_{O}^{*} data differ from literature data and show little pronounced temperature dependence. The calculated value of the overall activation enthalpy ΔH_{a} for oxygen surface exchange of nominally undoped ceria of (0.78 ± 0.23) eV in this work is nearly half of the value of 1.41 eV reported by KAMIYA and co-workers.

The calculated value of $\Delta H_{\mathrm{a}}^{K_{\mathrm{O}}^{*}}$ for 10 at-% Sm-doped ceria of (0.53 ± 0.14) eV in this work is close to the value of 0.6 eV reported by Manning et al. [Mann97] for 10 at-% Gd-doped ceria at low temperatures. Regarding the Zr-doped ceria samples it can be determined that the K_{O}^{*} data at T = 700 °C and T = 900 °C is close to the value for nominally undoped ceria.

Concerning the non-equilibrium oxygen exchange kinetics the calculation of the apparent overall activation enthalpy is based on the oxygen isotope exchange experiments utilizing $C^{18}O_2$ in the temperature range 300 °C $\leq T \leq$ 800 °C.

In section 6.7 it was shown that the relation between the thermodynamic factor of oxygen and the oxygen non-stoichiometry directly determines the measured chemical diffusivity, which explains the observable scatter of $\tilde{D}_{\mathrm{O}}$ values in Figure 20 due to variation of δ from 0.15 to 0.22.

In general the calculated overall activation enthalpies for chemical diffusion of oxygen for trivalent-doped and nominally undoped ceria of (0.46 ± 0.04) eV, (0.56 ± 0.03) eV and (0.87 ± 0.13) eV represent the oxygen ion migration energy ΔH_{m} only. Compared to the low temperature regime of tracer diffusivity the determined activation enthalpies of nominally undoped ceria and Sm-doped ceria are lower for chemical diffusion, which suggests a dependency of ΔH_{m} on the oxygen vacancy concentration of the reduced samples. This is attributed to the lattice expansion of the ceria crystal upon reduction, where, according to MUHICH [Muhi17b], the outward expansion of the cations neighbouring the oxygen vacancy caused by noncounterpoised forces induces long-range structural distortions.

Again the calculation of ΔH_a for non-equilibrium oxygen diffusivity of 10 at-% Zr-doped ceria in the low temperature 400 °C $\leq T \leq$ 800 °C region yields in comparison an increased value of (1.7 ± 0.08) eV, despite the high oxygen vacancy concentration of the solid. Regarding this finding, together with the results for oxygen tracer diffusion, a dopant-induced migration barrier enhancement in Zr-doped ceria has to be discussed.

It is known from theoretical calculations by GRIESHAMMER et al. [Gries17b, Gries18] that in Zr-doped ceria a strong attraction can be found between Zr^{4+} ions and oxygen vacancies, in comparison to trivalent doped ceria, which is due to the small size of the zirconium ion, allowing favorable relaxation around the oxygen vacancy. Therefore the authors identified three major influences on the ionic conductivity, which are the trapping of oxygen vacancies by dopant ions, the blocking effect, which alters the migration barriers around defects, and the lattice contradiction due to Zr-doping.

Furthermore, EUFINGER et al. [Eufi14] showed experimentally, that the conductivity in Y-doped ceria is significantly decreased by Zr-doping. The experimental findings on the oxygen diffusivity of this work therefore also suggest a dopant-vacancy interaction induced migration barrier enhancement in Zr-doped ceria.

The calculated activation enthalpies for chemical oxygen diffusivity for trivalent-doped and nominally undoped ceria differ by 0.41 eV and 0.29 eV, respectively, which is not the case for oxygen tracer diffusion. Here, the effects of the high oxygen vacancy concentrations on the bulk transport properties must be considered. As described in section 4.1, isolated defects can interact to form defect complexes with increasing oxygen non-stoichiometry.

BISHOP et al. discussed various defect complexes that can potentially form and found isolated defects and intrinsic trimers composed of reduced cations and oxygen vacancies in the form of $\left(\mathrm{Ce}'_{\mathrm{Ce}}\mathrm{V}_{\mathrm{O}}^{\bullet\bullet}\mathrm{Ce}'_{\mathrm{Ce}}\right)^{\times}$ to be the most significant ones [Bish09a, Bish09b].

A comparison of $CeO_{2-\delta}$ and $Ce_{0.9}Gd_{0.1}O_{1.95-\delta}$ showed differences in the chemical expansion as a function of p_{O_2}, which is explained by an increased tendency of undoped ceria to form defect complexes, changing the ratio of defect complexes to isolated defects. At a non-stoichiometry of $\delta = 0.15$, undoped ceria exhibits a calculated intrinsic trimer fraction of 86 %, whereas 10 at-% Gd-doped ceria exhibits an intrinsic trimer fraction of 62 %, having a higher fraction of isolated defects.

Based on the current knowledge it can be speculated that intrinsic trimers influence the ionic transport by trapping of the oxygen vacancy itself and the alteration of the migration barriers around the defect complex, which is also indicated by the difference in chemical oxygen diffusivity by one order of magnitude for 10 at.-% Sm-doped ceria at room temperature, as described in section 6.4.

The determined $\tilde{K}_{\mathrm{O}}$ data for nominally undoped and trivalent doped ceria shows also only weak temperature dependence. Concerning the increased value of $\Delta H_{\mathrm{a}}^{\tilde{K}_{\mathrm{O}}}$ for the Zr-doped ceria, which is not indicated by the oxygen tracer surface exchange data, reported findings on surface alteration effects under low oxygen partial pressure and high temperatures by KNOBLAUCH et al. [Knob17] can explain the observed differences. Selective surface evaporation of ceria, whose vapor pressure is considerably higher than that of zirconia, and segregation of zirconia can lead to a porous surface zone of $Ce_2Zr_2O_7$ pyrochlore and consequently to a surface enrichment of zirconia. Zr-doped ceria that is slightly different in its composition and surface structure might induce significant differences in oxygen surface exchange that lead to a different value of $\Delta H_{\mathrm{a}}^{\tilde{K}_{\mathrm{O}}}$.

A comparison can be made to $\tilde{K}_{\mathrm{O}}$ data obtained in the true exchange controlled kinetic regime, as the $\tilde{K}/\tilde{D}$ ratios of this work suggest a diffusion controlled or mixed kinetic regime at $T \leq 800$ °C, as discussed in section 6.5. KNOBLAUCH et al. [Knob15] discussed surface exchange controlled reduction kinetics at higher temperatures of $T \geq 1300$ °C for nominally undoped CeO_2 (polycrystalline CeO_2 samples of 1 mm thickness) using thermogravimetric analysis in non-equilibrium conditions and found that $\tilde{K}_{\mathrm{O}}$ shows a very weak or even formally negative activation enthalpy (if the typical errors of ± 0.05 eV are neglected), a finding that was also made by ACKERMANN [Acke14b] and co-workers. The influence of the kinetic regime on the apparent activation enthalpy of the surface exchange coefficient was thoroughly discussed by FIELITZ and BORCHARDT [Fiel16] (see section 4.3 Equations (43) and (44)). They suggest that the measured oxygen surface exchange coefficient K_{O}, if measured in the mixed regime and in the diffusion controlled kinetic regime, depends not only on the equilibrium oxygen exchange rate $\Re_{\mathrm{O}}^{0}$ at the gas/solid interface but also on the oxygen diffusion coefficient D_{O} in the bulk, meaning that for sufficiently thick samples as used in this work the determined apparent $\Delta H_{\mathrm{a}}^{\tilde{K}_{\mathrm{O}}}$ is the mean value of the individual activation enthalpies $\Delta H_{\mathrm{a}}^{\tilde{D}_{\mathrm{O}}}$ and $\Delta H_{\mathrm{a}}^{\Re_{\mathrm{O}}^{0}}$.

According to this theory, $\Delta H_{\mathrm{a}}^{\Re_{\mathrm{O}}^{0}}$ can be estimated by the relation $\Delta H_{\mathrm{a}}^{\Re_{\mathrm{O}}^{0}} = 2\Delta H_{\mathrm{a}}^{\tilde{K}_{\mathrm{O}}} - \Delta H_{\mathrm{a}}^{\tilde{D}_{\mathrm{O}}}$, which is shown in Table 11, yielding values between 0.5 and 0.7 eV. The relation $\Delta H_{\mathrm{a}}^{\Re_{\mathrm{O}}^{0}} = 2\Delta H_{\mathrm{a}}^{\tilde{K}_{\mathrm{O}}} - \Delta H_{\mathrm{a}}^{\tilde{D}_{\mathrm{O}}} \approx 0.5\ \mathrm{eV}$ is suggested as a rough estimate.

Table 11. Calculated values of the apparent activation enthalpy of the oxygen exchange rate $\Re_{\mathrm{O}}^{0}$ with regard to the relation $\Delta H_{\mathrm{a}}^{\Re_{\mathrm{O}}^{0}} = 2\Delta H_{\mathrm{a}}^{\tilde{K}_{\mathrm{O}}} - \Delta H_{\mathrm{a}}^{\tilde{D}_{\mathrm{O}}}$.

Sample type	$\Delta H_{\mathrm{a}}^{\tilde{K}_{\mathrm{O}}}$/eV	$\Delta H_{\mathrm{a}}^{\tilde{D}_{\mathrm{O}}}$/eV	$\Delta H_{\mathrm{a}}^{\Re_{\mathrm{O}}^{0}} = \left(2\Delta H_{\mathrm{a}}^{\tilde{K}_{\mathrm{O}}} - \Delta H_{\mathrm{a}}^{\tilde{D}_{\mathrm{O}}}\right)$/eV
$CeO_{2-\delta}$	0.7	0.87	0.53
$Ce_{0.9}Zr_{0.1}O_{2-\delta}$	1.1	1.7	0.5
$Ce_{0.9}Sm_{0.1}O_{1.95-\delta}$	0.58	0.46	0.7
$Ce_{0.9}Y_{0.1}O_{1.95-\delta}$	0.6	0.56	0.64

Concerning the temperature dependency of the normalized exchange rate $\Re_{\mathrm{O}}^{0}$ the contribution of w_{O} and c_{0} to $\Delta H_{\mathrm{a}}^{\Re_{\mathrm{O}}^{0}}$ must be also considered, as both parameters strongly depend on the oxygen non-stoichiometry δ. Based on the work of CLAUS et al. [Clau00] who give a relation of $w_{\mathrm{O}} = \frac{3c_{\mathrm{O}}}{\left[\mathrm{V}_{\mathrm{O}}^{\bullet\bullet}\right]}$ it is possible to deduce that $\frac{w_{\mathrm{O}}}{c_{\mathrm{O}}} = \frac{\text{const.}}{n\delta\left(T\right)}$. As a first approximation, one can assume that the temperature dependencies of c_{0} and w_{O} compensate each other, but there will remain a contribution to $\Delta H_{\mathrm{a}}^{\Re_{\mathrm{O}}^{0}}$ that cannot be expressed in quantitative terms by $\Delta H_{\mathrm{a}}^{\tilde{D}_{\mathrm{O}}}$ and $\Delta H_{\mathrm{a}}^{\tilde{K}_{\mathrm{O}}}$ in the context of this work.

7 Summary and overall conclusions

7.1 Summary

The focuses of this thesis is the experimental investigation of ceria-based redox materials, which are associated to two-step solar thermochemical splitting of carbon dioxide. Important detailed questions, in particular regarding the reaction kinetics, the exact influence of doping elements, the macroscopic and microscopic structure of the redox material as well as the cyclic stability, have to be answered in order to achieve a scaling of the redox process to the technical scale. The existing data gap should be minimized.

Surface exchange reactions and bulk transport of oxygen in ceria are of high relevance, therefore this work focusses on the surface reaction with carbon dioxide reduction and oxygen exchange, oxygen diffusion in bulk ceria samples, the phenomenological description (K_O, D_O), the interpretation of the calculated rate constants, the influence of the doping elements, the influence of the oxygen partial pressure of the gas atmosphere, as well as the impact of the macroscopic structural parameters on the respective kinetic regime.

The most direct method of measuring oxygen diffusivities and surface exchange coefficients in oxides is oxygen isotope exchange followed by Secondary Ion Mass Spectrometry (SIMS). By utilizing oxygen isotope enriched $^{18}O_2$ and $C^{18}O_2$ gas atmospheres and various experimental conditions this well-established approach represents the core of the experimental work of this thesis.

In accordance with the discussed established models the reaction scheme for carbon dioxide reduction on reduced ceria surfaces was deduced in section 6.1. The equilibrium exchange rate $\Re_\mathrm{O}^0$ was defined, based on the actual rate determining step (rds) of the assumed reaction scheme, yielding differences in the respective p_{O_2} dependency of $\Re_\mathrm{O}^0$.

In section 6.2 oxygen tracer diffusion coefficients D_O^* and oxygen tracer surface exchange coefficients K_O^* in ceria containing 10 at-% of dopants (Y, Sm, Zr) and in nominally un-doped ceria samples were determined in the temperature range from T = 700 to T = 900 °C utilizing $^{18}O_2$ gas atmosphere. Activation enthalpies were calculated and the determined D_O^* and K_O^* data is compared to literature data. Further chemical (non-equilibrium) oxygen diffusion coefficients $\tilde{D}_\mathrm{O}$ and oxygen surface exchange coefficients $\tilde{K}_\mathrm{O}$ in ceria containing 10 at-% of dopants (Y, Sm) and in nominally un-doped ceria samples were determined at T = 700 °C and summarized.

Section 6.3 focusses on oxygen isotope exchange experiments utilizing $C^{18}O_2$ gas atmosphere. Oxygen tracer diffusion coefficients D_{O}^{*} and oxygen tracer surface exchange coefficients K_{O}^{*} in ceria containing 10 at-% of dopants (Y, Sm, Zr) and in nominally un-doped ceria samples were determined in equilibrium conditions with a Ar/$C^{18}O_2$ gas mixture at T = 700 °C and T = 800 °C and summarized. Comparable to the low temperature step of the two-step thermochemical cycle for splitting CO_2, chemical oxygen diffusion coefficients $\tilde{D}_{\mathrm{O}}$ and oxygen surface exchange coefficients $\tilde{K}_{\mathrm{O}}$ in ceria containing 10 at-% of dopants (Y, Sm) and in nominally un-doped ceria samples were determined in the temperature range from T = 300 to T = 800 °C utilizing Ar/$C^{18}O_2$ gas mixture and activation enthalpies were calculated.

Re-oxidation of reduced ceria samples ($\delta = 0.05$ and $\delta = 0.15$) containing 10 at-% of dopants (Y, Sm, Zr) and in nominally un-doped ceria samples through interaction with $^{18}O_2$ at room temperature was determined and discussed in section 6.4. Oxygen isotope exchange in doped and un-doped ceria was observed at room temperature and results suggest a dependence of the amount of incorporated oxygen on the initial non-stoichiometry δ. The re-oxidation is related only to the sample surface and near-surface bulk region and bulk transport is limited at $T \approx 20$ °C. The determined oxygen isotope fraction profiles were utilized to approximate the chemical oxygen diffusion coefficients $\tilde{D}_{\mathrm{O}}$ at room temperature for the initial non-stoichiometry of $\delta = 0.15$.

An estimation of the kinetic regimes utilizing the K^{*}/D^{*} and $\tilde{K}/\tilde{D}$ data sets is given in section 6.5. As it turned out, oxygen tracer isotope exchange and non-equilibrium oxygen isotope exchange is either diffusion controlled or in the mixed kinetic regime in the given temperature range $T \leq 900$ °C, depending also on the respective sample type. A partial temperature dependency of the K/D ratios is indicated in the given temperature ranges. In general the results show that the K^{*}/D^{*} ratios, in the case of trivalent-doped ceria samples, and the $\tilde{K}/\tilde{D}$ ratios overall, shift from the mixed regime and tend to reach the surface exchange controlled regime at high temperatures $T \geq 700$ °C.

The normalized exchange rate $\Re_{\mathrm{O}}^{0}$ of the rate determining step in the reaction sequence at the gas/solid interface for oxygen isotope exchange from $^{18}O_2$ and $C^{18}O_2$ was calculated in section

6.6 for the respective temperature range utilizing the K^*/D^* and $\tilde{K}/\tilde{D}$ data sets. Besides a strong scattering of the calculated data, which is induced by the different gas atmospheres and sample types, a definite temperature dependency of the normalized exchange rate is in general not indicated.

Further analysis of the oxygen exchange kinetics and its dependency on the given experimental conditions (gas atmosphere, sample type, temperature) was done by comparing the calculated diffusion coefficients $D_\mathrm{O}^*, \tilde{D}_\mathrm{O}$ and exchange coefficients $K_\mathrm{O}^*, \tilde{K}_\mathrm{O}$ as well as the exchange rates $\mathfrak{R}_\mathrm{O}^0$ at temperatures of T = 700 °C and T = 800 °C in section 6.7. Values of the thermodynamic factor of oxygen w_O and values for n for the general relation $\delta \sim p_{\mathrm{O}_2}^{-n}$ were calculated for T = 700 °C and T = 800 °C.

The overall trends of the calculated diffusivities can be rationalized based on the respective total oxygen vacancy concentration. Ceria samples in contact with Ar/CO_2 gas atmospheres are non-stoichiometric due to the low oxygen activity. The dependencies on doping and oxygen activity (p_{O_2} and $\left[\mathrm{V}_\mathrm{O}^{\bullet\bullet}\right]$ - dependency) of $\mathfrak{R}_\mathrm{O}^0$ can be interpreted with the empirical expressions $\mathfrak{R}_\mathrm{O}^0 \sim \left(\left[\mathrm{O}_\mathrm{O}^\times\right]\left[\mathrm{e}'\right]\left[\mathrm{h}^\bullet\right]\right)^{\frac{1}{2}} \dfrac{p_{\mathrm{O}_2}^{\frac{1}{4}}}{\left[\mathrm{V}_\mathrm{O}^{\bullet\bullet}\right]^{\frac{1}{2}}}$ for oxygen incorporation from pure oxygen and

$\mathfrak{R}_\mathrm{O}^0 \sim \dfrac{\left[\mathrm{CO}_2\right]\left(\left[\mathrm{O}_\mathrm{O}^\times\right]\right)^{\frac{1}{2}}}{\left[\mathrm{V}_\mathrm{O}^{\bullet\bullet}\right]^{\frac{1}{2}} p_{\mathrm{O}_2}^{\frac{1}{4}}}$ for oxygen exchange with carbon dioxide splitting.

In the case of oxygen exchange from pure oxygen in equilibrium conditions $\mathfrak{R}_\mathrm{O}^0$ increases with decreasing $\left[\mathrm{V}_\mathrm{O}^{\bullet\bullet}\right]$ and strives against infinite for $\left[\mathrm{V}_\mathrm{O}^{\bullet\bullet}\right] \to 0$. The concentration of lanthanum (about 0.2 at-%) in the nominally un-doped ceria sample has to be taken into account as trivalent dopant. $\mathfrak{R}_\mathrm{O}^0$ decreases with increasing dopant concentration for $Ce_{0.9}Sm_{0.1}O_{1.95}$ and $Ce_{0.9}Y_{0.1}O_{1.95}$. Zr seems to neutralize the La contamination in the sense of suppressing the formation of oxygen vacancies.

In the case of oxygen exchange in equilibrium conditions from Ar/CO_2 gas atmosphere the relation is more complex, as $\mathfrak{R}_\mathrm{O}^0$ increases with decreasing concentration of oxygen vacancies, but also depends on the oxygen partial pressure of the surrounding gas atmosphere.

Considering the $\left[\mathrm{V}_{\mathrm{O}}^{\bullet\bullet}\right]-T-p_{\mathrm{O}_2}$ dependency it can be seen that $\Re_{\mathrm{O}}^{0}$ has higher values at T = 800 °C for equilibrium conditions in comparison to non-equilibrium conditions.

At T = 700 °C $\Re_{\mathrm{O}}^{0}$ is significantly overlapping because the samples might not have been in true equilibrium and $\left[\mathrm{V}_{\mathrm{O}}^{\bullet\bullet}\right]$ is increased. This is the case for the experimental condition where all samples are significantly non-stoichiometric and the high concentration of oxygen vacancies limits the influence of dopants. In non-equilibrium conditions during CO_2 splitting the p_{O_2} of the gas phase controls the exchange rate of oxygen.

The calculated apparent activation enthalpies are discussed in section 6.8. The lanthanum in the nominally undoped ceria sample has to be taken into account as trivalent dopant, similar to the 10 at-% Y-doped and Sm-doped ceria samples, and it is assumed that the oxygen tracer diffusion in the low temperature region 700 °C $\leq T \leq$ 900 °C is impurity controlled and therefore extrinsic.

The activation enthalpy ΔH_{a} in the extrinsic region corresponds to the enthalpy of oxygen ion migration ΔH_{m}. The difference in magnitude of D_{O}^{*} for nominally undoped ceria and 10 at-% Sm-doped ceria samples is therefore due to the difference in the dopant concentration. The calculated value of ΔH_{a} for oxygen tracer diffusion in 10 at-% Zr-doped ceria in the low temperature region is very close to the value reported for the intrinsic region T > 1000 °C of pure ceria, where ΔH_{a} corresponds to both the enthalpy of defect reaction and oxygen ion migration by $\Delta H_{\mathrm{a}} = \left(\Delta H_{\mathrm{f}} / 3\right) + \Delta H_{\mathrm{m}}$ [Kami00]. The Zr dopant seems to induce apparent intrinsic-type oxygen diffusion in Zr-doped ceria.

The K_{O}^{*} data for all ceria sample types in the low temperature region 700 °C $\leq T \leq$ 900 °C differ from literature data taken from KAMIYA et al. [Kami00], FLOYD [Floy73] and MANNING et al. [Mann97] and show little pronounced temperature dependence.

The calculated overall activation enthalpies ΔH_{a} for $\tilde{D}_{\mathrm{O}}$ for trivalent-doped and nominally undoped ceria represent the oxygen ion migration energy ΔH_{m}. Compared to the low temperature regime of tracer diffusion the determined activation enthalpies ΔH_{a} are lower for chemical diffusion, which suggests a dependency of ΔH_{a} (=ΔH_{m}) on the non-stoichiometry δ and therefore on $\left[\mathrm{V}_{\mathrm{O}}^{\bullet\bullet}\right]$ of the reduced samples. This is attributed to the lattice expansion of the ceria crystal upon reduction.

The calculation of ΔH_a for non-equilibrium oxygen diffusivity of 10 at-% Zr-doped ceria in the low temperature region $400\ °C \leq T \leq 800\ °C$ yields in comparison an increased value despite the high oxygen vacancy concentration of the solid. Regarding this finding, a dopant-induced migration barrier enhancement in Zr-doped ceria is discussed.

The calculated activation enthalpies ΔH_a (= ΔH_m) for chemical oxygen diffusion for trivalent-doped and nominally undoped ceria differ by 0.41 eV and 0.29 eV, respectively, which is not the case for oxygen tracer diffusion. Here, the effects of the high oxygen vacancy concentrations on the bulk transport properties are discussed.

The calculation of the apparent overall activation enthalpy of the $\tilde{K}_O$ data is based on the oxygen isotope exchange experiments utilizing $C^{18}O_2$ in the temperature range $300\ °C \leq T \leq 800\ °C$. Concerning the increased value of $\Delta H_a^{\tilde{K}_O}$ for the Zr-doped ceria, which is not indicated by the oxygen tracer surface exchange data, reported findings on surface alteration effects under low oxygen partial pressure and high temperatures can explain the observed differences.

A comparison can be made to $\tilde{K}_O$ data obtained in the true surface exchange controlled kinetic regime, as the $\tilde{K}/\tilde{D}$ ratios of this work suggest a diffusion controlled or mixed kinetic regime at $T \leq 800\ °C$. The influence of the kinetic regime on the apparent activation enthalpy of the surface exchange coefficient is considered. If measured in the mixed regime and in the diffusion controlled kinetic regime, K_O depends not only on the equilibrium oxygen exchange rate but also on the oxygen diffusion coefficient D_O in the bulk. The determined apparent $\Delta H_a^{\tilde{K}_O}$ is the mean value of the individual activation enthalpies $\Delta H_a^{\tilde{D}_O}$ and $\Delta H_a^{\mathfrak{R}_O^0}$. According to this theory $\Delta H_a^{\mathfrak{R}_O^0}$ can be estimated by the relation $\Delta H_a^{\mathfrak{R}_O^0} = 2\Delta H_a^{\tilde{K}_O} - \Delta H_a^{\tilde{D}_O} \approx 0.5\ \text{eV}$.

7.2 Overall conclusions

Within the framework of the objectives of this thesis the following overall conclusions can be drawn, based on the results discussed above. The experimental work shows promising results regarding CO_2 splitting with trivalent-doped ceria, especially Sm-doped ceria, at lower temperatures than suggested for the low-temperature splitting/re-oxidation step conditions. Several findings indicate a positive influence of doping ceria with trivalent dopants, especially Sm:

1. The majority of isotope exchange experiments under the various experimental conditions show enhanced values of D_O and K_O for 10 at-% Sm-doped cerium dioxide, in comparison to 10 at-% Y-doped and Zr-doped as well as nominally undoped ceria.

2. For the determinable apparent activation energies, the values for 10 at-% Sm-doped ceria are lowest.

3. 10 at-% Sm-doped and Y-doped ceria samples tend to reach the surface exchange controlled kinetic regime at $T \geq 700$ °C, which is attributed to the fact that the trivalent dopant increases the concentration of oxygen vacancies, and hence the diffusivity of oxygen in comparison to the 10 at-% Zr-doped and nominally undoped ceria samples.

4. Trivalent-doped ceria has a higher fraction of isolated defects at a certain non-stoichiometry. The tendency of undoped ceria to form defect complexes, changing the ratio of defect complexes to isolated defects, is detrimental to the ionic transport.

Considering the investigations of non-equilibrium surface exchange and bulk diffusion of oxygen with $C^{18}O_2$ gas atmosphere, a temperature of $T = 500$ °C for STCC is actually feasible, due to the weak temperature dependency of the parameters $\tilde{K}_O$ and $\tilde{D}_O$. As discussed in section 2.1, a decrease of the temperature for both the reduction and the re-oxidation step results, e.g., in the decrease of radiation losses of the optical solar concentration system as well as in a reduction of the thermal load of the redox material, this is critical with regard to the materials stability during long-term cycling. Further, at lower oxidation temperatures the total theoretical efficiency of the process is higher, too [Lang15]. Higher reduction extents δ are therefore necessary, given constant reaction conditions. An investigation of the optimal oxygen vacancy concentration of the redox material, e.g., Sm-doped ceria, with systematic variation of the oxygen non-stoichiometry in the reduction step, is suggested.

Using Zr-doped cerium oxide, on the other hand, shows various negative aspects. Zr-doping of ceria enhances the reducibility, but Zr-based surface alteration effects under low oxygen partial pressure and high temperatures and dopant-vacancy interaction induced migration barrier enhancement in Zr-doped ceria are detrimental for surface exchange and oxygen diffusion at lower temperatures of $T \leq 800$ °C. Zr-doped ceria that is slightly different in its composition and surface structure might induce significant differences in oxygen surface exchange. Very harsh reduction conditions should be avoided for the $(Ce,Zr)O_{2-\delta}$ redox system.

Bibliography

[Aban06] Abanades, S.; Flamant, G. Thermochemical hydrogen production from a two-step solar-driven water-splitting cycle based on cerium oxides. *Solar Energy* 80, **2006**, 1611-1623.

[Aban10] Abanades, S.; Legal, A.; Cordier, A.; Peraudeau, G.; Flamant, G.; Julbe, A. Investigation of reactive cerium-based oxides for H2 production by thermochemical two-step water-splitting. *J. Mater. Sci* 45, **2010**, 4163-4173.

[Acke14a] Ackermann, S.; Scheffe, J.R.; Steinfeld, A. Diffusion of Oxygen in Ceria at Elevated Temperatures and Its Application to H_2O/CO_2 Splitting Thermochemical Redox Cycles. *J. Phys. Chem. C* 118, **2014**, 5216-5225.

[Acke14b] Ackermann, S.; Scheffe, J.R.; Duss, J.; Steinfeld, A. Morphological Characterization and Effective Thermal Conductivity of Dual-Scale Reticulated Porous Structures. *Materials* 7, **2014**, 7173-7195.

[Acke15] Ackermann, S.; Sauvin, L.; Castiglioni, R.; Rupp, J.L.M.; Scheffe, J.R.; Steinfeld, A. Kinetics of CO_2 Reduction over Nonstoichiometric Ceria. *J. Phys. Chem. C* 119, **2015**, 16452-16461.

[Adle93a] Adler, S.B.; Smith, J.W., Reimer; J.A. Dynamic Monte Carlo simulation of spin-lattice relaxation of quadrupolar nuclei in solids. Oxygen-17 in yttria-doped ceria. *J. Chem. Phys.* 98, 9, **1993**, 7613-7620.

[Adle93b] Adler, S.B.; Smith, J.W. Effects of long-range forces on oxygen transport in yttria-doped ceria: Simulation and theory. *J. Chem. Soc. Faraday Trans.* 89, 16, **1993**, 3123-3128.

[Alle08] Allendorf, M.D.; Diver, R.B.; Siegel, N.P.; Miller, J.E. Two-Step Water Splitting Using Mixed-Metal Ferrites: Thermodynamic Analysis and Characterization of Synthesized Materials. *Energy Fuels* 22, **2008**, 4115-4124.

[Anan16] Ananyev, M.V.; Tropin, E.S.; Eremin, V.A.; Farlenkov, A.S.; Smirnov, A.S., Kolchugin, A.A.; Porotnikova, N.M.; Khodimchuk, A.V.; Berenov, A.V.; Kurumchin, E.Kh. Oxygen isotope exchange in $La_2NiO_{4\pm\delta}$. *Phys. Chem. Chem. Phys.* 18, **2016**, 9102-9111.

[Ando83] Ando, K.; Oishi, Y. Diffusion Characteristics of Actinide Oxides. *J. Nucl. Sci. Technol.* 20, **1983**, 973-982.

[Appe98] Appel, L.G.; Eon, J.G.; Schmal, M. The CO_2-CeO_2 interaction and its role in the CeO_2 reactivity. *Catalysis Letters* 56, **1998**, 199-202.

[Arms11] Armstrong, E.N.; Duncan, K.L.; Oh, D.J.; Weaver, J.F.; Wachsman, E.D. Determination of surface exchange coefficients of LSM, LSCF, YSZ, GDC constituent materials in composite SOFC cathodes. *Journal of The Electrochemical Society* 158, 5, **2011**, B492-B499.

[Arms13] Armstrong, E.N.; Duncan, K.L.; Wachsman, E.D. Effect of A and B-site cations on surface exchange coefficient for ABO3 perovskite materials. *Phys. Chem. Chem. Phys.* 15, **2013**, 2298-2308.

[Bald00] Balducci, G.; Saiful Islam, M.; Kaspar, J.; Fornasiero, P.; Graziani, M. Bulk reduction and oxygen migration in the ceria-based oxides. *Chem. Mater.* 12, **2000**, 677-681.

[Bald97] Balducci, G.; Kaspar, J.; Fornasiero, P.; Graziani, M. Computer simulation studies of bulk reduction and oxygen migration in CeO_2-ZrO_2 solid solutions. *J. Phys. Chem. B* 101, **1997**, 1750-1753.

[Ban72] Ban, Y.; Nowick, A.S. Defects and mass transport in reduced CeO_2 single chrystals. National Bureau of Standards Special Publication 364, Solid State Chemistry, Proceedings of 5th Materials Research Symposium, 1972.

[Bayo84] Bayoglu, A.; Lorenzelli, R. Oxygen diffusion in f.c.c. fluorite nonstoichiometric nuclear oxides $MO_{2\pm x}$. *Solid State Ionics* 12, **1984**, 53-66.

[Bell69] Belle, J. Oxygen and uranium diffusion in uranium dioxide (a review). *J. Nucl. Mater.* 30, **1969**, 3-15.

[Beva64] Bevan, D.J.M.; Kordis, J. Mixed oxides of the type MO_2 (fluorite)-M_2O_3-I. Oxygen dissociation pressures and phase relationships in the system CeO_2-Ce_2O_3 at high temperatures. *J. Inorg. Nucl. Chem.* 26, **1964**, 1509-1523.

[Bhos19] Bhosale, R.R.; Takalkar, G.; Sutar, P.; Kumar, A.; AlMomani, F.; Khraisheh, M. A decade of ceria based solar thermochemical H_2O/CO_2 splitting cycle. *International Journal of Hydrogen Energy* 44, **2019**, 34-60.

[Bine99] Binet, C; Daturi, M.; Lavalley, J.-C. IR study of polycrystalline ceria properties in oxidized and reduced states. *Catalysis Today* 50, **1999**, 207-225.

[Bish09a] Bishop, S.R.; Duncan, K.L.; Wachsman, E.D. Defect equilibria and chemical expansion in nonstoichiometric undoped and gadolinium-doped cerium oxide. *Electrochimia Acta* 54, **2009**, 1436-1443.

[Bish09b] Bishop, S.R.; Duncan, K.L.; Wachsman, E.D. Surface and bulk oxygen non-stoichiometry and bulk expansion in gadolinium-doped cerium oxide. *Acta Materialia* 57, **2009**, 3596-3605.

[Blai15] Blair, J.; Mebane, D.S. A Bayesian approach to electrical conductivity relaxation and isotope exchange/secondary ion mass spectrometry. *Solid State Ionics* 270, **2015**, 47-53.

[Blum71] Blumenthal, R.N.; Lee, P.W.; Panlener, R.J. Studies on the Defect Structure on Nonstoichiometric Cerium Dioxide. *J. Electrochemic. Soc.* 118, **1971**, 123-129.

[Buen08] Bueno-López, A.; Krishna, K.; Makkee, M. Oxygen exchange mechanism between isotopic CO_2 and Pt/CeO_2. *Appl. Catal. A General* 342, **2008**, 144-149.

[Bulf16] Bulfin, B.; Hoffmann, L.; de Oliveira, L.; Knoblauch, N.; Call, F.; Roeb, M.; Sattler, Ch.; Schmücker, M. Statistical thermodynamics of nonstoichiometric ceria and ceria zirconia solid solutions. *Phys. Chem. Chem. Phys.* 18, **2016**, 23147-23154.

[Butl83] Butler, V.; Catlow, C.R.A.; Fender, B.E.F.; Harding, J.H. Dopant ion radius and ionic conductivity in cerium dioxide. *Solid State Ionics* 8, **1983**, 109-113.

[Cale84] Cales, B.; Baumard, J.F. Transport Properties and Defect Structure of Nonstoichiometric Yttria Doped Ceria. *J. Phys. Chem. Solids* 45, 8/9, **1984**, 929-935.

[Call13] Call, F.; Roeb, M.; Schmücker, M.; Bru, H.; Curulla-Ferre, D.; Sattler, Ch.; Pitz-Paal, R. Thermogravimetric Analysis of Zirconia-Doped Ceria for Thermochemical Production of Solar Fuel. *American Journal of Analytical Chemistry* 4, **2013**, 37-45.

[Call15] Call, F.; Roeb, M.; Schmücker, M.; Sattler, Ch.; Pitz-Paal, R. Ceria Doped with Zirconium and Lanthanide Oxides to Enhance Solar Thermochemical Production of Fuels. *J. Phys. Chem. C* 119, **2015**, 6929-6938.

[Chat92] Chater, R.J.; Carter, S.; Kilner, J.A.; Steele, B.C.H. Development of a novel SIMS technique for oxygen self-diffusion and surface exchange coefficient measurements in oxides of high diffusivity. *Solid State Ionics.* 53–56, **1992**, 859–867

[Chen13] Cheng, Z.; Sherman, B.J.; Lo, C.S. Carbon dioxide activation and dissociation on ceria(110): A density functional theory study. *J. Chem. Phys.* 138, **2013**, 014702-014714.

[Chue09] Chueh, W.C.; Haile, S.M. Ceria as a thermochemical reaction medium for selectively generating syngas or methane from H_2O and CO_2. *ChemSusChem* 2, **2009**, 735-739.

[Chue10a] Chueh, W.C.; Falter, C.; Abbott, M.; Scipio, D.; Furler, P.; Haile, S.M.; Steinfeld, A. High-flux solar-driven thermochemical dissociation of CO_2 and H_2O using nonstoichiometric ceria. *Science* 330, **2010**, 1797-1801.

[Chue10b] Chueh, W.C.; Haile, S.M. A thermochemical study of ceria: exploiting an old material for new modes of energy conversion and CO_2 mitigation. *Phil. Trans. R. Soc. A* 368, **2010**, 3269-3294.

[Chue12a] Chueh, W.C.; Haile, S.M. Electrochemistry of mixed oxygen ion and electron conducting electrodes in solid electrolyte cells. *Annu. Rev. Chem. Biomol. Eng. 3*, **2012**, 313-341.

[Chue12b] Chueh, W.C.; McDaniel, A.H.; Grass, M.E.; Hao, Y.; Jabeen, N.; Liu, Z.; Haile, S.M.; McCarty, K.F.; Bluhm, H.; El Gabaly, F. Highly Enhanced Concentration and Stability of Reactive Ce^{3+} on Doped CeO_2 Surface Revealed In Operando. *Chem. Mater. 24*, **2012**, 1876–1882.

[Clau00] Claus, J.; Leonhardt, M.; Maier, J. Tracer diffusion and chemical diffusion of oxygen in acceptor doped $SrTiO_3$. J. *Phys. Chem. Solids 61*, **2000**, 1199-1207.

[Cost05] Costa-Nunes, O.; Gorte, R.J.; Vohs, J.M. High mobility of ceria films on zirconia at moderate temperatures. *J. Mater. Chem.* 15, **2005**, 1520-1522.

[Cran75] Crank, J. The Mathematics of Diffusion. Oxford University Press, 1975.

[Dave16] Davenport, T.C.; Yang, C.-K.; Kucharczyk, C.J.; Ignatowich, M.J.; Haile, S.M. Implications of Exceptional Material Kinetics on Thermochemical Fuel Production Rates. *Energy Technol.* 4, **2016**, 764-770.

[Delg13] Delgado, J.J.; del Rio, E.; Chen, X.; Blanco, G.; Pintado, J.M.; Bernal, S.; Calvino, J.J. Understanding ceria-based catalytic materials: An overview of recent progress. In Trovarelli, A., Fornasiero, P.: Catalysis by Ceria and Related Materials. Second Edition, Imperial College Press, 2013.

[DeSo06] De Souza, R.A. A universal empirical expression for the isotope surface exchange coefficients (k*) of acceptor-doped perovskite and fluorite oxides. *Phys. Chem. Chem. Phys.* 8, **2006**, 890-897.

[Dikm98] Dikmen, S.; Shuk, P.; Greenblatt, M. Hydrothermal synthesis and properties of $Ce_{1-x}Bi_xO_{2-\delta}$ solid solutions. *Solid State Ionics* 112, **1998**, 299-307.

[Dunc06] Duncan, K.L.; Wang, Y.; Bishop, S.R.; Ebrahimi, F.; Wachsman, E.D. The role of point defects in the physical properties of nonstoichiometric ceria. *J. Appl. Phys.* 101, **2007**, 044906-044912.

[Eguc92] Eguchi, K.; Setoguchi, T.; Inoue, T.; Arai, H. Electrical properties of ceria-based oxides and their application to solid oxide fuel cells. *Solid State Ionics* 52, **1992**, 165-172.

[Eufi14] Eufinger, J.-P.; Daniels, M.; Schmale, K.; Berendts, S.; Ulbrich, G.; Lerch, M.; wiemhöfer, H.-D.; Janek, J. The model case of an oxygen storage catalyst – non-stoichiometry, point defects and electrical conductivity of single crystalline CeO_2-ZrO_2-Y_2O_3 solid solutions. *Phys. Chem. Chem. Phys.* 16, **2014**, 25583-25600.

[Fabe89] Faber, J.; Geoffroy, C.; Roux, A.; Sylvestre, A.; Abelard, P. A systematic incestigation of the dc electrical conductivity of rare-earth doped ceria. *Appl. Phys. A* 49, **1989**, 225-232.

[Fabe89] Faber, J.; Geoffroy, C.; Roux, A.; Sylystre, A.; Abelard, P. A systematic investigations of the dc electrical conductivity or rare-earth doped ceria. *Appl. Phys. A*: *Solids Surf. 49*, **1989**, 225-232.

[Feng14] Feng, Z.A.; Gabaly, F.E.; Ye, X.; Shen, Z.-X.; Chueh, W.C. Fast vacancy-mediated oxygen ion incorporation across the ceria-gas electrochemical interface. *Nat. Commun. 5*, **2014**, 4374-4382.

[Feng15] Feng, Z.; Machala, M.L.; Chueh, W.C. Surface electrochemistry of CO_2 reduction and CO oxidation on Sm-doped CeO_{2-x}: Coupling between Ce^{3+} and carbonate adsorbates. *Phys. Chem. Chem. Phys.* 17, **2015**, 12273-12281.

[Fiel01] Fielitz, P.; Borchardt, G. On the accurate measurement of oxygen self-diffusivities and surface exchange coefficients in oxides via SIMS depth profiling, *Solid State Ionics* 144, **2001**, 71-80

[Fiel16] Fielitz, P.; Borchardt, G. Oxygen exchange at gas/solid interfaces: how the apparent activation energy of the surface exchange coefficient depends on the kinetic regime. *Phys. Chem. Chem. Phys.* 18, **2016**, 22031-22038.

[Fisc12] Fischer, E., Hertz, J.L. Measurability of the diffusion and surface exchange coefficients using isotope exchange with thin film and traditional samples. *Solid State Ionics* 218, **2012**, 18-24.

[Floy73] Floyd, J.M. Interpretation of transport phenomena in non-stoichiometric ceria. *Indian J. Technol.* 11, **1973**, 589-594.

[Forn96] Fornasiero, P., Balducci, G.; Di Monte, R.; Kaspar, J.; Sergo, V.; Gubitosa, G.; Ferrero, A.; Graziani, M. Modification of the Redox Behaviour of CeO_2 Induced by Structural Doping with ZrO_2. *Journal of Catalysis* 164, **1996**, 173-183.

[Fu10] Fu, Y.-P.; Chen, S.-H.; Huang, J.-J. Preparation and characterization of $Ce_{0.8}M_{0.2}O_2$ (M = Y, Gd, Sm, Nd, La) solid electrolyte materials for solid oxide fuel cells. *International Journal of Hydrogen Energy* 35, 2, **2010**, 745-752.

[Furl12] Furler, P.; Scheffe, J.R.; Steinfeld, A. Syngas production by simultaneous splitting of H_2O and CO_2 via ceria redox reactions in a high-temperature solar reactor. *Energy and Environmental Science* 5, **2012**, 6098-6103.

[Gries14] Grieshammer, S.; Grope, B.O.H.; Koettgen, J.; Martin, M. A combined DFT + U and Monte Carlo study on rare earth doped ceria. *Phys. Chem Chem. Phys.* 16, **2014**, 9974-9986.

[Gries16] Grieshammer, S.; Nakayama, M.; Martin, M. Association of defects in doped non-stoichiometric ceria from first principles. *Phys. Chem. Chem. Phys.* 18, **2016**, 3804-3811.

[Gries17a] Grieshammer, S.; Martin, M. Influence of defect interactions on the free energy of reduction in pure and doped ceria. *J. Mater. Chem. A* 5, **2017**, 9241-9249.

[Gries17b] Grieshammer, S. Defect Interactions in the CeO_2-ZrO_2-Y_2O_3 Solid Solution. *J. Phys. Chem. C* 121, **2017**, 15078-15084.

[Gries18] Grieshammer, S.; Eisele, S.; Koettgen, J. Modeling Oxygen Ion Migration in the CeO_2-ZrO_2-Y_2O_3 Solid Solution. *J. Phys. Chem. C* 122, **2018**, 18809-18817.

[Gron61] Grone, A.R. Current-induced marker motion in copper. *J. Phys. Chem. Solids* 20, **1961**, 88-93.

[Grop12] Grope, B.O.H.; Zacherle, T.; Nakayama, M.; Martin, M. Oxygen conductivity of doped ceria: A Kinetic Monte Carlo study. *Solid State Ionics* 225, **2012**, 476-483.

[Gros13] Gross, J. H. Massenspektrometrie. Springer, 2013

[Hahn13] Hahn, K.R.; Iannuzzi, M.; Seitsonen, A.P.; Hutter, J. Coverage Effect of the CO_2 Adsorption Mechanisms on $CeO_2(111)$ by First Principles Analysis. *J. Phys. Chem. C* 117, **2013**, 1701-1711.

[Hao14] Hao, Y.; Yang, C.-K.; Haile, S.M. Ceria-Zirconia Solid Solutions ($Ce_{1-x}Zr_xO_{2-\delta}$, $x \leq 0.2$) for Solar Thermochemical Water Splitting: A Thermodynamic Study. *Chem. Mater.* 26, **2014**, 6073-6082.

[Harr06] Harrison, W.E. The Role of Fischer Tropsch Fuels for the US Military. OSD Assured Fuels Initiative Report, 2006.

[Haus12] Haussener, S.; Steinfeld, A. Effective heat and mass transport properties of anisotropic porous ceria for solar thermochemical fuel generation. *Materials* 5, **2012**, 192-209.

[Heid14] van der Heide, P. Secondary Ion Mass Spectrometry. An Introduction to Principles and Practices. Wiley, 2014

[Hide00] Hayashi, H.; Sagawa, R.; Inaba, H.; Kawamura, K. Molecular dynamics calculations on ceria-based solid electrolytes with different radius dopants. *Solid State Ionics* 131, **2000**, 281-290.

[Hide99] Inaba, H.; Sagawa, R.; Hayashi, H.; Kawamura, K. Molecular dynamics simulation of gadolinia-doped ceria. *Solid State Ionics* 122, **1999**, 95-103.

[Hohn81] Hohnke, D.K. Ionic conduction in doped oxides with the fluorite structure. *Solid State Ionics* 5, **1981**, 531-534.

[Hook13] Höök, M.; Tang, X. Depletion of fossil fuels and anthropogenic climate change - A review. *Energy Policy* 52, **2013**, 797-809.

[Huan97] Huang, W.; Shuk, P.; Greenblatt, M. Hydrothermal synthesis and properties of $Ce_{1-x}Sm_xO2-_{x/2}$ and $Ce_{1-x}Ca_xO_{2-x}$ solid solutions. *Chem. Mater.* 9, **1997**, 2240-2245.

[Hunt61] Huntington, H.B.; Grone, A.R. Current-induced marker motion in gold wires. *J. Phys. Chem. Solids* 20, **1961**, 76-87.

[Janv98] Janvier, C.; Pijolat, M.; Valdivieso, F.; Soustelle, M.; Zing, C. Thermal stability of $Ce_{1-x}Zr_xO_2$ solid solution powders. *Journal of the European Ceramic Society* 18, 9, **1998**, 1331-1337.

[Jian14] Jiang, Q.; Zhou, G.; Jiang, Z.; Li, C. Thermochemical CO_2 splitting reaction with $Ce_xM_{1-x}O_{2-\delta}$ (M = Ti^{4+}, Sn^{4+}, Hf^{4+}, Zr^{4+}, La^{3+}, Y^{3+} and Sm^{3+}) solid solutions. *Sol. Energy* 99, **2014**, 55-66.

[Kami00] Kamiya, M.; Shimada, E.; Ikuma, Y.; Komatsu, M.; Haneda, H. Intrinsic and extrinsic oxygen diffusion and surface exchange reaction in cerium oxide. *J. Electrochem. Soc.* 147, 3, **2000**, 1222-1227.

[Kami98] Kamiya, M.; Shimada E.; Ikuma, Y. Oxygen self-diffusion in cerium oxide. *J. Ceram. Soc. Japan* 106, **1998**, 1023-1026.

[Kane07] Kaneko, H.; Miura, T.; Ishihara, H.; Taku, S.; Yokoyama, T.; Nakajima, H.; Tamaura, Y. Reactive ceramics of CeO_2–MO_x (M = Mn, Fe, Ni, Cu) for H_2 generation by two-step water splitting using concentrated solar thermal energy. *Energy* 32, **2007**, 656-663.

[Kane08] Kaneko, H.; Ishihara, H.; Taku, S.; Naganuma, Y.; Hasegawa, N.; Tamaura, Y. Cerium ion redox system in CeO_2-xFe_2O_3 solid solution at high temperatures (1273-1673 K) in the two-step water-splitting reaction for solar H_2 generation. *J. Mater. Sci.* 43, **2008**, 3153-3161.

[Kasp99] Kaspar, J.; Fornasiero, P.; Graziani, M. Use of CeO_2-based oxides in the three-way catalysis. *Catalysis Today* 50, 2, **1999**, 285-298.

[Kill62] Killoran, D.R. The Effective Duration of a Linear Slow-Cool. *J. Electrochem. Soc.* 109, **1962**, 170-171.

[Kiln11] Kilner, J.A.; Skinner, S.J.; Brongersma, H.H. The isotope exchange depth profiling (IEDP) technique using SIMS and LEIS. *J. Solid State Electrochem.* 15, **2011**, 861-876.

[Kiln82] Kilner, J.A.; Waters, C.D. The effects of dopant cation-oxygen vacancy complexes on the anion transport properties of non-stoichiometric fluorite oxides. *Solid State Ionics* 6, **1982**, 253-259.

[Kiln84] Kilner, J.A.; Steele, B.C.H. Oxygen self-diffusion studies using negative-ion secondary ion mass spectrometry (SIMS). *Solid State Ionics* 12, **1984**, 89–97

[Kiln96a] Kilner, J.A.; De Souza, R.A., in: Poulsen, F.W.: Bonanos, N.; Linderoth, S.; Mogensen, M.; Zachau-Christiansen, B. (Eds.): Proceedings of the 17th Riso International Symposium on Materials Science: High Temperature Electrochemistry: Ceramics and Metals, 1996, 41.

[Kiln96b] Kilner, J.A.; De Souza, R.A.; Fullarton, I.C. Surface exchange of oxygen in mixed conducting perovskite oxides. *Solid State Ionics* 86-88, **1996**, 703-709.

[Kim06] Kim, T.; Vohs, J.M.; Gorte, R.J. Thermodynamic Investigation of the Redox Properties of Ceria-Zirconia Solid Solutions. *Ind. Eng. Chem. Res.* 45, **2006**, 5561-5565.

[Kim89] Kim, D.-J. Lattice Parameters, Ionic Conductivities and Solubility Limits in Fluorite-Structure MO_2 Oxide ($M = Hf^{4+}$, Zr^{4+}, Ce^{4+}, Th^{4+}, U^{4+}) Solid Solutions. *Journal of the American Ceramic Society* 72, 8, **1989**, 1415-1421.

[Knob15] Knoblauch, N.; Dörrer, L.; Fielitz, P.; Schmücker, M.; Borchardt, G. Surface controlled reduction kinetics of nominally undoped polycrystalline CeO_2. *Phys. Chem. Chem. Phys.* 17, **2015**, 5849-5860.

[Knob17] Knoblauch, N.; Simon, H.; Dörrer, L.; Uxa, D.; Fielitz, P.; Wendelstorf, J.; Spitzer, K.-H.; Schmücker, M.; Borchardt, G. Ceria: Recent Results on Dopant-Induced Surface Phenomena. *Inorganics* 5, **2017**, 76.

[Koep16] Koepf, E.; Villasmil, W.; Meier, A. Pilot-scale solar reactor operation and characterization for fuel production via the Zn/ZnO thermochemical cycle. *Appl. Energy* 165, **2016**, 1004-1023.

[Koet17] Koettgen, J.; Zacherle, T.; Grieshammer, S.; Martin, M. Ab initio calculation of the attempt frequency of oxygen diffusion in pure and samarium doped ceria. *Phys. Chem. Chem. Phys.* 19, **2017**, 9957-9973.

[Koet18] Koettgen, J.; Grieshammer, S.; Hein, P.; Grope, B.O.H.; Nakayama, M.; Martin, M. Understanding the ionic conductivity maximum in doped ceria: trapping and blocking. *Phys. Chem. Chem. Phys.* 20, **2018**, 14291-14321.

[Kroe56] Kroeger, F.; Vink, H. In: Solid State Physics. Vol.3, Academic Press, 1956, 307-435.

[Kuhn13] Kuhn, M.; Bishop, S.R.; Rupp, J.L.M.; Tuller, H.L. Structural characterization and oxygen non-stoichiometry of ceria-zirconia ($Ce_{1-x}Zr_xO_{2-\delta}$) solid solutions. *Acta. Mat.* 61, **2013**, 4277-4288.

[Kuma16] Kumari, N.; Ali Haider, M.; Agarwal, M.; Sinha, N.; Basu, S.: Role of reduced CeO_2 (110) surface for CO_2 reduction to CO and methanol. *J. Phys. Chem. C* 120, **2016**, 16626-16635.

[Laar91] Laachir, A.; Perrichon, V.; Badri, A.; Lamotte, J.; Catherine, E.; Lavalley, J.C.; El Fallah, J.; Hilaire, L.; Normand, F.; Quemere, E.; Sauvion, G.N.; Touret, O.: Reduction of CeO2 by hydrogen. Magnetic susceptibility and Fourier-transform infrared ultraviolet and X-ray photoelectron spectroscopy measurements. *J. Chem. Soc. Faraday Trans.* 87, **1991**, 1601-1609.

[Lang16] Lange, M.; Roeb, M.; Sattler, Ch.; Pitz-Paal, R. Entropy Analysis of Solar Two-Step Thermochemical Cycles for Water and Carbon Dioxide Splitting. *Entropy* 18, **2016**, 24.

[LeGa11] Le Gal, A.; Abanades, S. CO_2 and H_2O Splitting for Thermochemical Production of Solar Fuels Using Nonstoichiometric Ceria and Ceria/Zirconia Solid Solutions. *Energy Fuels* 25, **2011**, 4836-4845.

[LeGa12] Le Gal, A.; Abanades, S. Dopant Incorporation in Ceria for Enhanced Water-Splitting Activity during Solar Thermochemical Hydrogen Generation. *J. Phys. Chem.C* 116, **2012**, 13516-13523.

[LeGa13] Le Gal, A.; Abanades, S.; Bion, N.; Le Mercier, T.; Harle, V. Reactivity of Doped Ceria-Based Mixed Oxides for Solar Thermochemical Hydrogen Generation via Two-Step Water-Splitting Cycles. *Energy Fuels* 27, **2013**, 6068-6078.

[Leon02] Leonhardt, M.; De Souza, R.A.; Claus, J.; Maier, J. Surface kinetics of oxygen incorporation into $SrTiO_3$. *Journal of The Electrochemical Society* 149, 2, **2002**, J19-J26.

[Lich12] Lichty, P.; Liang, X.; Muhich, Ch.; Evanko, B.; Bingham, C.; Weimer, A.W. Atomic layer deposited thin film metal oxides for fuel production in a solar cavity reactor. *Int. J. Hydrogen Energy* 37, **2012**, 16888-16894.

[Lykh10] Lykhach, Y.; Staudt, T.; Streber, R.; Lorenz, M.P.A.; Bayer, A.; Steinrück, H.-P.; Libuda, J. CO_2 activation on single crystal based ceria and magnesia/ceria model catalysts. *Eur. Phys. J. B* 75, **2010**, 89-100.

[Maha11] Mahato, N.; Gupta, A.; Balani, K. Doped Zirconia and Ceria-based Electrolytes for Solid Oxide Fuel Cells: A Review. *Nanomaterials and Energy* 1, 1, **2011**, 27-45.

[Maie00] Maier, J. Interaction of oxygen with oxides: How to interpret measured effective rate constants? *Solid State Ionics* 135, **2000**, 575-588.

[Maie04] Maier, J. Physical Chemistry of Ionic Materials: Ions and Electrons in Solids. John Wiley, 2004.

[Mann68] Manning, J.R. Diffusion Kinetics for Atoms in Crystals. D. Van Nostrand Company, Inc., 1968.

[Mann97] Manning, P.S.; Sirman, J.D.; Kilner, J.A. Oxygen self-diffusion and surface exchange studies of oxide electrolytes having he fluorite structure. *Solid State Ionics* 93, **1997**, 125-132.

[Mart06] Martin, M.: On the ionic conductivity of strongly acceptor doped, fluorite-type oxygen ion conductors. J. Electroceram. 17, 2006, 765-773.

[Marx15] Marxer, D.; Furler, Ph.; Scheffe, J.; Geerlings, H.; Falter, Ch.; Batteiger, V.; Sizmann, A.; Steinfeld, A. Demonstration of the Entire Production Chain to Renewable Kerosene via Thermochemical Splitting of H_2O and CO_2. *Energy Fuels* 29, **2015**, 3241-3250.

[Matz69] Matzke, H.J. On uranium self-diffusion in UO_2 and UO_{2+x}. *J. Nucl. Mater.* 30, **1969**, 26-35.

[Matz83] Matzke, H.J. Diffusion processes and surface effects in non-stoichiometry nuclear fuel oxides UO_{2+x} and $(U, Pu)O_{2\pm x}$. *J. Nucl. Mater.* 114, **1983**, 121-135.

[Matz87] Matzke, H.J. Atomic Transport Properties in UO_2 and mixed Oxides $(U, Pu)O_2$. *J. Chem,. Soc., Faraday Trans.* 2, 83, **1987**, 1121-1142.

[Maza94] Mazanec, T.J. Prospects for ceramic electrochemical reactors in industry. *Solid State Ionics* 70/71, **1994**, 11-19.

[McDa13] McDaniel, A.H.; Ambrosini, A.; Coker, E.N.; Miller, J.E.; Chueh, W.C.; O´Hayre, R.; Tong, J. Nonstoichiometric perovskite oxides for solar thermochemical H_2 and CO production. *Energy Procedia* 49, **2013**, 2009-2018.

[McPh06] McPhail, D. S. Applications of Secondary Ion Mass Spectrometry (SIMS) in Material Science. *J. of Mat. Sc.* 41, **2006**, 873-903

[Mehr07] Mehrer, H. Diffusion in Solids. Fundamentals, Methods, Materials, Diffusion-Controlled Processes. Springer, 2007.

[Meng11] Meng, Q.-L.; Lee, C.-i.; Ishihara, T.; Kaneko, H.; Tamaura, Y. Reactivity of CeO_2-based ceramics for solar hydrogen production via a two-step water splitting cycle with concentrated solar energy. *Int. J. Hydrogen Energy* 36, **2011**, 13435-13441.

[Meng12] Meng, Q.-L.; Lee, C.-i.; Shigeta, S.; Kaneko, H.; Tamaura, Y. Solar hydrogen production using $Ce_{1-x}Li_xO_{2-\delta}$ solid solutions via a thermochemical two-step water splitting cycle. *J. Solid State Chem.* 194, **2012**, 343-351.

[Merk08] Merkle, R.; Maier, J. How is oxygen incorporated into oxides? A comprehensive kinetic study of a simple solid-state reaction with $SrTiO_3$ as a model material. *Angew. Chem. Int. Ed.* 47, **2008**, 3874-3894.

[Meye97] Meyer M.; Nicoloso, N.; Jaenisch, V. Percolation model for the anomalous conductivity of fluorite-related oxides. *Physical Review B* 56, 10, **1997**, 5961-5966.

[Mill84] Millot, F.; De Mierry, P. A new method for the study of chemical diffusion in oxides with application to cerium oxide CeO_{2-x}. *J. Phys. Chem. Solids* 46, 7, **1985**, 797-801.

[Moge00] Mogensen, M.; Sammes, N.M.; Tompsett, G.A. Physical, chemical and electrochemical properties of pure and doped ceria. *Solid State Ionics* 129, **2000**, 63-94.

[Muhi17a] Muhich, Ch.; Steinfeld, A. Principles of doping ceria for the solar thermochemical redox splitting of H_2O and CO_2. *J. Mater. Chem. A* 5, **2017**, 15578.

[Muhi17b] Muhich, Ch. Re-Evaluating CeO_2 Expansion Upon Reduction: Noncounterpoised Forces, Not Ionic Radius Effects, Are the Cause. *J. Phys. Chem. C* 121, **2017**, 8052-8059.

[Murr12] Murray, J.; King, D. Climate policy: Oil´s tipping point has passed. *Nature* 481, 7382, **2012**, 433-435.

[Naka09] Nakayama, M.; Martin, M. First-principles study on defect chemistry and migration of oxide ions in ceria doped with rare-earth cations. *Phys. Chem. Chem. Phys.* 11, **2009**, 3241-3249.

[Naka77] Nakamura, T. Hydrogen production from water utilizing solar heat at high temperatures. *Solar Energy* 19, **1977**, 467-475.

[Nama03] Namai, Y.; Fukui, K.-I.; Iwasawa, Y. Atom-Resolved Noncontact Atomic Force Microscopic Observations of CeO_2(111) Surfaces wih Different Oxidation States: Surface Structure and Behavior of Surface Oxygen Atoms. *J. Phys. Chem. B* 107, **2003**, 11666-11673.

[Ni08] Ni, M.; Leung, M.K.; Leung, D.Y. Technological development of hydrogen production by solid oxide electrolyzer cell (SOEC). *International Journal of Hydrogen Energy* 33, 9, **2008**, 2337-2354.

[Paie13] Paier, J.; Penschke, Ch.; Sauer, J. Oxygen defects and surface chemistry of ceria: Quantum chemical studies compared to experiment. *Chem. Rev.* 113, **2013**, 3949-3985.

[Panl75] Panlener, R.J.; Blumenthal, R.N.; Garnier, J.E. A thermodynamic study of nonstoichiometric cerium oxide. *J. Phys. Chem. Solids* 36, **1975**, 1213-1222.

[Pech67] Pechini, M.P. Method of preparing lead and alkaline earth titanates and niobates and coating method using the same to form a capacitor. U.S. Patent 3.330.697, 1967.

[Perr94] Perrichon, V.; Laachir, A.; Bergeret, G.; Frety, R.; Tournayan, L.; Touret, O. Reduction of cerias with different textures by hydrogen and their reoxidation by oxygen. *J. Chem. Soc. Faraday Trans.* 90, **1994**, 773-781.

[Pfau94] Pfau, A.; Schierbaum, K.D. The electronic structure of stoichiometric and reduced CeO_2 surfaces: an XPS, UPS and HREELS study. *Surf. Sci.* 321, **1994**, 71-80.

[Pijo95] Pijolat, M.; Prin, M.; Soustelle, M.; Touret, O.; Nortier, P. Thermal stability of doped ceria: experiment and modelling. *Journal of the Chemical Society* 91, 21, **1995**, 3941-3948.

[Pryd95] Pryde, A.K.A.; Vyas, S.; Grimes, R.W.; Gardner, J.A.; Wang, R. Cadmium and indium defects in ceria and their interaction with oxygen vacancies and small polarons. *Physical Review B* 52, **1995**, 13214-13222.

[Ramo14] Ramos-Fernandez, E.V.; Shiju, N.R.; Rothenberg, G. Understanding the solar-driven reduction of CO_2 on doped ceria. *RSC Adv.* 4, **2014**, 16456-16463.

[Rome07] Romero-Alvarez, M.; Gonzales-Aguilar, J.; Zarza, E. Concentrating solar thermal power. In: Energy efficiency and renewable energy Handbook. CRC Press, 2007.

[Ruiz98] Ruiz-Trejo, E.; Sirman, J.D.; Baikov, Y.M.; Kilner, J.A. Oxygen ion diffusivity, surface exchange and ionic conductivity in single crystal Gadolinia doped Ceria. *Solid State Ionics*, 113-115, **1998**, 565-569.

[Scar15] Scaranto, J.; Idriss, H. The Effect of Uranium Cations on the Redox Properties of CeO_2 Within the Context of Hydrogen Production from Water. *Top. Catal.* 58, **2015**, 143-148.

[Scha19] Schaube, M.; Merkle, R.; Maier, J. Oxygen exchange kinetics on systematically doped ceria: a pulsed isotope exchange study. *J. Mater. Chem. A* 7, **2019**, 21854-21866.

[Scha20] Schaube, M.; Merkle, R.; Maier, J. Interdependence of Point Defects and Reaction Kinetics: CO and CH4 Oxidation on Ceria and Zirconia. *J. Phys. Chem. C* 124, **2020**, 18544-18556.

[Sche12] Scheffe, J.R.; Steinfeld, A. Thermodynamic Analysis of Cerium-Based Oxides for Solar Thermochemical Fuel Production. *Energy Fuels* 26, **2012**, 1928-1936.

[Sche13] Scheffe, J.R.; Jacot, R.; Patzke, G.R.; Steinfeld, A. Synthesis, Characterization, and Thermochemical Redox Performance of Hf^{4+}, Zr^{4+}, and Sc^{3+} Doped Ceria for Splitting CO_2. *J. Phys. Chem. C* 117, **2013**, 24104-24114.

[Scot75] Scott, H.G. Phase relationships in the zirconia-yttria system. *J. Mater. Sci.* 10, **1975**, 1527-1535.

[Sieg13] Siegel, N.P.; Miller, J.E.; Ermanoski, I.; Diver, R.B.; Stechel, E.B. Factors Affecting the Efficiency of Solar Driven Metal Oxide Thermochemical Cycles. *Industrial & Engineering Chemistry Research* 52, 9, **2013**, 3276-3286.

[Smit10] Smith, H.T. Ace in the Hole: Fischer-Tropsch Fuels and National Security. USAWC Program Research Project Report, 2010.

[Sriv74] Srivastava, K.K.; Patil, R.N.; Choudhary, C.B. Revised Phase diagram of the System ZrO_2-$YO_{1.5}$. *Trans. J. Br. Ceram. Soc.* 73, **1974**, 85-91.

[Stau10] Staudt, T.; Lykhach, Y.; Tsud, N.; Skála, T.; Prince, K.C.; Matolín, V.; Libuda, J. Ceria reoxidation by CO_2: A model study. *Journal of Catalysis* 275, **2010**, 181-185.

[Stau11] Staudt, T.; Lykhach, Y.; Tsud, N.; Skála, T.; Prince, K.C.; Matolin, V.; Libuda, J. Electronic structure of magnesia-ceria model catalysts, CO_2 adsorption, and CO_2 activation: A synchrotron radiation photoelectron spectroscopy study. *J. Phys. Chem. C* 115, **2011**, 8716-8724.

[Stei02] Steinfeld, A. Solar hydrogen production via a two-step water-splitting thermochemical cycle based on Zn/ZnO redox reactions. *Int. J. Hydrogen Energy* 27, **2002**, 611-619.

[Stil21] Stilhano Vilas Boas, C.R.; Sturm, J.M.; Milov, I.; Phadke, P.; Bijkerk, F. Room temperature oxygen exchange and diffusion in nanometer-thick ZrO_2 and MoO_3 films. *Applied Surface Science* 550, **2021**, 149384-149392.

[Taka15] Takacs, M.; Scheffe, J.R.; Steinfeld, A. Oxygen non-stoichiometry and thermodynamic characterization of Zr doped ceria in the 1573-1773 K temperature range. *Phys. Chem. Chem. Phys.* 17, **2015**, 7813-7822.

[Taka17] Takacs, M.; Ackermann, S.; Bonk, A.; Neises-von Puttkamer, M.; Haueter, Ph.; Scheffe, J.R.; Vogt, U.F.; Steinfeld, A. Splitting CO_2 with a Ceria-Based Redox Cycle in a Solar-Driven Thermogravimetric Analyzer. *AIChE Journal* 63, 4, **2017**, 1263-1271.

[Tian02] Tianshu, Z.; Hing, P.; Huang, H.; Kilner, J.A.: Ionic conductivity in the CeO_2-Gd_2O_3 system ($0.05 \leq Gd/Ce \leq 0.4$) prepared by oxalate coprecipitation. *Solid State Ionics* 148, **2002**, 567.

[Trov02] Trovarelli, A. Catalysis by Ceria and Related Materials. Imperial College Press, 2002.

[Tull77] Tuller, H.L.; Nowick, A.S. Small polaron electron transport in reduced CeO_2 single crystals. *J. Phys. Chem. Solids* 38, **1977**, 859-867.

[Vida01] Vidal, H.; Kaspar, J.; Pijolat, M.; Colon, G.; Bernal, S.; Cordon, A.; Perrichon, V.; Fally, F. Redox behavior of CeO_2-ZrO_2 mixed oxides: II. Influence of redox treatments on low surface area catalysts. *Applied Catalysis B: Environmental* 30, 1, **2001**, 75-85.

[Wang80] Wang, D.Y.; Nowick, A.S. The “grain-boundary effect” in doped ceria solid electrolytes. *J. Solid State Chem.* 35, **1980**, 325-333.

[Wang81] Wang, D.Y.; Park, D.S.; Griffith, J.; Nowick, A.S. Oxygen-Ion conductivity and defect interactions in yttria-doped ceria. *Solid State Ionics* 2, **1981**. 95-105.

[Wang97] Wang, S.; Inaba, H.; Tagawa, H.; Hashimoto, T. Non-stoichiometry of $Ce_{0.8}Gd_{0.2}O_{1.9-x}$. *J. Electrochem. Soc.* 144, 11, **1997**, 4076-4080.

[Wang98] Wang, S.; Inaba, H.; Tagawa, H.; Dokiya, M.; Hashimoto, T. Non-stoichiometry of $Ce_{0.9}Gd_{0.1}O_{1.95-x}$. *Solid State Ionics* 107, **1998**, 73-79.

[Wang19] Wang, J.; Bishop, S.R.; Sun, L.; Lu, Q.; Vardar, G.; Bliem, R.; Tsvetkov, N.; Crumlin, E.J.; Gallet, J.-J.; Bournel, F.; Waluyo, I.; Yildiz, B. Threshold catalytic onset of carbon formation on CeO_2 during CO_2 electrolysis: mechanism and inhibition. *J. Mater. Chem. A*, 7, **2019**, 15233-15243.

[Yang06] Yang, Z.; Woo, T.K.; Hermansson, K. Effects of Zr doping on stoichiometric and reduced ceria: A first-principles study. *The Journal of Chemical Physics* 124, **2006**, 224704-224710.

[Yang14] Yang, N.; Belianinov, A.; Strelcov, E.; Tebano, A.; Foglietti, V.; Di Castro, D.; Schlueter, Ch.; Lee, T.-L.; Baddorf, A.P.; Balke, N.; Jesse, S.; Kalinin, S.V.; Balestrino, G.; Aruta, C. Effect of Doping on Surface Reactivity and

Conduction Mechanism in Samarium-Doped Ceria Thin Films. *ACS Nano* 8,12, **2014**, 12494-12501.

[Yu14] Yu, Y.; Mao, B.; Geller, A.; Chang, R.; Gaskell, K.; Liu, Z.; Eichhorn, B.W. CO_2 activation and carbonate intermediates: An operando AP-XPS study of CO_2 electrolysis reactions on solid oxide electrochemical cells. *Phys. Chem. Chem. Phys.* 16, **2014**, 11633-11639.

[Yuan15] Yuan, F.; Zhang, Y.; Weber, W.J. Vacancy-vacancy interaction induced oxygen diffusivity enhancement in undoped nonstoichiometric ceria. *J. Phys. Chem. C* 119, **2015**, 13153-13159.

[Zhan12] Zhang, C.; Grass, M.E.; Yu, Y.; Gaskell, K.J.; DeCaluwe, S.C.; Chang, R.; Jackson, G.S.; Hussain, Z.; Bluhm, H.; Eichhorn, B.W.; Liu, Z. Multielement Activity Mapping and Potential Mapping in Solid Oxide Electrochemical Celss through the use of operando XPS. *ACS Catal.* 2, **2012**, 2297-2304.

[Zhao16] Zhao, Z.; Uddi, M.; Tsvetkov, N.; Yildiz, B.; Ghoniem, A.F. Redox Kinetics Study of Fuel educed Ceria for Chemical-Looping Water Splitting. *J. Phys. Chem. C* 120, **2016**, 16271-16289.

[Zhou07a] Zhou, G.; Shah, P.R.; Kim, T.; Fornasiero, P.; Gorte, R.J. Oxidation entropies and enthalpies of ceria-zirconia solid solutions. *Catalysis Today* 123, **2007**, 86-93.

[Zhou07b] Zhou, G.; Shah, P.R.; Montini, T.; Fornasiero, P.; Gorte, R.J. Oxidation enthalpies for reduction of ceria surfaces. *Surface Science* 601, **2007**, 2512-2519.

[Zhu03] Zhu, W.; Deevi, S. A review on the status of anode materials for solid oxide fuel cells. *Materials Science and Engineering: A* 362, 1, **2003**, 228-239.

Appendix

A Secondary Ion Mass Spectrometry

A.1 General

Secondary Ion Mass Spectrometry (SIMS) is generally a complex method of material analysis, more specifically a depth or surface analysis technique for the chemical composition of a sample, and is one of the ion beam techniques [McPh06, Heid14]. It uses the same mode of action as used in cathode sputtering, this means a beam of primary ions in the range of 250 eV - 30 keV strikes a surface and triggers a collision cascade inside the solid state with the energy transmitted by the incident particles, as shown in Figure A1. This collision cascade sets several atomic layers in motion and involves complex processes of energy transfer and interaction in the near-surface solid state interior. This leads to the emission of electrons, photons, atoms and molecules, the latter in neutral or ionic form, whereby the surface is irreversibly changed [Gros13, Heid14].

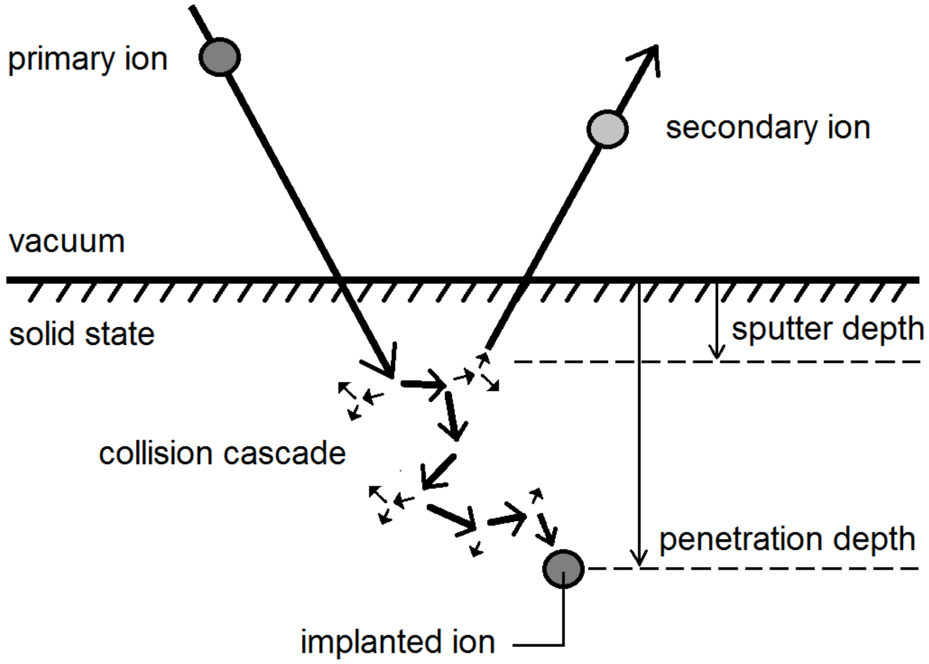

Figure A1. Schematic representation of the near-surface collision cascade. The primary ion has reached its penetration depth after a series of impacts. Adapted from [McPh06].

SIMS is therefore one of the destructive methods for material analysis. Furthermore, the introduction of primary ions into the sample changes their composition and structure. Of interest are the emitted ions, which are called secondary ions, from which the naming of the method results [Gros13]. The investigations are carried out in vacuum (usually in a high vacuum in the range of 10^{-7} - 10^{-8} mbar).

In the analysis of solids, all elements and isotopes of the periodic table can be detected by means of SIMS. Also, a three-dimensional analysis and the scanning of the sample surface are possible. In this way, SIMS provides information about the lateral and depth distributions of the elements contained in the sample. Technical limits of the lateral resolution, due to the focusing of the primary ion beam, are at 5 - 10 nm, and sub-nanometer dimensions are possible in principle for depth resolution, hereby limiting the choice of primary ion species. Positive ions such as O_2^+, Ar^+, Ga^+ or Cs^+ and negative ions such as O^{2-} or O^- are used [McPh06, Heid14].

Basically, due to a kind of intrinsic compensation of sample charges, negative primary ions are well suited to poorly conductive samples. At the same time, the change in the sample surface caused by primary ion bombardment, referred to as forward mixing, is quite strong. This is explained, in the case of positive secondary ions, with a high kinetic energy of the negative primary ions. On the other hand, forward mixing is less pronounced in the case of positive primary ion bombardment because of lower kinetic energy, which is why such primary ions are well suited to thinner samples. This effect is additionally enhanced if the positive primary ions are present as a molecule, as in O_2^+. This is vice versa for negative secondary ions. Elements of the first main groups tend to be easier to measure with positive secondary ions, since the ionization probability is higher here [Gros13].

A distinction is made between two operating modes for SIMS, the static SIMS procedure and the dynamic SIMS procedure. The static SIMS works with very low sputtering rates, partly with pulsed primary ion beam. This causes high sensitivity to the top monolayers of the samples. With dynamic SIMS, high sputtering rates and primary ion doses are used, resulting in high sensitivity to contamination. A single sputter event is understood to mean the penetration of the primary ions into the sample, the formation of a collision cascade and the dissolution of secondary particles. This event lasts less than 10^{-12} s. At primary ion densities below 10^{12} $s^{-1}cm^{-2}$, there is no interaction with products of other sputtering events since the maximum cross section of a primary ion is on the order of 10 nm^2. Each event is therefore independent of preceding, succeeding or parallel successors [Gros13]. From a time perspective, this means that with dynamic SIMS up to 100 impacts · min^{-1} of primary ions occur in a certain surface area, whereas with static SIMS only 0.01 - 0.1 impacts · min^{-1} are to be expected. With a monatomic layer observation periods of 1 h can be realized with static SIMS, static refers to the extensive preservation of the surface [Gros13, Heid14].

In consequence, the major difference being that static SIMS does not provide depth profiling capabilities, whereas dynamic SIMS does. A possible simultaneous detection of all chemical isotopes in the ppm to ppb range, a high mass resolution, lateral and depth resolution in the nm range are decisive advantages for using the method ex situ for studies of diffusion processes in solids.

A.2 Quantification

The detectable secondary ion intensity I_i of a species i is dependent on the intensity of the primary ions I_P, the sputter yield Y, the ionization probability of the species α_i, the detection efficiency of the SIMS machine γ, and the concentration of the species in the sample c_i, so it can be calculated as follows:

$$I_i = I_P Y \alpha_i \gamma c_i \ . \tag{A1}$$

If one wants to deduce the concentration of species i in the solid state, one is confronted with the problem that the secondary ion current is non-linearly dependent on it. The reason for this is the ionization probability. It is not constant but dependent on the atomic environment of the i-type atom in the solid, which is called matrix effect, as well as on the primary-ion species used. It is the reason that the count of the secondary ions of the species i as a function of time is given as a measured variable in the secondary ion mass spectrometry.

Conclusions on the concentration of the species i in the sample are not possible without assumptions or comparative measurements on standard samples of known composition, therefore it is often more accurate to keep the measure of the count rate and to specify only a depth profile or a lateral distribution. The sputtering rate or the measurement of the sputter crater on the sample surface can be used to deduce the depth or the location when the forward mixing is not very pronounced.

However, a statement about an isotopic distribution of species i in the sample is possible because the ionization probabilities of the species isotopes are the same. In the case of oxide samples, which display an isotope mixture primarily made up of $^{16}O_2$, the corresponding oxygen isotopes are $^{17}O_2$ and $^{18}O_2$. If the quotients of the corresponding secondary ion currents are formed, the ionization probability is reduced from Equation (A1).

Differences in sputter yield and ionisation yield can be neglected for isotopes of the same element so that the depth distribution of the atomic fraction of the rare stable ^{18}O isotope $c(^{18}\mathrm{O})$ can be quantified via:

$$c(^{18}\mathrm{O}) = \frac{I(^{18}\mathrm{O})}{I(^{18}\mathrm{O}) + I(^{16}\mathrm{O})}, \qquad \text{(A2)}$$

from the SIMS raw data, where I is the intensity of the SIMS signal [Knob17].

A.3 Applied SIMS methods and techniques

Although the instrumentation required and the information content provided can be quite different, the basic instrument setup for SIMS remains essentially the same. In all cases, mass spectra are used to identify signals of interest. Imaging, along with depth profiling, is used to define the location of the specific signals of interest. Instrument designs are defined by the type of mass filter used within the secondary ion column.

In the context of this work, three different types of SIMS machines with reference to the secondary ion column were used in the dynamic operation mode, which shall be described briefly. In general the secondary ion column is the section of a SIMS machine where collection, filtering, focusing and detection of the emitted secondary ions occur. The layout is primarily set by the type of mass filter used, which additionally defines the capabilities and limitations of the respective SIMS instrument.

The most applied mass filter types, which were also used in the context of this work, are the quadrupole mass filter, the magnetic sector mass filter and the Time-of-Flight (ToF) mass filter. As secondary ions carry with them a charge, SIMS relies on the ability to resolve the m/q ratio of the emitted secondary ions in the mass filter region of the instrument, and the majority of them is in the +1 or -1 charge state. Therefore it is often assumed that the mass is equal to the m/q ratio.

The charge allows the ions to be extracted from the sample surface and passed through the respective secondary ion column. The detector records the number of secondary ions passing per unit time and converts the number of ions into a quantity that is then converted into some frequency value, i.e. counts per second, which in general requires linearity of the conversion process. The specific layout of secondary ion columns is described and discussed in detail in the respective literature [Heid14].

The most direct method of measuring the depth distribution of the atomic fraction of ^{18}O isotopes in oxides is Secondary Ion Mass Spectrometry depth profiling (SIMS IEDP) or cross section line scan (SIMS IELS) as is shown schematically in Figure A2 [Kiln84, Chat92, Fiel01]. The line scan technique involves sectioning of the sample after isotope exchange in a plane perpendicular to the exchange surface and analysing the isotope fraction profile by laterally scanning the primary ion beam across the contact line of the two exposed (half) surfaces.

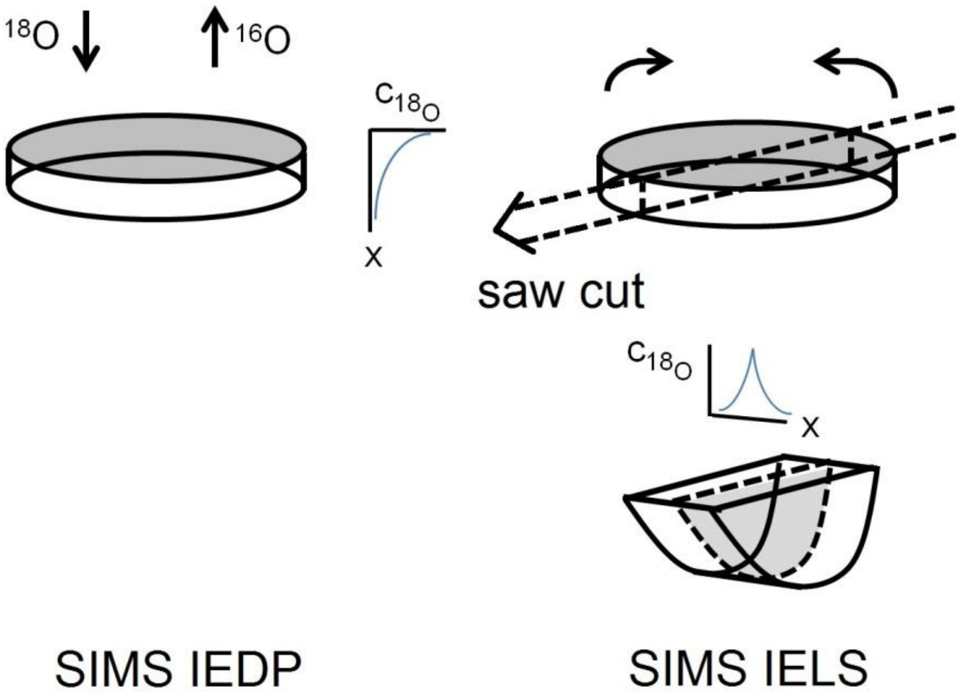

Figure A2. Schematic diagram summarising the SIMS IEDP technique for $\sigma < 5$ µm (left) and the SIMS IELS technique for 10 µm $< \sigma < h/4$ (right) [Knob17].

In Figure A3 a microscopic image of a sectioned sample of 10 % zirconia-doped ceria $Ce_{0.9}Zr_{0.1}O_2$ as used in this work is shown. As it is visible the assembling leaves a small joint gap of typically 1 - 4 µm which is then also displayed in the resulting SIMS ion image as well as in the SIMS line scan depth profile as can be seen in Figure A4 and Figure A5.

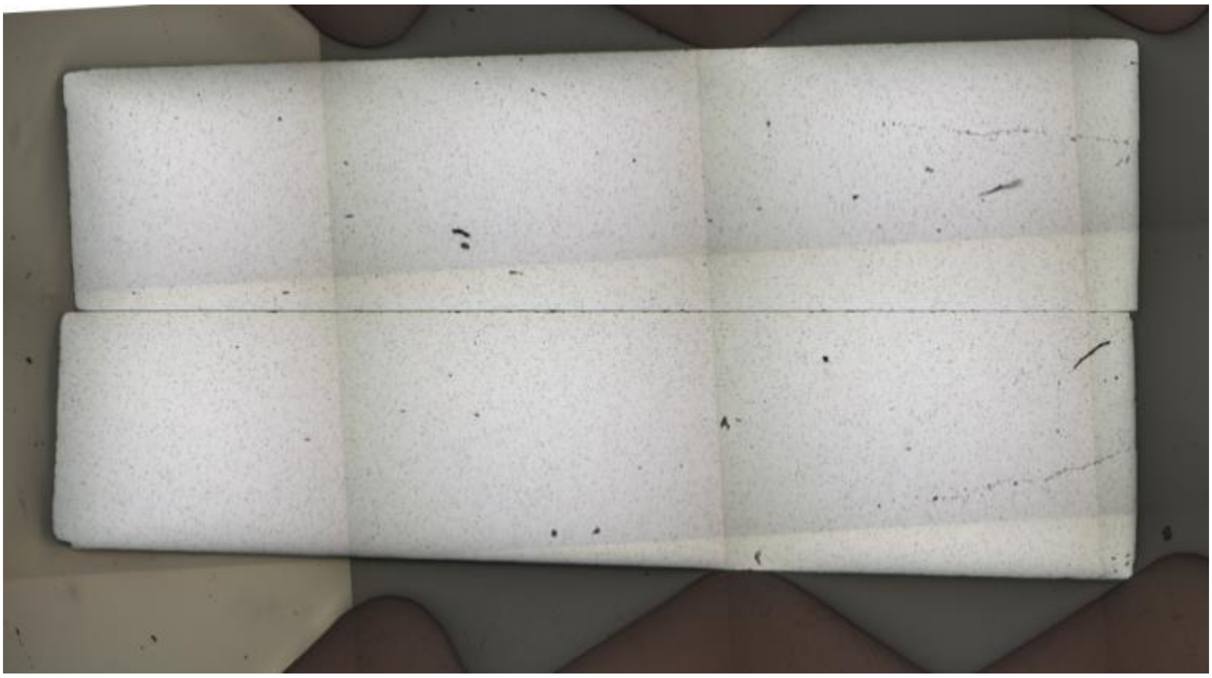

Figure A3. Microscopic image of a sectioned sample of 10 % zirconia-doped ceria $Ce_{0.9}Zr_{0.1}O_2$ as used in this work. As it is visible the assembling leaves a small joint gap of typically 1 - 4 µm. The image is composed of several individual images, which explains the fluctuations in brightness.

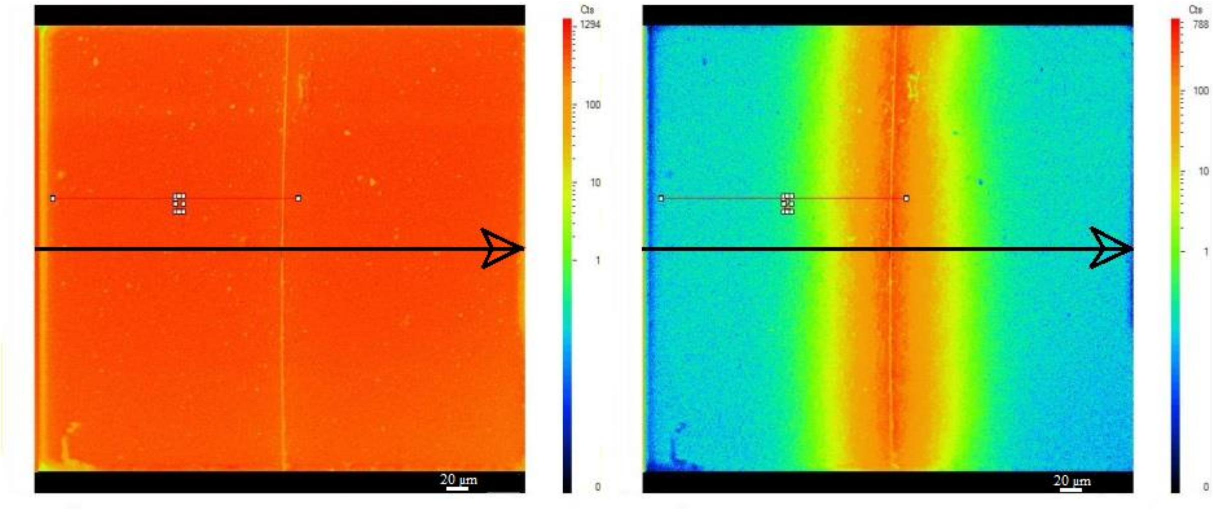

Figure A4. Ion image for ^{16}O (left) and ^{18}O (right) in logarithmic scale of a sectioned sample of 10 % yttria-doped ceria as used in this work. The blank text boxes are artefacts without physical significance. The arrow indicates the direction of the line scan half. The SIMS measurements were done in imaging mode with a CAMECA IMS 7f N with a double focusing magnetic sector mass filter [Knob17].

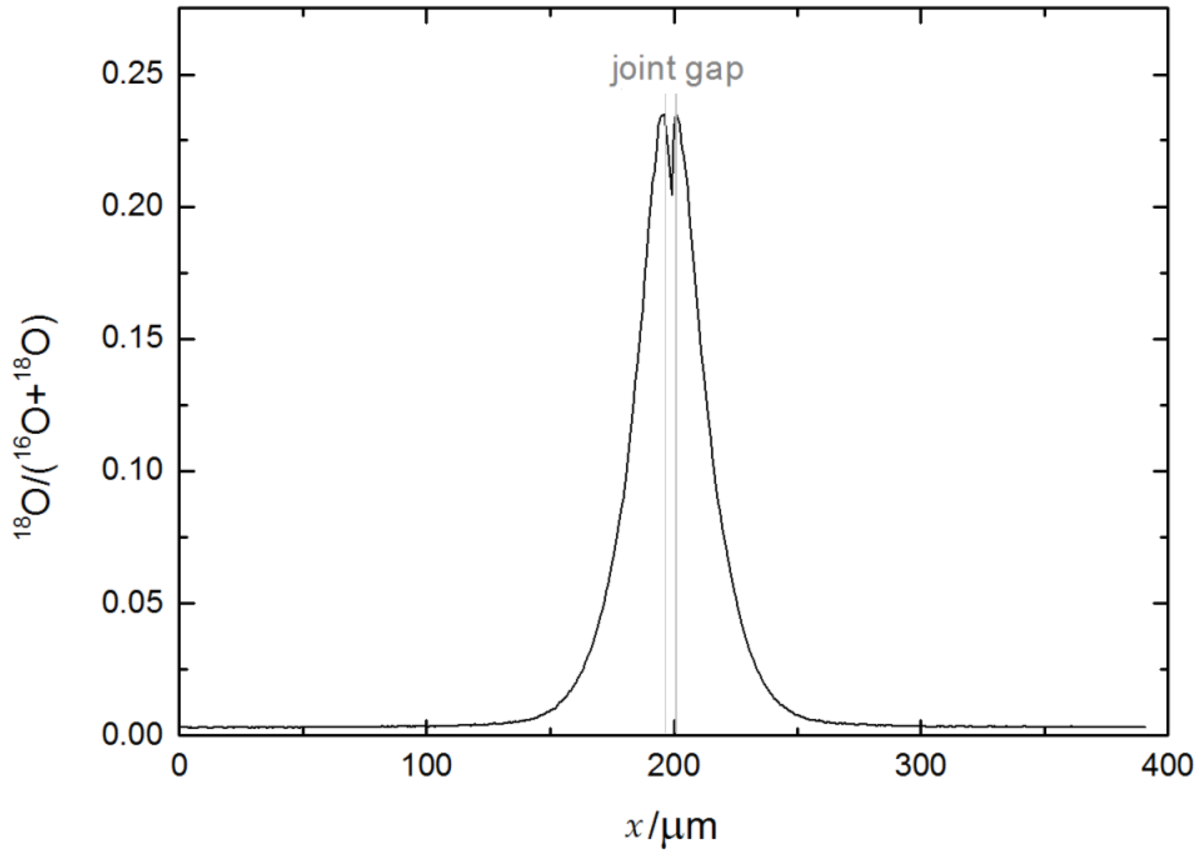

Figure A5. SIMS line scan depth profile measured in a nominally un-doped polycrystalline ceria as used in this work with the isotope fraction of ^{18}O perpendicular to the original surface. The SIMS IELS measurements were done with a TOF-SIMS IV with a Time-of-Flight mass filter [Knob17].

B Limitations of the simultaneous determination of D_O and K_O

B.1 Time and δ dependence of the ^{18}O surface concentration

A first discussion about limitations of the accurate simultaneous determination of D_O and K_O data by SIMS methods was given by CHATER et al. [Chat92] and continued comprehensively by FIELITZ and BORCHARDT [Fiel01], which will be explained in the following sections. With isotope exchange followed by SIMS IEDP or IELS being the most direct method of measuring D_O and K_O of oxide materials the accuracy is based mainly on the fact that the ratio $^{18}O/^{16}O$ of the natural isotope abundancies is about 1/500, meaning the dynamic range of the depth distribution of the atomic fraction $c(^{18}O)$ can reach almost three orders of magnitude.

Differences in sputter yield and ionisation yield can be neglected for isotopes so that $c(^{18}O)$ can be quantified via Equation (A2).

Under most experimental conditions the oxygen incorporation is described by Equation (40) and the flux of oxygen at the gas/solid interface must be equal to the diffusional flux of oxygen in the solid:

$$-D_\mathrm{i}\left.\frac{\partial c_\mathrm{i}}{\partial x}\right|_{x=0} = -K_\mathrm{i}\Delta c_\mathrm{i}(x=0). \tag{B1}$$

The analytical solution of this diffusion problem in a semi-infinite homogeneous media as given by CRANK [Cran75] was proposed in a more specific notation by FIELITZ and BORCHARDT [Fiel01]:

$$\frac{c_{^{18}\mathrm{O}}(x,t)-c_{^{18}\mathrm{O}}^{\infty}}{c_{^{18}\mathrm{O}}^{g}-c_{^{18}\mathrm{O}}^{\infty}} = \mathrm{erfc}\left(\frac{x}{\sigma}\right) - \exp\left(2\frac{x}{\sigma}\sqrt{\frac{t}{\tau}}+\frac{t}{\tau}\right)\mathrm{erfc}\left(\frac{x}{\sigma}+\sqrt{\frac{t}{\tau}}\right), \quad \text{with } \sigma \equiv 2\sqrt{Dt} \text{ and } \tau \equiv \frac{D}{K^2} \tag{B2}$$

where $c_{^{18}O}^{\infty}$ is the natural abundance of ^{18}O in the sample (at $x \to \infty$), σ is the diffusion length of the tracer isotope and τ the characteristic time constant which determines the duration that is necessary to reach equilibrium between the ^{18}O gas concentration and the ^{18}O concentration at the surface of the solid. Equation (B2) is valid for constant values of D and K.

This condition is in general not strictly valid for chemical equilibration with a tracer concentration gradient at the gas/solid interface, but for moderate dependencies of D and K on the defect concentrations (changing locally with time).

Approximate values of the chemical parameters can be derived for the case of a chemical potential gradient at the gas/solid interface. By setting $x = 0$ one can calculate the time dependence of the ^{18}O concentration at the solid surface $c_\mathrm{s}(t) = c(0,t)$:

$$c_\mathrm{s}(t)-c_\infty = \left(c_\mathrm{g}-c_\infty\right)\left[1-\exp\left(\frac{t}{\tau}\right)\mathrm{erfc}\left(\sqrt{\frac{t}{\tau}}\right)\right]. \tag{B3}$$

In Figure B1 the time dependence of the ^{18}O concentration at the surface, $c_\mathrm{s}(t)$, for $\mu_\mathrm{O} = \mathrm{const.}$, is plotted for a gas concentration, $c_\mathrm{g} = 1$, and a natural abundance, $c_\infty = 0.002$, with t/τ being the ratio of the annealing time t and the characteristic time constant τ. The annealing time t is given for each isotope exchange experiment at annealing temperature T and pressure p.

It is obvious from Figure B1 that beyond the “working range” between $t/\tau > 10$ and $t/\tau < 10^{-6}$ the error is too large.

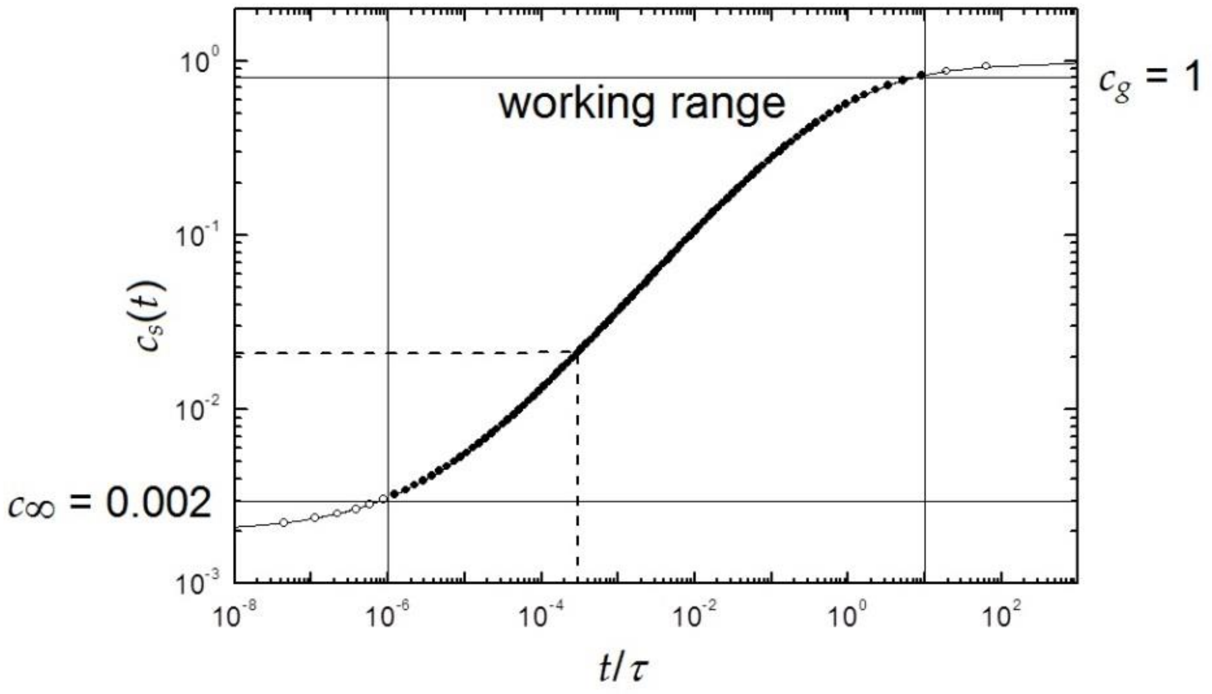

Figure B1. Dependence of the ^{18}O concentration at the surface, $c_S(t)$, on the annealing time t (Equation B2 for $c_g = 1$ and $c_\infty = 0.002$). Solid circles show the “working range” for calculating t/τ ratios from measured surface concentrations. Adapted from [Fiel01].

The experimental work in non-equilibrium conditions utilizes reduced samples, with the respective oxygen non-stoichiometry δ of the sample depending on the temperature of the reduction step and the sample type. During the isotope exchange step the ^{18}O will be incorporated from $^{18}O_2$ into the sample bulk, re-oxidizing the sample (neglecting isotope exchange). It is then possible to estimate the maximum ^{18}O/O ratio related to the concentration of oxygen vacancies, which is measurable by meanings of SIMS, so that $\left(^{18}\mathrm{O}/\mathrm{O}\right)_{\max} = f(\delta)$:

$$c(^{18}\mathrm{O}) = \frac{^{18}\mathrm{O}}{^{18}\mathrm{O}+^{16}\mathrm{O}} = \frac{2c_\infty + \left(c_\mathrm{g} - c_\infty\right)\delta}{2}. \tag{B4}$$

B.2 Simultaneous determination of D_O and K_O

The simultaneous determination of oxygen diffusity and surface exchange coefficient by measuring the depth distribution of the atomic fraction of ^{18}O isotopes in oxides is based on the analysis of the measured SIMS depth profiles by fitting with Equation (B2), which, however, works well only in a limited parameter range.

An adequate annealing time for the isotope exchange is therefore crucial, as can be deduced by Figure B1. For $t > 10\tau$ the determination of τ (and therefore K) may very well lead to significant error. To determine an accurate value of the diffusion coefficient, according to CHATER the dynamic range of the ^{18}O concentration should comprise one order of magnitude or more [Chat92]. As can be derived from Figure B1 this leads to the following range of adequate annealing time:

$$3\cdot 10^{-4}\tau \le t \le 10\tau . \tag{B5}$$

Given practical values of t from 100 s to 1 month with Equation (B3) the measurable range of τ from 10 to 10^{10} s (≈ 317 years) can be derived. Additional limitations are set by measurement uncertainties of the SIMS method itself as discussed in more detail in section C of the appendix.

KILNER and DE SOUZA have estimated that 30 nm is the minimum for the diffusion length σ that can be measured caused by ion beam mixing only. Further limitations are surface roughness or a deposited conductive layer to prevent sample charging. Crater base roughening during SIMS depth profiling limits SIMS IEDP to 10 μm, whereas for the line scan method the working maximum is about 1 mm [Kiln96].

Utilizing Equation (B2) with the discussed working parameters an accessible K-D window for the simultaneous determination of D_{O} and K_{O} that is partially shown in Figure B2 can be drawn. The lines define a range of parameters within which a simultaneous determination is possible with acceptable errors. In order to be in this working parameter range, it is crucial to choose an adequate annealing time.

A more detailed discussion of depth profiles calculated at the intersection points of the lines as well as a qualitative estimation of the error which results if τ, D_{O} and K_{O} values are determined at the intersection points is given by FIELITZ and BORCHARDT [Fiel01]. Further comprehensive calculations and discussion on this topic are given by FISCHER and HERTZ [Fisc12].

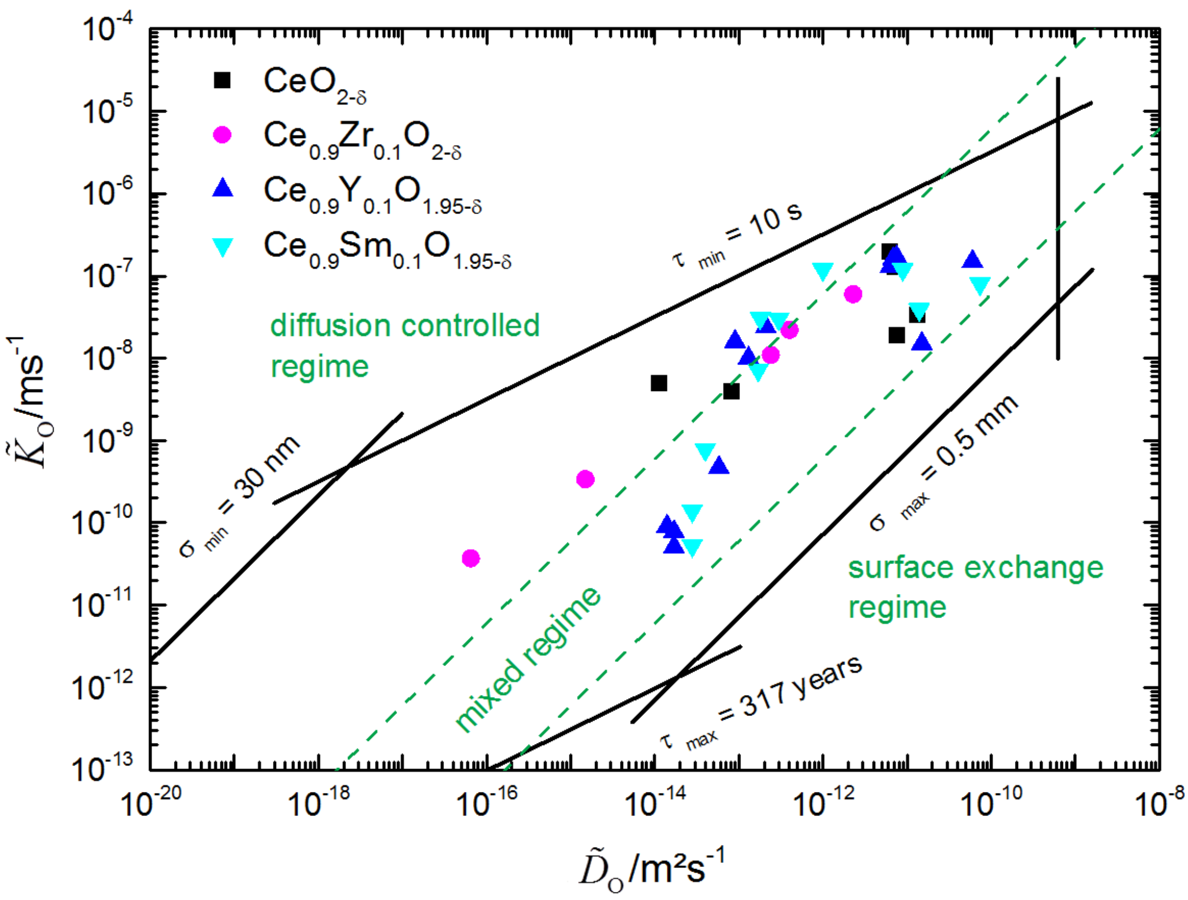

Figure B2. The accessible *K*-*D* window for the simultaneous determination of D_O and K_O plotted partially together with *K*-*D*-Data derived in non-equilibrium experimental conditions in the temperature range $T = 300$ to $T = 800$ °C utilizing $C^{18}O_2$. Additionally the boundaries for the kinetic regime are drawn, which were calculated according to $L = \frac{h}{2}\frac{K}{D}$ with $h = 1$ mm and L being the characteristic dimensionless parameter of the kinetic regimes. The calculations were done according to [Fiel01] and [Knob15].

C Validation of the measured oxygen isotope fraction distributions

C.1 Influence of temperature and annealing time

As given by Equation (24), diffusion data can often be described by an ARRHENIUS Equation, which describes the temperature dependence of the diffusion coefficient. If the duration of the isotherms of the diffusion annealing is considerably longer than the time required for heating and cooling, a correction of the annealing time is not required. In the case of very short annealing times, the annealing time has to be corrected in the sense of an effective diffusion time [Kill62]:

$$D(T_0)\cdot t_{\mathrm{eff}} = \int_0^t D\left[T\left(t'\right)\right]dt' . \tag{C1}$$

If the temperature-time-dependence $T(t)$ is known, solutions for the simplified case of linear temperature changes over time are given [Kill62]. For most temperature curves, however, this Equation can only be solved graphically or numerically. A numerical estimation with a temperature profile shown in Figure C1 for $T = 900$ ° C of a ceria sample results in an effective annealing time of ≈ 160 s for the determined activation enthalpy of (1.02±0.11) eV and the given annealing duration of 140 s.

In general, the dependency of the effective annealing duration on the activation enthalpy in Equation (24) is rather low. As the experimental setup used in this work utilizes an IR radiation heated furnace which allows fast heating rates up to 100 K/s in the temperature range $300\ °\mathrm{C} \leq T \leq 900\ °\mathrm{C}$, the time dependency is technically controllable. On the other hand, the exact temperature measurement is very important for the determination of the diffusion coefficient, which is why special attention was required here. As shown in Figure 9 of section 5.2 the samples were placed on a platinum mesh, avoiding contact of the platinum with the sample surface, in a quartz holder. In the context of this work, the temperature-time-dependence $T(t)$ of a sample and the sample holder was measured simultaneously, as given in Figure C1. The ceria sample was cut and thermally connected with the thermocouple (N-type, 0.25 mm, TC Direct, Germany) via silver lacquer.

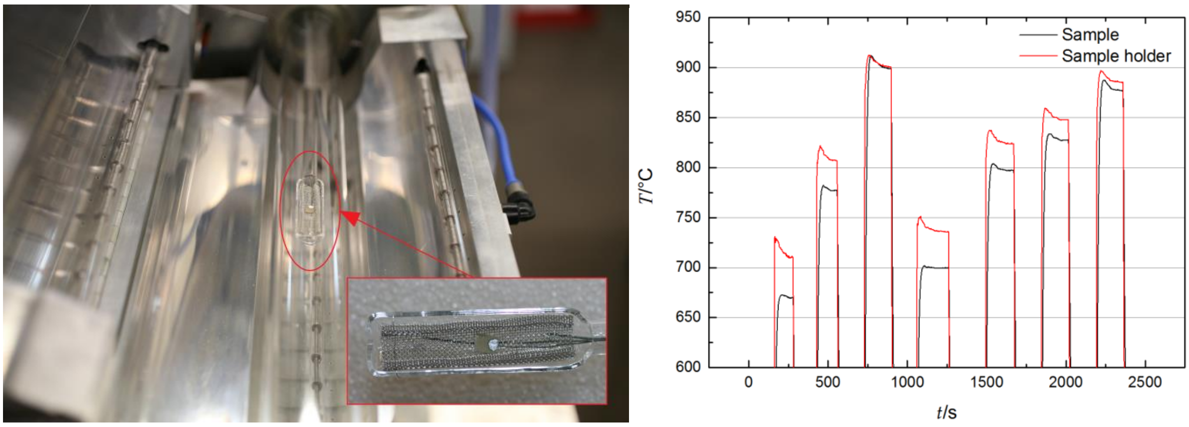

Figure C1. The temperature-time-dependence $T(t)$ of a sample and the sample holder, measured simultaneously (right side). The ceria sample was cut and thermally connected with the thermocouple (N-type, 0.25 mm) via silver lacquer. Two thermocouples (N-type, 0.5 mm) measured the temperature at the platinum sample holder, assuring a thermal homogeneity of 10 K over a distance of 15 mm, which is basically dependent on the position of the quartz sample holder within the furnace (left side).

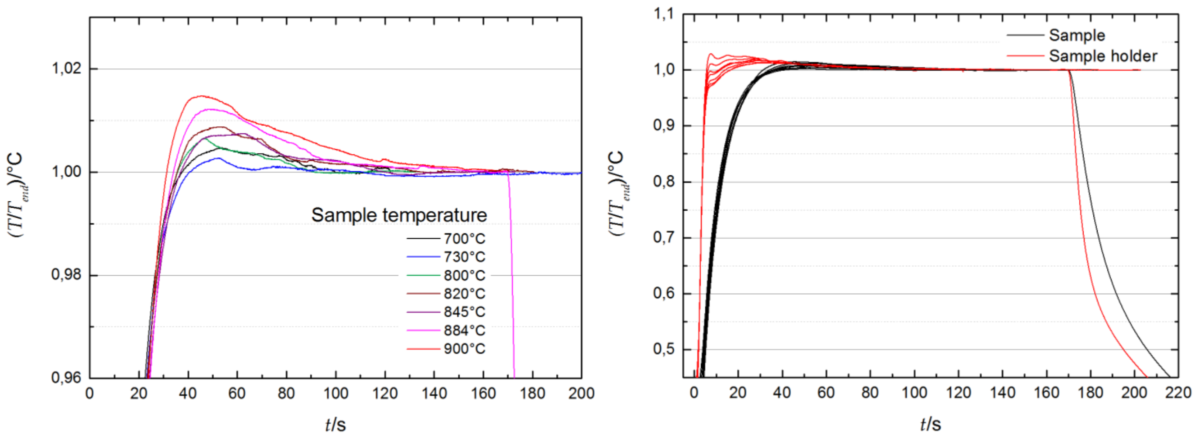

Figure C2. The measured temperature-time-dependency of the sample (left side) and of the sample compared to the sample holder (right side). A temperature dependency is revealed, and also a temperature difference ΔT between sample and sample holder can be seen, which has a temperature dependency itself, proposing $\Delta T = f\left(t,T\right)$.

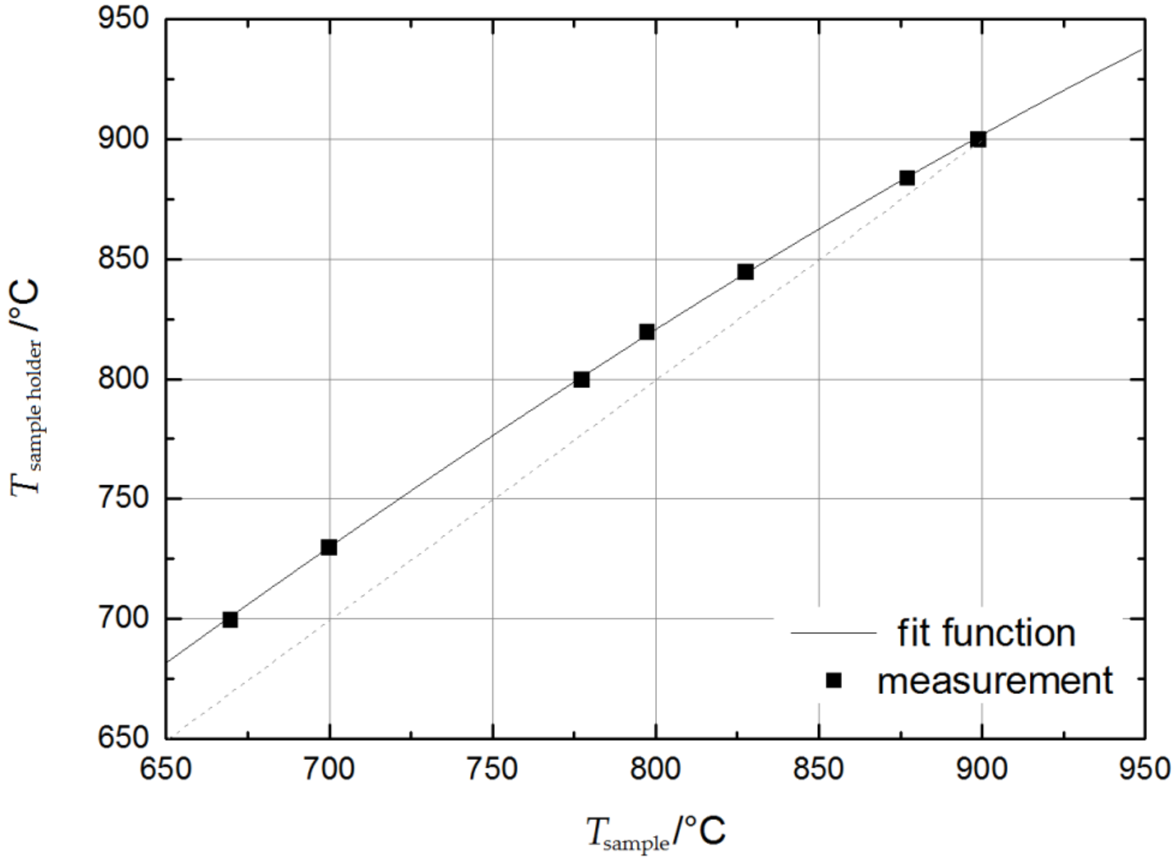

Figure C3. Measured temperature difference ΔT between sample and sample holder (deviation of the data points from the grey dotted line), which has a temperature dependency itself, together with the fit function (C3) for the correction of ΔT during the diffusion annealing, which is necessary as the furnace is controlled according to the temperature of the sample holder.

Two thermocouples (N-type, 0.5 mm, TC Direct, Germany) measured the temperature at the platinum sample holder, assuring a thermal homogeneity of 10 K over a distance of 15 mm, which is basically dependent on the position of the quartz sample holder within the furnace. In Figure C2 the measured temperature-time-dependency of the sample and the sample holder in comparison is given, where a temperature dependency itself is revealed, and also a temperature difference ΔT between sample and sample holder can be seen in Figure C2, which has a temperature dependency itself. The complexity of the relation

$$\Delta T = f\left(t, T\right) \tag{C2}$$

suggested the use of a fit function:

$$T_{\text{sample holder}} = T_{\text{sample}} + 21 - 0.11 T_{\text{sample}} + 4.45 \cdot 10^{-4} T_{\text{sample}}^{2} - 3.85 \cdot 10^{-7} T_{\text{sample}}^{3}, \tag{C3}$$

as given in Figure C3 for the correction of ΔT during the diffusion annealing, which is necessary as the furnace is controlled according to the temperature of the sample holder. As can be seen from Figure C2, a constant ΔT between sample and sample holder is achieved after about 150 s, which then can be assumed as the shortest rational annealing time that can be controlled via the given correction term of ΔT (FISCHER and HERTZ [Fisc12] give a lower limit for the annealing time of 60 s).

C.2 Influence of the primary ion species

Considering that a primary ion beam contains a natural oxygen isotope distribution and that in case of SIMS measurement with primary ions other than oxygen, the measured ^{18}O/O ratio of the sample is displayed correctly, the influence of the primary ion species can be estimated by measuring the ^{18}O distribution in a sample with oxygen primary ions as well as with argon primary ions and determine the ^{18}O/O ratio of the sample. Then the ^{18}O/O ratio can be defined in the following way:

$$^{18}\text{O}_{\text{meas}}\left(\text{O}^{-}\right) = {}^{18}\text{O}_{\text{sample}} + \Delta^{18}\text{O}_{\text{g}}, \tag{C4}$$

$$^{16}\text{O}_{\text{meas}}\left(\text{O}^{-}\right) = {}^{16}\text{O}_{\text{sample}} + \Delta^{16}\text{O}_{\text{g}}, \tag{C5}$$

$$^{18}\text{O}_{\text{g}} = 0.002\,{}^{16}\text{O}_{\text{g}}, \tag{C6}$$

$$\Delta^{18}\text{O}_{\text{g}} = 0.002 \cdot \Delta^{16}\text{O}_{\text{g}}, \tag{C7}$$

$$\frac{{}^{18}\mathrm{O}_{\mathrm{sample}}}{{}^{16}\mathrm{O}_{\mathrm{sample}}+{}^{18}\mathrm{O}_{\mathrm{sample}}}=\frac{{}^{18}\mathrm{O}_{\mathrm{meas}}\left(\mathrm{O}^{-}\right)-\Delta{}^{18}\mathrm{O}_{\mathrm{g}}}{{}^{18}\mathrm{O}_{\mathrm{meas}}\left(\mathrm{O}^{-}\right)+{}^{16}\mathrm{O}_{\mathrm{meas}}\left(\mathrm{O}^{-}\right)-\Delta{}^{18}\mathrm{O}_{\mathrm{g}}-\Delta{}^{16}\mathrm{O}_{\mathrm{g}}}, \tag{C8}$$

$$\frac{{}^{18}\mathrm{O}_{\mathrm{sample}}}{{}^{16}\mathrm{O}_{\mathrm{sample}}+{}^{18}\mathrm{O}_{\mathrm{sample}}}=\frac{{}^{18}\mathrm{O}_{\mathrm{meas}}\left(\mathrm{O}^{-}\right)-\Delta{}^{18}\mathrm{O}_{\mathrm{g}}}{{}^{18}\mathrm{O}_{\mathrm{meas}}\left(\mathrm{O}^{-}\right)+{}^{16}\mathrm{O}_{\mathrm{meas}}\left(\mathrm{O}^{-}\right)-501\cdot\Delta{}^{18}\mathrm{O}_{\mathrm{g}}}. \tag{C9}$$

From the measurement of the ^{18}O distribution of the sample with argon primary ions $\frac{{}^{18}\mathrm{O}_{\mathrm{sample}}}{{}^{16}\mathrm{O}_{\mathrm{sample}}+{}^{18}\mathrm{O}_{\mathrm{sample}}}=\frac{{}^{18}\mathrm{O}_{\mathrm{meas}}(\mathrm{Ar}^{+})}{{}^{16}\mathrm{O}_{\mathrm{meas}}(\mathrm{Ar}^{+})+{}^{18}\mathrm{O}_{\mathrm{meas}}(\mathrm{Ar}^{+})}$ at the surface is known and from the measurement with oxygen primary ions $^{18}\mathrm{O}_{\mathrm{meas}}$ and $^{16}\mathrm{O}_{\mathrm{meas}}$ at the same depth are known. Therefore, $\Delta^{18}\mathrm{O}_{\mathrm{gas}}$ can be calculated (considering $\Delta^{18}\mathrm{O}_{\mathrm{gas}}$ being constant):

$$\Delta{}^{18}\mathrm{O}_{\mathrm{g}}=\frac{{}^{16}\mathrm{O}_{\mathrm{meas}}\left(\mathrm{Ar}^{+}\right)\cdot\left[{}^{18}\mathrm{O}_{\mathrm{meas}}\left(\mathrm{O}^{-}\right)+{}^{18}\mathrm{O}_{\mathrm{meas}}\left(\mathrm{Ar}^{+}\right)\right]-{}^{18}\mathrm{O}_{\mathrm{meas}}\left(\mathrm{Ar}^{+}\right)\cdot\left[{}^{18}\mathrm{O}_{\mathrm{meas}}\left(\mathrm{O}^{-}\right)+{}^{16}\mathrm{O}_{\mathrm{meas}}\left(\mathrm{O}^{-}\right)\right]}{{}^{16}\mathrm{O}_{\mathrm{meas}}\left(\mathrm{Ar}^{+}\right)-500\cdot{}^{18}\mathrm{O}_{\mathrm{meas}}\left(\mathrm{Ar}^{+}\right)}. \tag{C10}$$

The real oxygen isotope fraction depth profile $c(x,t)=\frac{{}^{18}\mathrm{O}_{\mathrm{sample}}}{{}^{16}\mathrm{O}_{\mathrm{sample}}+{}^{18}\mathrm{O}_{\mathrm{sample}}}$ can thus be calculated from the SIMS measurement with oxygen primary ions inserting Equation (C10) into Equation (C9).

Alternatively, it is possible to measure the ^{18}O distribution with oxygen primary ions (assuming the influence of the primary ions on the measured signal being small) and calculate the diffusivity:

$$^{18}\mathrm{O}_{\mathrm{meas}}-{}^{18}\mathrm{O}_{\mathrm{meas},\infty}\approx{}^{18}\mathrm{O}_{\mathrm{sample}}-{}^{18}\mathrm{O}_{\mathrm{bulk}}=({}^{18}\mathrm{O}_{\mathrm{meas,s}}-{}^{18}\mathrm{O}_{\mathrm{meas},\infty})erfc\left(\frac{x}{2\sqrt{Dt}}\right). \tag{C11}$$

This calculation is valid for $t >> \tau$ but can be also applied in other cases with an acceptable error according to [Fiel01] if only the region $x > \sigma$ is used for the fitting procedure.

From the surface measurements with argon primary ions τ can be determined (confer Equation (B3)) via:

$$c_{\mathrm{s}}(t)=\frac{{}^{18}\mathrm{O}_{\mathrm{sample}}}{{}^{16}\mathrm{O}_{\mathrm{sample}}+{}^{18}\mathrm{O}_{\mathrm{sample}}}=\left(c_{\mathrm{g}}-c_{\infty}\right)\left[1-\exp\left(\frac{t}{\tau}\right)\mathrm{erfc}\left(\sqrt{\frac{t}{\tau}}\right)\right]+c_{\infty}, \tag{C12}$$

where $K=\sqrt{\frac{D}{\tau}}$ yields the corresponding surface exchange coefficient of oxygen.

In Figure C4 a comparison of measured $^{18}O/O$ and ^{18}O distributions for different primary ion species is shown together with their corresponding fits. From the variance of the calculated parameters *D* and *K* the influence of the primary ion species can be estimated, which is in the range of ~ 10 % for *D*, but about one order of magnitude for *K*.

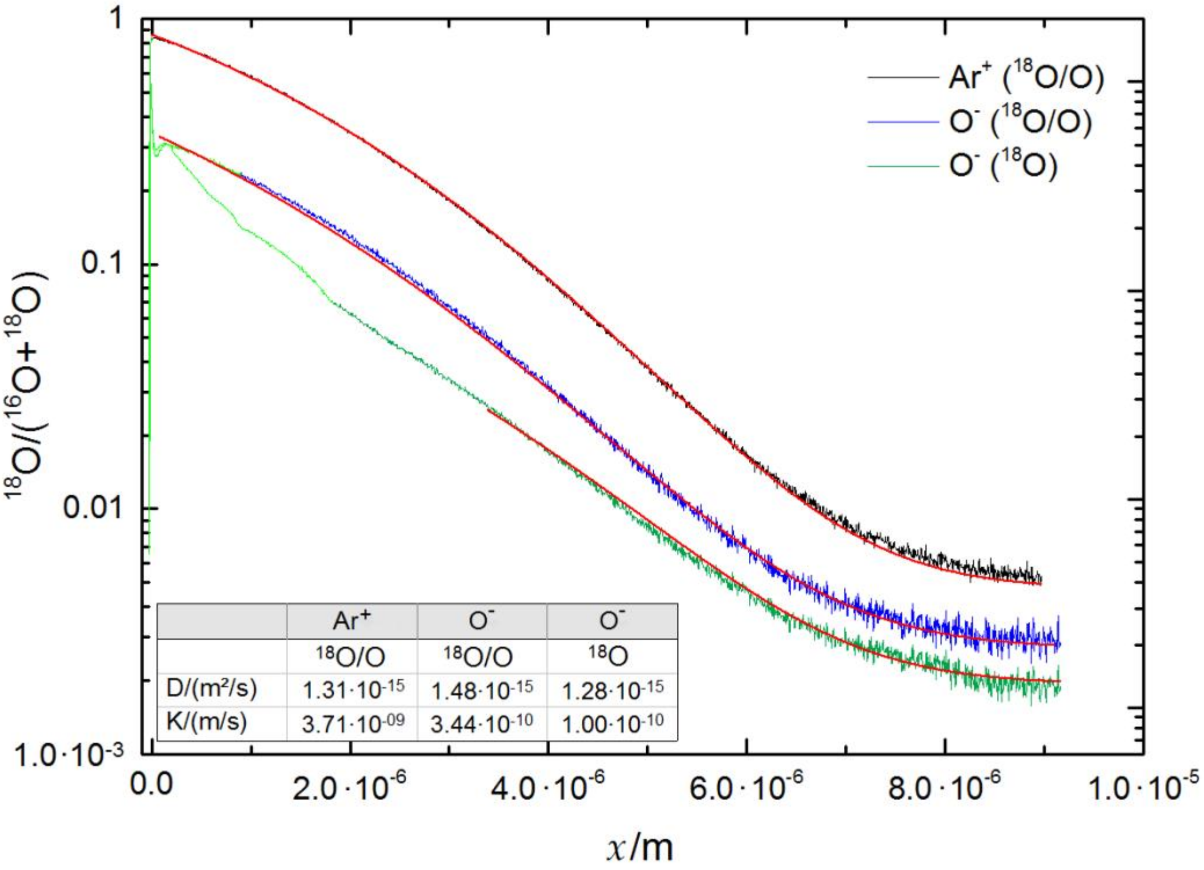

	Ar^+	O^-	O^-
	$^{18}O/O$	$^{18}O/O$	^{18}O
$D/(m^2/s)$	$1.31\cdot10^{-15}$	$1.48\cdot10^{-15}$	$1.28\cdot10^{-15}$
$K/(m/s)$	$3.71\cdot10^{-09}$	$3.44\cdot10^{-10}$	$1.00\cdot10^{-10}$

Figure C4. Comparison of measured $^{18}O/O$ and ^{18}O distributions for different primary ion species Ar^+ and O^-, together with their corresponding fits and calculated parameters *D* and *K*.

C.3 Deconvolution of SIMS line scan profiles

Measured SIMS profiles always contain distortions because of sample imperfections like surface roughness and ion-matrix interactions like ion beam mixing in the case of depth profiling (vertical uncertainty), and because of apparatus factors like a defined spot size of the primary ion beam in the case of line scan mode (lateral uncertainty). In functional analysis this can be described as convolution. The measured concentration $C_i(x)$ of a species i as a function of sputtered depth or scanned length can therefore be expressed as a convolution integral:

$$C_\mathrm{i}(x) = \int_{-\infty}^{\infty} R(x-y) C_\mathrm{i}^0(y)dy\,, \tag{C13}$$

where $R(x)$ is the resolution function and C_i^0 the original concentration distribution of a species i. The function value of the weighting function C_i^0 at a point y indicates how much the value y of the weighted function that is behind, i.e. $R(x-y)$, is included in the value of the result function at point x. Only in the case of the ideal resolution function $R(x)=\delta(x)$, with $\delta(x)$ being the delta-function, the measurement is not falsified. In the case of SIMS depth profile measurements the resolution function can be determined by measuring so-called as-prepared samples with δ-shaped distributions of the species i.

In general $R(x)$ can then be described by a GAUSSIAN distribution with variance σ_R^2. If the original distribution $c_\mathrm{i}(x)$ of a species i can be described by a GAUSSIAN distribution as well, the convolution of two GAUSSIAN distributions with variances σ_R^2 and σ_c^2 results in a GAUSSIAN distribution with the variance $\sigma_I^2 = \sigma_R^2 + \sigma_c^2$, meaning that the mathematically complex deconvolution can be approximated by a simple algebraic operation. It is particularly important to take the resolution function into account when considering very steep concentration distributions, especially if they are in the range of the resolution.

In the case of the SIMS line scan technique the spot size of the primary ion beam is the limiting apparatus factor in terms of dissolvable diffusion lengths. The SIMS line scan technique as used in this work and described in section A3 involves sectioning of the sample after isotope exchange in a plane perpendicular to the exchange surface and analysing the isotope fraction profile by laterally scanning the primary ion beam across the contact line of the two exposed (half) surfaces.

The assembling leaves a small joint gap of typically 1 - 4 µm which is then also displayed in the resulting SIMS ion image as well as in the SIMS line scan depth profile as can be seen in Figure A4 and Figure A5. When a SIMS Workstation (Hiden Analytical Ltd, UK) was used for measurements, a spot size of about 50 µm in x-direction had to be considered (the raster-scanned area was $500 \cdot 500$ µm^2 in imaging mode) and the measured ^{18}O distributions were significantly distorted. Here the resolution function is approximated by a GAUSSIAN distribution with the FWHM being the spot size and the area being normalized to unity.

The convolution can only be approximated by an iteration approach. Here the measured SIMS line scan profile is analyzed according to Equation (B2), and with the determined parameters *D* and *K* the actual ^{18}O distribution is simulated, taking into account the joint gap (5 µm), which is also calculated. The simulated ^{18}O distribution is then stepwise convoluted with the approximated resolution function and the iteration is repeated until a good fit between the convoluted and the measured ^{18}O distribution is achieved. As can be seen in Figure C5, the measured intensity ratio in the region around the joint gap is significantly decreased, together with a slight broadening of the concentration profile, which influences primarily the determination of the parameter *K*. The difference between the adjusted and the not-adjusted determination was estimated to be ~ 15 %.

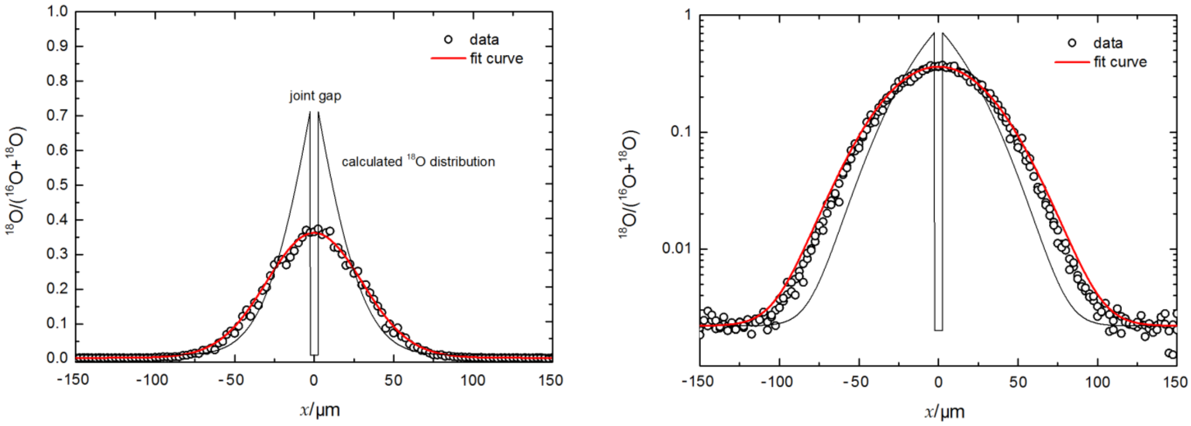

Figure C5. Comparison of measured ^{18}O distributions (SIMS line scan technique, linear scaling on the left hand side, logarithmic scaling on the right hand side) together with calculated actual concentration profiles, taking into account the joint gap. The convolution (red solid line) is simulated utilizing a stepwise iteration algorithm where the resolution function is approximated by a GAUSSIAN distribution with the FWHM being the spot size of the primary ion beam.

C.4 Comparison of different analytical solutions for the diffusion problem

As discussed in section B.1, under most experimental conditions the oxygen incorporation is described by Equation (40), with the flux of oxygen at the gas/solid interface being equal to the diffusional flux of oxygen in the solid. The analytical solution of this diffusion problem in a semi-infinite homogeneous media as given by CRANK [Cran75] was proposed in a more specific notation by FIELITZ and BORCHARDT [Fiel01] and is given in Equation (B2) for constant values of *D* and *K*.

The simultaneous determination of oxygen diffusivity and surface exchange coefficient by measuring the depth distribution of the atomic fraction of ^{18}O isotopes in oxides is based on the analysis of the measured SIMS line scan profiles (as given for example in Figure A5) or depth profiles by fitting with Equation (B2). This approach is, however, limited to half of the sample thickness, as described in section B.2. In the case that the diffusion length of the exchanged or incorporated oxygen tracer reaches the sample half width $\frac{h}{2}$ during the isotope exchange experiment, the natural abundance of ^{18}O in the sample (at $x \to \infty$) $c^{\infty}_{^{18}\mathrm{O}}$ is distorted. Therefore, another approach for simultaneous determination of D_O and K_O data can be applied, based on the work of Fischer and Hertz [Fisc12], an analytical solution of the diffusion problem, which considers especially the measured SIMS line scan profile of a prepared sample as shown in Figure A3. Such a complete line scan profile, where the oxygen diffusion length during the annealing experiment exceeds the sample half width $\frac{h}{2}$ is shown exemplary in Figure C6.

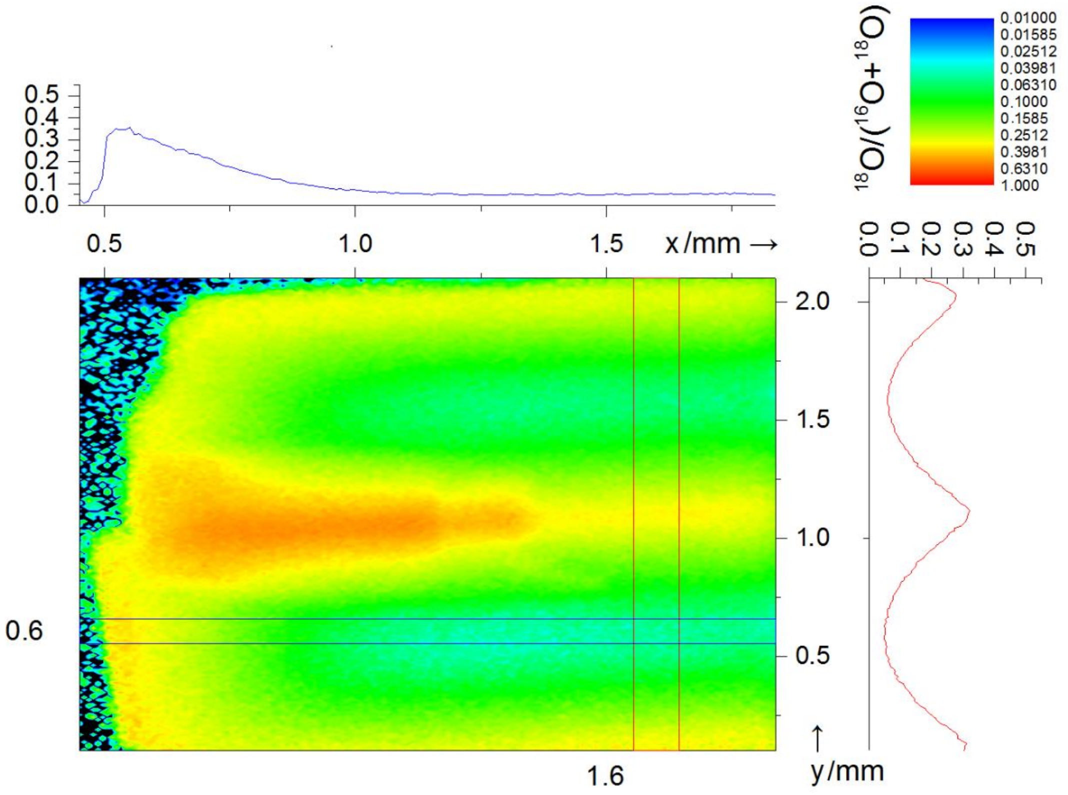

Figure C6. Ion image for ^{18}O tracer exchange of a sectioned sample of nominally un-doped ceria as used in this work. The tracer exchange was conducted in non-equilibrium conditions at T = 800 °C and t = 900 s, with ceria being initially reduced to CeO$_{1.8}$. The blue and red lines indicate the direction of the line scan half and where the secondary ion intensity of ^{18}O (shown at the x - and y - axis) has been averaged. The SIMS measurements were done in imaging mode with a SIMS Workstation (Hiden Analytical Ltd, UK).

In the case of a plane sheet, which is sufficiently thin or where the diffusivity of the considered species is fast, and where the law of exchange of the type given in Equation (B1) during the reduction-oxidation process holds on both surfaces (a case that is equivalent by symmetry), the following solution is given by CRANK [Cran75]:

$$\frac{c_\mathrm{s}(x,t)-c_\infty}{c_\mathrm{g}-c_\infty}=1-\sum_{n=1}^{\infty}\frac{2L^2\exp(-\beta_\mathrm{n}^2 Dt/\left(\frac{h}{2}\right)^2)}{\beta_\mathrm{n}^2(\beta_\mathrm{n}^2+L^2+L)}, \tag{C14}$$

with $L=\frac{h}{2}\frac{K}{D}$ being the characteristic dimensionless parameter of the kinetic regime. The dimensionless β_n values are positive roots of $\beta_\mathrm{n}\tan\beta_\mathrm{n}=L$. The infinite sum in Equation (C14) converges rapidly [Fisc12] after few iteration steps so that Equation (C14) can be approximated by:

$$\frac{c_\mathrm{s}(x,t)-c_\infty}{c_\mathrm{g}-c_\infty}\cong 1-\frac{2L^2\exp(-\beta_1^2 Dt/\left(\frac{h}{2}\right)^2)}{\beta_1^2(\beta_1^2+L^2+L)}. \tag{C15}$$

The line scan profile shown in Figure C6 can therefore be analyzed regarding D_O and K_O over h with Equation (C15) and the determined parameters can be compared to D_O and K_O data determined by fitting the measured isotope distribution over $\frac{h}{2}$ with Equation (B2).

The comparison of the two different approaches of analyzing the measured ^{18}O distribution in the sample is shown in Figure C7, together with the determined parameters D_O and K_O. The difference can be estimated to ≈ 24 % for D_O and ≈ 5 % for K_O, which leads to the conclusion that in a case where the oxygen diffusion length during the annealing experiment extends the sample half width $\frac{h}{2}$ the application of Equation (C15) for the data analysis is more appropriate in terms of the determination of the diffusivity, whereas there is no significant difference concerning the determination of the surface exchange coefficient.

In general it is also possible to apply a finite difference approach to FICK´s second law with the given boundary condition (Equation (B1)) as it was shown for example by LEONHARDT et al. [Leon02], but this approach not considered expedient in context of this work.

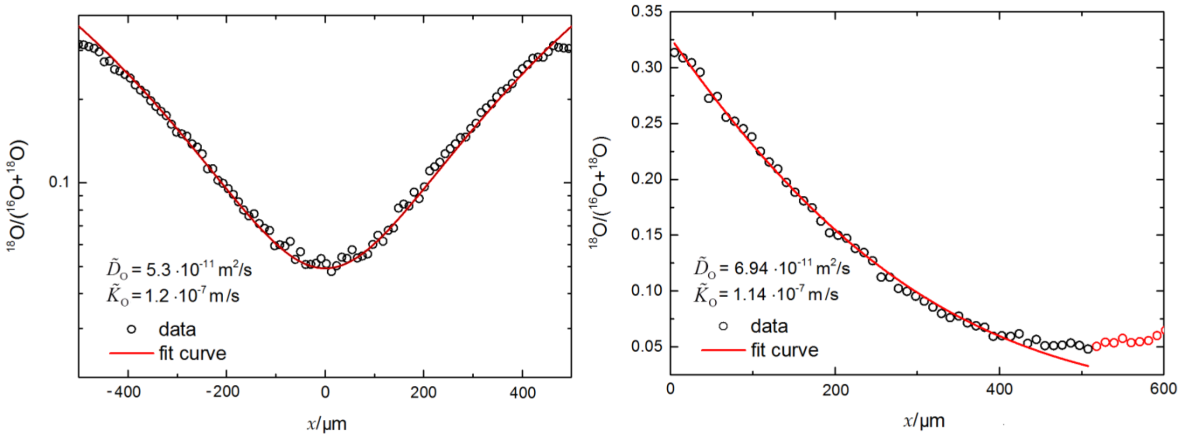

Figure C7. Comparison of two different approaches for the simultaneous determination of D_O and K_O data by applying analytical solutions to the diffusion problem. On the left side a fit of the measured ^{18}O distribution (logarithmic scale) over h by Equation (C15) is shown, which can be compared to the fit of the data over $\frac{h}{2}$ with Equation (B2) on the right side. The difference between the determined parameters is ≈ 24 % for D_O and ≈ 5 % for K_O. The tracer exchange was conducted in non-equilibrium conditions at T = 800 °C and t = 900 s, with ceria being initially reduced to $CeO_{1.8}$.

D Defect chemical models

D.1 Defect structure regarding isolated point defects

During the reduction of cerium oxide oxygen vacancies are formed in order to obtain charge balance of the ionic crystal. Using the KRÖGER-VINK notation [Kroe56], the following reaction Equation shows how the changing Ce^{4+}($[\mathrm{Ce}_{\mathrm{Ce}}^{\times}]$)- and Ce^{3+}($[\mathrm{Ce}'_{\mathrm{Ce}}]$)-concentrations are related to the oxygen vacancy concentration:

$$2\mathrm{Ce}_{\mathrm{Ce}}^{\times} + \mathrm{O}_{\mathrm{O}}^{\times} \leftrightarrow 2\mathrm{Ce}'_{\mathrm{Ce}} + \mathrm{V}_{\mathrm{O}}^{\bullet\bullet} + \frac{1}{2}\mathrm{O}_2(\mathrm{g})\,. \tag{D1}$$

The corresponding law of mass action combines the defect concentrations with a temperature-dependent equilibrium constant $K_{\mathrm{red}} = \exp\left(-\frac{\Delta G_{\mathrm{red}}}{RT}\right)$ and can be written for Equation (D1) as follows:

$$K_{\mathrm{red}} = \frac{a^2_{\mathrm{Ce}'_{\mathrm{Ce}}} \cdot a_{\mathrm{V}_{\mathrm{O}}^{\bullet\bullet}} \cdot a^{\frac{1}{2}}_{\mathrm{O}_2}}{a^2_{\mathrm{Ce}_{\mathrm{Ce}}^{\times}} \cdot a_{\mathrm{O}_{\mathrm{O}}^{\times}}}\,. \tag{D2}$$

For the activities of $\mathrm{Ce}_{\mathrm{Ce}}^{\times}$ and $\mathrm{O}_{\mathrm{O}}^{\times}$ applies under standard conditions $a \approx 1$. Since the concentrations of $\mathrm{Ce}_{\mathrm{Ce}}'$ and $\mathrm{V}_{\mathrm{O}}^{\bullet\bullet}$ are very small, in the first approximation for the activities the concentrations can be used. Applying $a = \frac{p_\mathrm{i}}{p_\mathrm{i}^0}$ the following relation for K_red can be deduced:

$$K_\mathrm{red} = [\mathrm{Ce}_{\mathrm{Ce}}']^2 \cdot [\mathrm{V}_{\mathrm{O}}^{\bullet\bullet}] \cdot p_{\mathrm{O}_2}^{\frac{1}{2}} . \tag{D3}$$

Considering the charge neutrality condition Equation (D4),

$$0.5[\mathrm{Ce}_{\mathrm{Ce}}'] = [\mathrm{V}_{\mathrm{O}}^{\bullet\bullet}] , \tag{D4}$$

the Equation (D3) can be simplified and yields Equation (D5):

$$K_\mathrm{red} = 4[\mathrm{V}_{\mathrm{O}}^{\bullet\bullet}]^3 \cdot p_{\mathrm{O}_2}^{\frac{1}{2}} . \tag{D5}$$

There is thus proportionality between oxygen vacancy concentration and the oxygen partial pressure:

$$[\mathrm{V}_{\mathrm{O}}^{\bullet\bullet}] = \frac{K_\mathrm{red}^{\frac{1}{3}}}{4} \cdot p_{\mathrm{O}_2}^{-\frac{1}{6}} . \tag{D6}$$

Since $\left[\mathrm{V}_{\mathrm{O}}^{\bullet\bullet}\right] = 0.5\delta$, the non-stoichiometry δ is proportional to $p_{\mathrm{O}_2}^{-\frac{1}{6}}$:

$$\delta \propto p_{\mathrm{O}_2}^{-\frac{1}{6}} . \tag{D7}$$

D.2 Defect structure regarding defect clusters

With increasing oxygen non-stoichiometry, isolated defects can interact to form defect complexes that are themselves new defects. The trimer consists of an oxygen vacancy and two reduced cerium cations. The formation Equation and the corresponding mass action Equation are given by:

$$2\mathrm{Ce}_{\mathrm{Ce}}^{\times} + \mathrm{O}_{\mathrm{O}}^{\times} \leftrightarrow \left(\mathrm{Ce}_{\mathrm{Ce}}'\mathrm{V}_{\mathrm{O}}^{\bullet\bullet}\mathrm{Ce}_{\mathrm{Ce}}'\right)^{\times} + \frac{1}{2}\mathrm{O}_2(\mathrm{g}) , \tag{D8}$$

$$K_\mathrm{red} = \frac{a_{\left(2\mathrm{Ce}_{\mathrm{Ce}}'\mathrm{V}_{\mathrm{O}}^{\bullet\bullet}\right)^{\times}} \cdot a_{\mathrm{O}_2}^{\frac{1}{2}}}{a_{\mathrm{Ce}_{\mathrm{Ce}}^{\times}}^2 \cdot a_{\mathrm{O}_{\mathrm{O}}^{\times}}} . \tag{D9}$$

Applying $a = \frac{p_\mathrm{i}}{p_\mathrm{i}^0}$ the following relation for K_red can be deduced:

$$K_\mathrm{red} = \left[\left(2\mathrm{Ce}'_\mathrm{Ce} \mathrm{V}_\mathrm{O}^{\bullet\bullet} \right)^{\times} \right] \cdot p_{\mathrm{O}_2}^{\frac{1}{2}} \cdot \tag{D10}$$

There is thus proportionality between the trimer concentration and the oxygen partial pressure:

$$\left[\left(2\mathrm{Ce}'_\mathrm{Ce} \mathrm{V}_\mathrm{O}^{\bullet\bullet} \right)^{\times} \right] = K_\mathrm{red} \cdot p_{\mathrm{O}_2}^{-\frac{1}{2}} \cdot \tag{D11}$$

E Phenomenological modelling of reaction parameters

E.1 Coupling of the macroscopic diffusion coefficients

In the context of this work the determined macroscopic parameters are the tracer diffusion coefficient $D^*_{\mathrm{O}^{2-}}$, reflecting the "true" self-diffusion coefficient of the oxygen ions in the absence of a driving force, and the chemical diffusion coefficient $\tilde{D}_\mathrm{O}$ of oxygen, which formally characterizes for ionic compounds a charge-neutral ambipolar diffusion.

Here the diffusion of oxygen takes places as a result of coupled transport of O^{2-} and $2e^-$ in opposite directions. As a consequence, $\tilde{D}_\mathrm{O}$ is going to be of the order of magnitude of the defect diffusion coefficients and represents a combination of ionic and electronic defect diffusivities.

In random-walk theory, as discussed in section 4.2, it is assumed that the atom jump probabilities do not depend on the directions of previous jumps. However, in real crystals this is not the case, successive atom jumps are correlated to one another; therefore each atom follows a correlated walk. The random walk diffusion Equations are therefore modified by introducing a correlation factor. The effective frequency of random jumps v^e then differs from the actual jump frequency v^a in Equation (30) [Mann68]:

$$v^e = f v^a, \tag{E1}$$

where f is the correlation factor, which equals the fraction of jumps which are effective in causing random diffusion, and which can be also expressed in terms of the coupling between the fluxes of $D^*_{\mathrm{O}^{2-}}$ and $D_{\mathrm{O}^{2-}}$ as the origin of the correlation effects [Mehr07].

For self-diffusion by a vacancy mechanism, the correlation factor ranges between 0.78 for f.c.c. structure and 0.5 for a diamond structure [Gron61, Hunt61]. The experimentally derived tracer diffusion coefficient of oxygen is related to the self-diffusion coefficient of the oxygen ions by the correlation factor in the following way [Mann68, Mehr07]:

$$D^{*}_{\mathrm{O}^{2-}} = fD_{\mathrm{O}^{2-}} \,. \tag{E2}$$

For simplification the correlation factor is assumed as $f \approx 1$ as a first approximation in the context of this work. Based on the existence of a chemical potential gradient characterizing a composition change in an oxide sample, the experimentally derived chemical diffusion coefficient of oxygen is then coupled via the thermodynamic factor w_{O} with the tracer diffusion coefficient as follows:

$$\tilde{D}_{\mathrm{O}} = w_{\mathrm{O}}(x=0) D^{*}_{\mathrm{O}^{2-}} \,, \tag{E3}$$

where $w_{\mathrm{O}}(x=0)$ is related to μ_{O} according to Maier [Maie98, Maie00]:

$$w_{\mathrm{O}}(x=0) = \frac{c_{\mathrm{O}}(x=0)}{RT} \left.\frac{\partial \mu_{\mathrm{O}}}{\partial c_{\mathrm{O}}}\right|_{x=0} . \tag{E4}$$

E.2 Derivation of the different effective equilibrium exchange rates of oxygen

The surface reaction of oxygen incorporation, in particular, is made up of several complex individual steps [Maie04, DeSo06]. The reaction pathway involves the adsorption and dissociation of oxygen molecules on the surface, the reaction with an oxygen vacancy and the transfer of oxygen ions through the surface, in addition to several charge transfer steps (Equations (34) - (38)). As a consequence of this proposed pathway the most likely rate determining step (rds) is charge transfer leading to dissociation. According to BODENSTEIN´s principle one step in the pathway is assumed to be rate determining and all preceding and succeeding reaction steps are treated as being at quasi-equilibrium.

The so-called apparent or effective equilibrium exchange rate of oxygen $\Re^{0}_{\mathrm{O}}$ (being a measure of the dynamics at equilibrium, which is likewise an exchange current density) of the rate determining step is then defined by [DeSo06, Fiel16]:

$$\Re_{\mathrm{O}}^{0} = \left(\overleftarrow{k}_{\mathrm{rds}}\left[\mathrm{O}'_{\mathrm{ad}}\right] \times \overrightarrow{k}_{\mathrm{rds}}\left[\mathrm{O}_{\mathrm{ad}}\right]\left[\mathrm{e}'\right]\right)^{\frac{1}{2}}, \tag{E5}$$

where $\overrightarrow{k}_{\mathrm{rds}}$ and $\overleftarrow{k}_{\mathrm{rds}}$ are the forward and backward reaction rates of the rate determining step (= charge transfer step). After inserting the mass action constants for the preceding and succeeding reaction steps (adsorption and incorporation):

$$K_{\mathrm{ad}} = \frac{\left[\mathrm{O}_{\mathrm{ad}}\right]}{p_{\mathrm{O}_2}^{\frac{1}{2}}}, \tag{E6}$$

$$K_{\mathrm{inc}} = \frac{\left[\mathrm{O}_{\mathrm{O}}^{\times}\right]\left[\mathrm{h}^{\bullet}\right]}{\left[\mathrm{O}'_{\mathrm{ad}}\right]\left[\mathrm{V}_{\mathrm{O}}^{\bullet\bullet}\right]}, \tag{E7}$$

into Equation (E5) one can finally deduce:

$$\Re_{\mathrm{O}}^{0} = \left(\frac{\overleftarrow{k}_{\mathrm{rds}}\overrightarrow{k}_{\mathrm{rds}}K_{\mathrm{ad}}}{K_{\mathrm{inc}}}\right)^{\frac{1}{2}} \left(\left[\mathrm{O}_{\mathrm{O}}^{\times}\right]\left[\mathrm{e}'\right]\left[\mathrm{h}^{\bullet}\right]\right)^{\frac{1}{2}} \frac{p_{\mathrm{O}_2}^{\frac{1}{4}}}{\left[\mathrm{V}_{\mathrm{O}}^{\bullet\bullet}\right]^{\frac{1}{2}}}. \tag{E8}$$

As $\mathrm{CO_2}$ splitting on reduced $\mathrm{CeO}_{2-\delta}$ surfaces involves the exchange and incorporation of oxygen it is obvious to consider the oxygen incorporation as fundamental reaction. In accordance with the discussed established ideas on surface exchange from pure oxygen atmospheres the reaction scheme given in Equations (45) - (48) can be deduced.

It is most probable that steps (47) and (48) occur simultaneously in one step since O^{2-}(ad) is not stable at the surface [DeSo06]. As a consequence of this proposed pathway the most likely rate determining step (rds) again is charge transfer leading to dissociation. In the case of carbon dioxide reduction the effective equilibrium exchange rate of oxygen $\Re_{\mathrm{O}}^{0}$ of the rate determining step is then defined by:

$$\Re_{\mathrm{O}}^{0} = \left(\overleftarrow{k}_{\mathrm{rds}}\left[\mathrm{CO}'_{2,\mathrm{ad}}\right] \times \overrightarrow{k}_{\mathrm{rds}}\left[\mathrm{CO}_{2,\mathrm{ad}}\right]\left[\mathrm{e}'\right]\right)^{\frac{1}{2}}, \tag{E9}$$

where $\overrightarrow{k}_{\mathrm{rds}}$ and $\overleftarrow{k}_{\mathrm{rds}}$ are again the forward and backward reaction rates of the rate determining step (= charge transfer step).

After inserting the mass action constants for the preceding and succeeding reaction steps (adsorption and incorporation):

$$K_{\mathrm{ad}} = \frac{\left[\mathrm{CO}_{2,\mathrm{ad}}\right]}{\left[\mathrm{CO}_2\right]}\,, \tag{E10}$$

$$K_{\mathrm{inc}} = \frac{\left[\mathrm{CO}\right]\left[\mathrm{O}_{\mathrm{O}}^{\times}\right]}{\left[\mathrm{CO}'_{2,\mathrm{ad}}\right]\left[\mathrm{V}_{\mathrm{O}}^{\bullet\bullet}\right]\left[\mathrm{e}'\right]}\,, \tag{E11}$$

as well as the mass action constant for the carbon dioxide dissociation in the gas phase,

$$K_{\mathrm{diss}} = \frac{\left[\mathrm{CO}\right] p_{\mathrm{O}_2}{}^{\frac{1}{2}}}{\left[\mathrm{CO}_2\right]}\,, \tag{E12}$$

into Equation (E9) one can finally deduce:

$$\Re_{\mathrm{O}}^{0} = \left(\frac{\overleftarrow{k}_{\mathrm{rds}}\overrightarrow{k}_{\mathrm{rds}}K_{\mathrm{ad}}K_{\mathrm{diss}}}{K_{\mathrm{inc}}}\right)^{\frac{1}{2}} \frac{\left[\mathrm{CO}_2\right]\left(\left[\mathrm{O}_{\mathrm{O}}^{\times}\right]\right)^{\frac{1}{2}}}{\left[\mathrm{V}_{\mathrm{O}}^{\bullet\bullet}\right]^{\frac{1}{2}} p_{\mathrm{O}_2}{}^{\frac{1}{4}}}\,. \tag{E13}$$

E.3 Correlation between surface exchange coefficient, diffusion coefficient and equilibrium exchange rate of oxygen

The correlation between K_{O} and D_{O} principally results from the boundary condition at the gas/solid interface by coupling Equations (20) and (40):

$$j_{\mathrm{O}}(x=0) = K_{\mathrm{O}}\Delta c_{\mathrm{O}}(x=0) = D_{\mathrm{O}} \left.\frac{\partial c_{\mathrm{O}}}{\partial x}\right|_{x=0}\,, \tag{E14}$$

which has to be respected when solving the respective diffusion Equation [Cran75]. The so-called characteristic length L (being the characteristic dimensionless parameter of the kinetic regimes) results directly from the boundary condition and is defined as [Fiel16]:

$$L = \frac{1}{w_{\mathrm{O}}(x=0)}\frac{D_{\mathrm{O}}}{K_{\mathrm{O}}}\,. \tag{E15}$$

The physical meaning of L becomes evident if the characteristic time constant τ is defined:

$$\tau = \frac{L}{w_{\mathrm{O}}(x=0)K_{\mathrm{O}}} = \frac{D_{\mathrm{O}}}{K_{\mathrm{O}}^{2}}\,. \tag{E16}$$

The characteristic length L is thus proportional to the diffusion length the oxygen ions cover in the near-surface region during the characteristic time τ. The term $K_O/\Delta x$ in Equation (41) can be considered equivalent to τ^{-1}. Therefore FIELITZ and BORCHARDT postulated [Fiel16]:

$$\tau = \frac{c_O(x=0)}{w_O(x=0)\Re_O^0} \,. \tag{E17}$$

Combining Equation (E16) with Equation (E17) yields the correlation between K_O and D_O:

$$K_O^{h\to\infty} = \left(w_O(x=0) D_O \frac{\Re_O^0}{c_O(x=0)} \right)^{\frac{1}{2}} , \tag{E18}$$

which is identical with Equation (44) for the boundary condition given in (E9) for plate-like samples of large thickness with $h > L$.

The condition $h \approx L$ means that within the characteristic time τ in principle all the oxygen is exchanged in the sample, which is usually referred to as the mixed regime. Here the oxygen exchange rate $\Re_O^0$ at the surface and the diffusion coefficient of oxygen D_O hinder the overall exchange simultaneously. This is often the case during non-equilibrium chemical exchange experiments with $w_O(x=0) > 1$ when the oxygen diffusion is strongly enhanced due to Equation (E3).

The condition $h < L$ means that the oxygen exchange at the sample surface is slow and/or the oxygen bulk diffusion is rapid, which then means that the oxygen exchange of the sample is dominated by the oxygen exchange rate $\Re_O^0$ at the surface. This corresponds to the surface exchange regime. For a sufficiently thin plate-like sample the solution of the diffusion Equation given in Equation (B2) can then be approximated by:

$$\frac{c_{^{18}O}(x,t) - c_{^{18}O}^{\infty}}{c_{^{18}O}^{g} - c_{^{18}O}^{\infty}} = 1 - \exp\left(-\frac{t}{\tau} \right) with \quad \tau = \frac{h}{2} \frac{1}{K_O} \,. \tag{E19}$$

For the boundary conditions as given in Equation (43) this yields for K_O:

$$K_O^{h\to 0} = \frac{h}{2} w_O(x=0) \frac{\Re_O^0}{c_O(x=0)} \,. \tag{E20}$$

E.4 Coupling of the macroscopic surface exchange coefficients

Depending on the experimental conditions three respective macroscopic surface exchange coefficients $K^{Q}_{\mathrm{O}^{2-}}$, $K^{*}_{\mathrm{O}^{2-}}$, $\tilde{K}_{\mathrm{O}}$ can be differentiated in analogy to the different macroscopic diffusion coefficients according to MAIER [Maie04], where only the latter two are relevant in the context of this thesis. Equation (40) in section 4.3 is only valid for surface reactions at $x = 0$, meaning that the surface exchange coefficient K_{O} depends on the defect chemistry of the surface only. For an oxygen isotope exchange experiment with $D^{*}_{\mathrm{O}^{2-}} = fD_{\mathrm{O}^{2-}}$ and $w_{\mathrm{O}} = 1$ Equation (E18) becomes [Fiel16]:

$$\left(K^{*}_{\mathrm{O}}\right)^2 = D^{*}_{\mathrm{O}} \frac{\Re^{0}_{\mathrm{O}}}{c_{\mathrm{O}}(x=0)}. \tag{E21}$$

In a chemical exchange experiment with $w_{\mathrm{O}} > 1$ and $\tilde{D}_{\mathrm{O}} = w_{\mathrm{O}}(x=0)D^{*}_{\mathrm{O}^{2-}}$ Equation (E18) yields:

$$\left(\tilde{K}_{\mathrm{O}}\right)^2 = \tilde{D}_{\mathrm{O}} \frac{\Re^{0}_{\mathrm{O}}}{c_{\mathrm{O}}(x=0)} = w_{\mathrm{O}}(x=0)D^{*}_{\mathrm{O}} \frac{\Re^{0}_{\mathrm{O}}}{c_{\mathrm{O}}(x=0)} = w_{\mathrm{O}}(x=0)\left(K^{*}_{\mathrm{O}}\right)^2. \tag{E22}$$

Then follows, in contrast to the relation in Equation (E3) concerning D_{O}:

$$\tilde{K}_{\mathrm{O}} = \sqrt{w_{\mathrm{O}}(x=0)}K^{*}_{\mathrm{O}}. \tag{E23}$$

E.5 Relation between thermodynamic factor and oxygen non-stoichiometry

Conferring Equation (11) the general relation of the oxygen non-stoichiometry and oxygen activity as discussed in section 4.1 can be given as:

$$\frac{\partial \ln \delta}{\partial \ln a_{\mathrm{O}_2}} = \pm n. \tag{E24}$$

In addition to the definition of the thermodynamic factor as given in Equation (E4) the more general definition reads:

$$w_{\mathrm{O}} = \frac{c_{\mathrm{O}}}{RT}\frac{\partial \mu_{\mathrm{O}}}{\partial c_{\mathrm{O}}} = \frac{\partial \ln a_{\mathrm{O}}}{\partial \ln c_{\mathrm{O}}}. \tag{E25}$$

Considering the elementary reaction $O_2 \leftrightarrow 2O$ with $K_{\mathrm{diss}} = \frac{{a_{\mathrm{O}}}^2}{a_{\mathrm{O_2}}}$, the general relation between a_{O} and δ is:

$$\partial \ln a_{\mathrm{O}} = \frac{1}{2} \partial \ln a_{\mathrm{O_2}} = \frac{1}{\pm n} \frac{1}{2} \partial \ln \delta \,. \tag{E26}$$

Since $c_{\mathrm{O}} = c_{\mathrm{O}}^0 \left(1 - \delta\right)$, the general relation between c_{O} and δ is:

$$\partial \ln c_{\mathrm{O}} = \partial \ln\left(c_{\mathrm{O}}^0 \left(1 \pm \delta\right)\right) = \partial \ln\left(1 \pm \delta\right) = \frac{\partial\left(1 \pm \delta\right)}{\left(1 \pm \delta\right)} \,. \tag{E27}$$

The relation between the thermodynamic factor and the oxygen non-stoichiometry can thus be written as:

$$w_{\mathrm{O}} = \frac{\frac{1}{\pm n} \frac{1}{2} \partial \ln \delta}{\frac{\partial\left(1 \pm \delta\right)}{\left(1 \pm \delta\right)}} = \frac{1}{\pm n} \frac{1}{2} \left(\pm 1\right) \frac{1 \pm \delta}{\delta} \,, \tag{E28}$$

$$w_{\mathrm{O}}(-n, -\delta) = \frac{1}{2n} \frac{1 - \delta}{\delta} \,, \tag{E29}$$

$$w_{\mathrm{O}}(+n, +\delta) = \frac{1}{2n} \frac{1 + \delta}{\delta} \,. \tag{E30}$$

In a more generalized form the following simplification is valid if $\left|\delta\right| << 1$:

$$w_{\mathrm{O}}(n, \delta) = \frac{1}{2n} \frac{1}{\delta} \,. \tag{E31}$$

F Error estimation

For error consideration, a distinction is made between systematic and random (statistical) errors. The goal is to estimate the largest error Δx of a measurement variable x by linear addition of the undetected systematic error with the random, statistical error. Systematic errors are basically detectable and consistent for each repetition of the measurement. They occur either as detected systematic errors or as unrecorded systematic errors. Systematic deviations elude statistical treatment. In particular, it cannot be assumed that it is unlikely that all deviations of the measured variables are at the same time extreme.

The systematic errors include the manufacturer's deviations or measurement uncertainties of the measuring instruments (i.e. resolution of the measuring devices), which occur as maximum deviations of the measurements from each other when the measurement is repeated under identical conditions. This is called the concept of reproducibility, i.e. the statistical part of the systematic error, and is separated from the statistical contribution of the measuring.

Random errors are subjective errors by the observer or objective errors due to external influences. They are subject to statistical laws and fluctuate randomly. Random errors can be estimated by multiple measurements. Fluctuations in the measured values themselves are basically no measurement errors or measurement deviations, and therefore decoupled from the error consideration.

The reproducibility of SIMS measurements itself is very good. Nevertheless, in the context of this work, several further distinctions regarding considered errors were made. First, the primary systematic measurement errors regarding secondary ion mass spectrometry are the influence of the primary ion species on the ^{18}O distribution in the case that the primary ions are oxygen ions, as discussed in section C.2, and the distortion of the ^{18}O distribution in the case of SIMS line scan measurements as discussed in section C.3. These systematic errors are consistent and could be quantified as well as corrected in the context of this work. Second, several statistical measurement errors of physical quantities had to be taken into account. As discussed in section C.1, the influence of temperature measurement and annealing time on the diffusion anneals had to be respected, where, after the correction of secondary systematic errors, the remaining uncertainty of the temperature measurement was approximately ± 10 K.

In the case of SIMS depth profiling, depth calibration was done by measuring the SIMS crater depth using a surface profiler, which leaves an uncertainty of x due to SIMS crater roughening and inhomogeneity of about 10 %. A similar influence is introduced by the fluctuation of the primary ion current, which cannot be measured simultaneously, but, however, before and after SIMS depth profiling. It can be approximated to about 10 %. Regarding the simultaneous determination of D_O and K_O data by SIMS methods (utilizing Equation (B2)) the general limitations discussed in chapter B of the appendix had to be considered, but besides that, measurement limitations of random characteristics by SIMS due to sample surface roughness or a deposited conductive layer with respect to the ^{18}O surface concentration occur additionally. These features influence primarily the determination of K_O by fitting with Equation (B2) and can be approximated to about 15 %. Third, statistical uncertainties of the fitting procedure of the measured oxygen distributions itself occur, although they are not greater than 2 %. Since these sources of error are not statistically independent of one another, the individual errors can be added, yielding maximum statistical errors of about 22 % for D_O and of about 37 % for K_O data.

If a physical quantity is not measured directly, but rather is calculated as a function of several other measured physical quantities x, y, z, i.e. $f = f(x, y, z)$, the deviations of the measured physical quantities can be linked by forming partial derivatives. If the measured variables x, y, z are statistically independent of one another, a GAUSSIAN propagation of error can be used:

$$\Delta f = \sqrt{\left(\frac{\partial f}{\partial x}\right)^2 \cdot \Delta x^2 + \left(\frac{\partial f}{\partial y}\right)^2 \cdot \Delta y^2 + \left(\frac{\partial f}{\partial z}\right)^2 \cdot \Delta z^2}\ . \tag{F1}$$

In the case of determined activation enthalpies, for example the overall activation enthalpy of diffusion ΔH_a in Equation (24), the resultant propagation of error is then derived with:

$$\Delta H_\mathrm{a} = -k_\mathrm{B} T \ln \frac{D_\mathrm{i}}{D_\mathrm{i}^0}\ . \tag{F2}$$

With the temperature measurement error being very small and thus neglected, the partial derivation is given by:

$$\Delta\Delta H_\mathrm{a} = \sqrt{\left(-\frac{k_\mathrm{B} T}{D_\mathrm{i}}\right)^2 \cdot \Delta D_\mathrm{i}^2 + \left(\frac{k_\mathrm{B} T}{D_\mathrm{i}^0}\right)^2 \cdot \Delta D_\mathrm{i}^{0^2}}\ . \tag{F3}$$

A similar derivation is valid in case of the activation enthalpy of surface exchange. For calculating the equilibrium exchange rate Equation (44) is used:

$$\Re_\mathrm{O}^0 \frac{w(x=0)}{c_\mathrm{O}(x=0)} = \frac{\left(K_\mathrm{O}^{h\to\infty}\right)^2}{D_\mathrm{O}}\ , \tag{F4}$$

with the partial derivation given by:

$$\Delta\Re_\mathrm{O}^0 \frac{w(x=0)}{c_\mathrm{O}(x=0)} = \sqrt{\frac{4K_\mathrm{O}^2}{D_\mathrm{O}^2} \cdot \Delta K_\mathrm{O}^2 + \frac{K_\mathrm{O}^4}{D_\mathrm{O}^4} \cdot \Delta D_\mathrm{O}^2}\ . \tag{F5}$$